SuperDARN Cross Polar Cap Potential and Parameters of the Near-Earth Space

A Thesis Submitted to the
College of Graduate Studies and Research
in Partial Fulfillment of the Requirements
for the degree of Master of Science
in the Department of Physics and Engineering Physics
University of Saskatchewan
Saskatoon

By
Daniel Mori

PERMISSION TO USE

In presenting this thesis in partial fulfilment of the requirements for a Postgraduate degree from the University of Saskatchewan, I agree that the Libraries of this University may make it freely available for inspection. I further agree that permission for copying of this thesis in any manner, in whole or in part, for scholarly purposes may be granted by the professor or professors who supervised my thesis work or, in their absence, by the Head of the Department or the Dean of the College in which my thesis work was done. It is understood that any copying or publication or use of this thesis or parts thereof for financial gain shall not be allowed without my written permission. It is also understood that due recognition shall be given to me and to the University of Saskatchewan in any scholarly use which may be made of any material in my thesis.

Requests for permission to copy or to make other use of material in this thesis in whole or part should be addressed to:

Head of the Department of Physics and Engineering Physics
University of Saskatchewan
116 Science Place
Saskatoon, Saskatchewan S7N 5A9

ABSTRACT

The Super Dual Auroral Radar Network (SuperDARN) of HF coherent radars routinely report the so-called cross polar cap potential (CPCP), a voltage applied by the solar wind and interplanetary magnetic field (IMF) onto the high-latitude ionosphere. The CPCP ultimately drives the global-scale plasma circulation and thus reflects the influence of the Sun on the near-Earth electrodynamic environment. In this Thesis, SuperDARN measurements of the CPCP collected over the year 2000 are investigated with a goal to statistically assess its relationship with various parameters of the solar wind and IMF and to compare found tendencies with expectations of several key theories/models predicting the CPCP. It is shown that SuperDARN measurements show smaller CPCPs when compared with theories/empirical models and show a smaller dependence on various parameters. Some reported tendencies, such as IMF B_z dependence, were found to be consistent with measurements by other instruments, as reported in the literature. In an attempt to clarify the reasons for discrepancies, SuperDARN CPCPs were compared with velocity measurements, acting as a proxy for the ionospheric electric field, from the Resolute Bay ionosonde, which was in operation within the central polar cap and was monitoring the flows contributing significantly to the CPCP. The expected linear relationship between SuperDARN CPCP and ionosonde velocities was confirmed. As a side issue, the Resolute Bay ionosonde velocities were compared with the velocities measured by the SuperDARN radars at Rankin Inlet and Inuvik over the area monitored by the ionosonde. Reasonable agreement was found between the instruments, which implies that ionosondes and SuperDARN are compatible.

ACKNOWLEDGEMENTS

First, I would like to thank my supervisor Dr. Sasha Koustov. His help and guidance made this Thesis possible. I would also like to thank the professors, researchers and grad students in ISAS for support and feedback on this project; and all my fellow denizens of the physics student lounge.

I would also like to thank Chad Bryant for the availability of the SuperDARN CPCP data used in this Thesis; P. T. Jayachandran for the availability of CHAIN CADI data; and NASA's Goddard Space Flight Center for the availability of OMNI IMF and SW data.

Financial support, for which I am grateful, was received from the College of Graduate Studies and Research, the Physics and Engineering Physics department and the Institute of Space and Atmospheric Studies at the University of Saskatchewan, and the Canadian Space Agency.

Finally, I would like to thank my parents and, most of all, my fiancée Kristan for her constant support and patience with me during our time in Saskatoon.

CONTENTS

LIST OF TABLES

LIST OF FIGURES

LIST OF ABBREVIATIONS

SW	Solar Wind
IMF	Interplanetary Magnetic Field
IEF	Interplanetary Electric Field
GSM	Geocentric Solar Magnetic
FAC	Field-aligned current
R1	Region 1
R2	Region 2
CPCP	Cross polar cap potential
MHD	Magnetohydrodynamics
MLAT	Magnetic Latitude
FoV	Field-of-View
SuperDARN	Super Dual Auroral Radar Network
PolarDARN	Polar Dual Auroral Radar Network
CHAIN	Canadian High Arctic Ionospheric Network
CADI	Canadian Advanced Digital Ionosonde
PCN	Polar Cap North (Index)
DMSP	Defense Meteorological Satellites Program
AMIE	Assimilative Mapping of Ionospheric Electrodynamics
HF	High frequency
l-o-s	line-of-sight
ACF	Autocorrelation function
HMB	Heppner-Maynard boundary
RB	Resolute Bay
EU	Eureka
RKN	Rankin
INV	Inuvik
SAS	Saskatoon
KOD	Kodiak
AOA	Angle of Arrival
AACGM	Altitude-Adjusted Corrected Geomagnetic

CHAPTER 1

INTRODUCTION

The Sun is the source of energy for everything on the Earth. Besides light in the visible spectrum of electromagnetic waves, the energy is continuously delivered through more static fields and charged particles that are accumulated in the near-Earth environment. One well-established effect is the onset of a quasi-static global-scale electric field that forces the charged particles in the upper atmosphere to directional motion that is often referred to as convection. The particle motion due to electric and magnetic fields affects the temperature regime of the atmosphere at certain heights. Thus, the strength of the convection ultimately determines how much energy is delivered to the near-Earth environment in the form of particles and fields. The major goal of the intended research is to evaluate the efficiency of energy delivery to the upper atmosphere through the global scale electric fields. The following section contains a description of the basic concepts and major regions of the near-Earth space based on the works of *Hargreaves* (1992) and *Kivelson and Russell* (1995).

1.1 The Solar Wind and the Magnetosphere

The Sun continuously emits a highly-conducting plasma called the solar wind. It is composed mainly of protons and electrons, in roughly equal parts, and a small percentage of alpha particles, making up $\sim$5% of the total number of particles. The average solar wind density n_{sw} near the Earth is $\sim$5 cm^{-3}. The solar wind plasma expands outward from the Sun radially at velocities typically around 400 km/s and can exceed 1000 km/s under strong solar conditions. The solar wind plasma drags solar magnetic field lines along with it, forming the interplanetary magnetic field (IMF), with typical component values

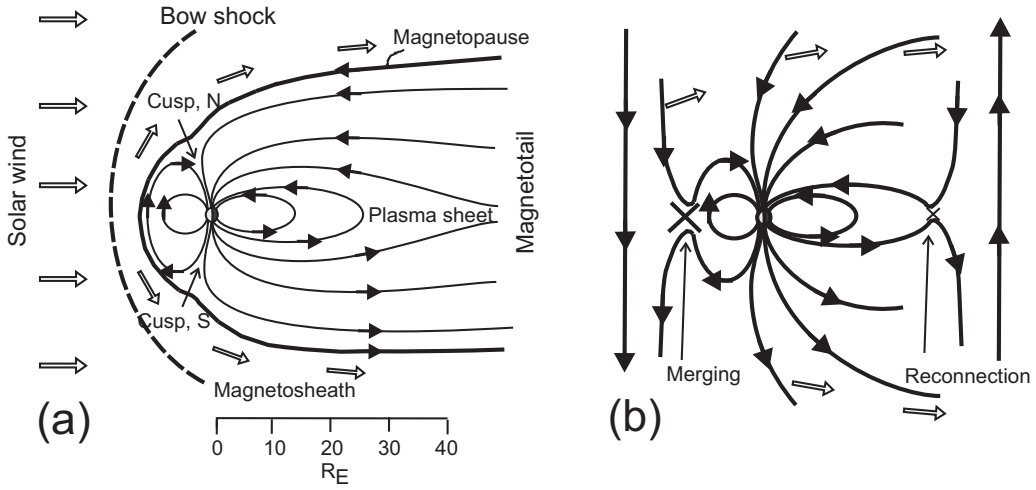

Figure 1.1: (a) A cross-section of the magnetosphere, in the plane containing the geomagnetic dipole. (b) The magnetic merging/reconnection process for a southward IMF.

from -10 to 10 nT. Due to the highly-conducting nature of the solar wind, the IMF flux is "frozen" into the plasma.

As the solar wind approaches the near-Earth environment, it interacts with the Earth's dipole-like magnetic field (Fig. 1.1a). The solar wind is diverted around the geomagnetic field, creating a cavity, the magnetosphere, which is compressed by the solar wind on the dayside and elongated on the nightside, forming the magnetotail. The boundary between the magnetosphere and the solar wind, the magnetopause, is formed by the balancing of the solar wind pressure p_{sw} and the geomagnetic field pressure. On the dayside, this implies that the magnetosphere extends out to (*Spreiter et al.*, 1966)

$$R_{ms} = \left(\frac{(2B_0 R_E^3)^2}{2\mu_0 p_{sw}} \right)^{1/6} \simeq 10.7 p_{sw}^{-1/6} R_E, \tag{1.1}$$

where B_0 = 31 μT is the strength of Earth's magnetic field at the surface of the Earth near the magnetic equator, R_E = 6371 km is the Earth's radius, and $\mu_0 = 4\pi \times 10^{-7} N \cdot A^{-2}$ is the permeability of free space. The point on the dayside magnetopause farthest from the Earth is known as the stagnation point; the distance to the stagnation point is the magnetosphere radius. Near $\pm 78^\circ$ magnetic latitude, there are neutral points called the polar cusps, where the magnetic field at the magnetopause is near zero.

About 2-3 R_E in front of the magnetopause, the solar wind undergoes a sudden deceleration, changing from supersonic to subsonic speeds. This occurs in a region called the

bow shock, which is analogous to the shock wave that forms around a jet or bullet travelling at supersonic speeds. The area between the bow shock and the magnetopause, the magnetosheath, is filled with a slower-moving but hotter plasma. Both the plasma density and IMF field strength increase by a factor r (*Ridley*, 2005),

$$r = \frac{2(\gamma+1)}{C+\sqrt{C^2+4(\gamma+1)(2-\gamma)M_A^{-2}}}, \tag{1.2}$$

$$C = \gamma-1+2M_s^{-2}+\gamma M_A^{-2}, \tag{1.3}$$

where

$$M_A = \frac{v_{sw}}{v_A}, \tag{1.4}$$

$$M_s = \frac{v_{sw}}{c_s}, \tag{1.5}$$

$$v_A = \frac{B}{\sqrt{\mu_0\rho}}, \tag{1.6}$$

$$c_s = \sqrt{\frac{\gamma k_B T_p}{m_p}}, \tag{1.7}$$

are the Alfvén-Mach number, sonic Mach number, Alfvén velocity and thermal speed, respectively; m_p is the mass of a proton; T_p is the solar wind proton temperature; k_B is the Boltzmann constant; B is the IMF strength; ρ is the solar wind mass density and γ is 5/3. In the limit of large Mach and Alfvén-Mach numbers, r approaches the upper limit of 4. Boundary conditions require that the total solar wind pressure (dynamic, magnetic and thermal), the solar wind electric field and the mass flux are constant across the bow shock. The magnetosheath plasma either is diverted around the magnetopause, with ions moving duskward and electrons moving dawnward, setting up a closed current system called the Chapman-Ferraro currents, or travels along geomagnetic field lines into the ionosphere forming field-aligned currents (FACs) known as Region 1 (R1) currents. The process believed to be primarily responsible for generating the R1 currents is magnetic reconnection.

Reconnection is a process that occurs in plasma where magnetic field lines from different domains can couple and form two topologically different field lines. This occurs at the frontside magnetopause when the IMF is antiparallel to the geomagnetic field. "Merging" is the term often used for the dayside process. For a southward IMF, where $B_z < 0$

in the GSM[1] coordinate system, merging occurs near the stagnation point (Fig. 1b), while for a northward IMF ($B_z > 0$) it occurs at high latitudes anti-sunward of the polar cusps. Merging results in geomagnetic field lines becoming "open" to the solar wind, allowing particles to flow into the magnetosphere and the solar wind electric field,

$$\mathbf{E}_{sw} = -\mathbf{v} \times \mathbf{B}, \tag{1.8}$$

to map into the so-called polar cap along magnetic field lines; the polar cap is essentially a region of open field lines. The open field lines are dragged by the solar wind to the magnetotail where they decouple from the IMF and form a closed field line once more. Energy released from tail reconnection accelerates plasma towards the Earth where it enters the plasma sheet, which is a population of cold plasma trapped in the magnetosphere containing ions and electrons from both the ionosphere and the solar wind; the inner edge of the plasma sheet is the source of Region 2 (R2) currents that map into the high-latitude ionosphere along closed field lines.

1.2 Ionosphere

The ionosphere is the layer of the Earth's atmosphere where neutral atoms undergo ionisation, resulting in a population of ions and electrons that form a plasma. There are two main sources of ionisation: solar radiation and, at high latitudes, particles precipitating along the magnetic field lines from the magnetosphere. Because the ion-electron pair formation processes depend on height, the established electron density profile has peaks at several heights, which define the E and F regions (Fig. 1.2).

The E region peak is located around 100 km altitude and is formed by the ionisation of O and N_2. Due to collisions, such as O with N_2^+ and O^+ with N_2, the most populous ion in the E region is NO^+. The E region rapidly disappears at night due to a lack of ionising photons and the recombination of NO^+ with electrons. Above the E region is

[1]The Geocentric Solar Magnetospheric (GSM) coordinate system is defined as follows: the origin is the center of the Earth; $\hat{x}$ is along the line connecting the center of the Earth to the center of the Sun; $\hat{y}$ is the cross product of the magnetic dipole axis and $\hat{x}$, with positive towards dusk; and $\hat{z}$ is the cross product of $\hat{x}$ and $\hat{y}$. The magnetic dipole axis is in the xz plane.

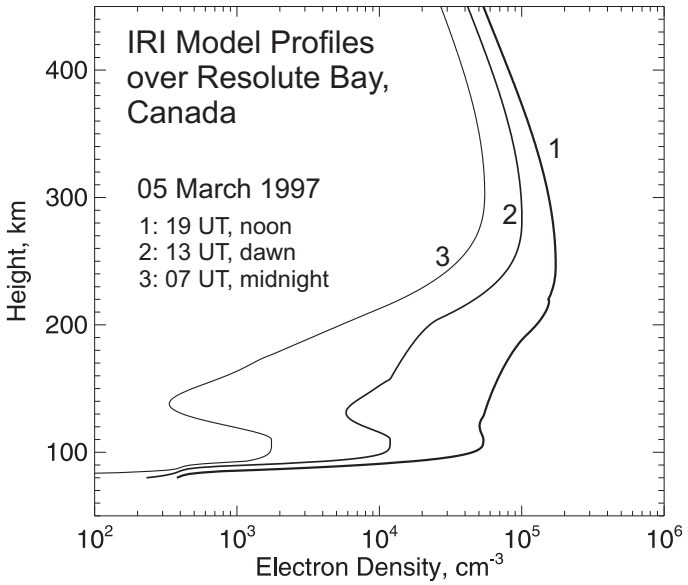

Figure 1.2: IRI model-derived electron density height profile of the ionosphere for noon, dawn, and midnight over Resolute Bay, Nunavut, Canada on March 5, 1997.

the F region, where N_2 concentrations are much lower than that of O. Here, the ionisation of O is the main source of electrons, with a peak electron density at $\sim$250 km. On the dayside, a deformation in the F region peak can occur, separating it into the F1 and F2 layers (Fig. 1.2, curve 1). While the density does diminish at night, the F region does not disappear like the E region because O^+ must be turned into NO^+ through collisions with less abundant N_2 to undergo recombination.

1.2.1 Ionospheric Convection

Ions and electrons in the ionosphere are in continuous motion. Plasma motion at high latitudes is driven primarily by quasi-static electric fields and the Earth's magnetic field, but is also affected by the winds through collisions with neutrals. For an electric field parallel to the magnetic field (or in absence of a magnetic field), the velocity of an ion relative to the neutral wind is $\mathbf{v}_{in} = q_i E / m_i \nu_{in}$, where ν_{in} is the ion-neutral collision frequency, m_i is the ion mass and $q_i = +e$ is the ion charge, where $e = 1.602 \times 10^{-19}$ C is the elementary charge; a similar equation holds for electrons, denoted by e subscripts instead of i, which denote ions. For an electric field perpendicular to a magnetic field, the equation of motion

for ions gives 2 velocity components, parallel to $\mathbf{E}$ and perpendicular to both $\mathbf{E}$ and $\mathbf{B}$:

$$\mathbf{v}_{in} = \frac{1}{1+\alpha_i^2}\left[\alpha_i \frac{\mathbf{E}_\perp}{B} + \frac{\mathbf{E}_\perp \times \mathbf{B}}{B^2}\right], \tag{1.9}$$

where $\alpha_i = \nu_{in}/\omega_i$ is the ratio of the ion-neutral collision frequency to the ion cyclotron frequency $\omega_i = q_i B/m_i$. For ions in the E region, the first term dominates, but above 120 km, where $\alpha_i \approx 1$, the second term dominates and the ions undergo what is known as $\mathbf{E}\times\mathbf{B}$ drift. Electrons, which follow a similar equation, will $\mathbf{E}\times\mathbf{B}$ drift above 80 km due to a much higher cyclotron frequency.

1.2.2 Ionospheric Electrodynamics

The parallel and perpendicular particle motions give rise to ionospheric currents. The current density is the sum of the ion and electron currents, $\mathbf{J} = n_i q_i \mathbf{v}_i + n_e q_e \mathbf{v}_e$, where n_i is the ion density and n_e is the electron density; the ionosphere is assumed to be quasi-neutral, $n_i \approx n_e$. The current density can be related to the electric field through the conductivity σ. Like velocity, currents and conductivities have 3 components: parallel to the magnetic field $\mathbf{B}$ (Birkeland or field-aligned current), parallel to $\mathbf{E}$ and perpendicular to $\mathbf{B}$ (Pedersen current) and in the $\mathbf{E}\times\mathbf{B}$ direction (Hall current). The parallel, Pedersen and Hall conductivities are respectively given by the expressions

$$\begin{aligned}
\sigma_\parallel &= n_i e^2 \left(\tfrac{1}{m_i \nu_{in}} + \tfrac{1}{m_e \nu_{en}}\right), \\
\sigma_P &= \tfrac{n_i e}{B}\left(\tfrac{\alpha_i}{1+\alpha_i^2} + \tfrac{|\alpha_e|}{1+\alpha_e^2}\right), \\
\sigma_H &= \tfrac{n_i e}{B}\left(\tfrac{1}{1+\alpha_i^2} - \tfrac{1}{1+\alpha_e^2}\right)
\end{aligned} \tag{1.10}$$

The full current density vector is given by Ohm's law $\mathbf{J} = \bar{\bar{\sigma}} \cdot \mathbf{E}$, where $\bar{\bar{\sigma}}$ is the conductivity tensor:

$$\bar{\bar{\sigma}} = \begin{pmatrix} \sigma_P & \sigma_H & 0 \\ -\sigma_H & \sigma_P & 0 \\ 0 & 0 & \sigma_\parallel \end{pmatrix} \tag{1.11}$$

The conductivities are height-dependent due to the collision and plasma frequencies, vary with the density of the neutral atmosphere, which decreases with height. Ohm's law is often written in 2-dimensional form for height-integrated conductivities, $\mathbf{I} = \bar{\bar{\Sigma}} \cdot \mathbf{E}$, where $\Sigma_H = \int_0^\infty \sigma_H(z)\mathrm{d}z$ (likewise for Σ_P), often referred to as the Hall (Pedersen) conductance.

The electric field primarily responsible for plasma motion in the high-latitude ionosphere is established via the field-aligned currents (Fig. 1.3a) that connect the ionosphere to the solar wind and magnetosphere. The current system closer to the pole is the R1 current system, generated by solar wind-magnetospheric coupling. The R1 current enters the ionosphere on the dawn side and exits on the dusk side, generating an electric field pointing in the dawn-to-dusk direction, which is the same direction that $\mathbf{E}_{sw}$ points for a southward IMF. The weaker R2 currents flow in the opposite direction, entering duskward and exiting dawnward. The electric field configuration from the two current systems (Fig. 1.3b) drives the F region plasma along a configuration known as a two-cell convection pattern (Fig. 1.3c).

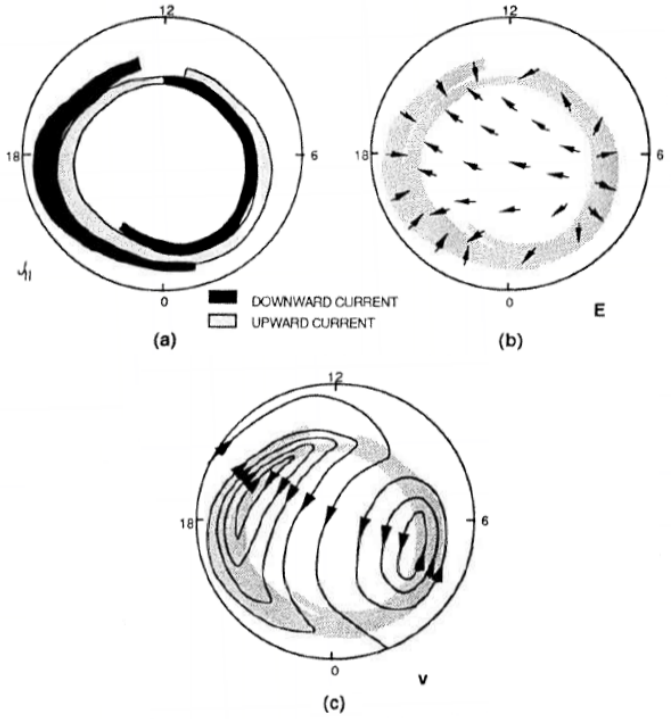

Figure 1.3: (a) Typical FAC distribution across the polar regions for a southward IMF. R1 currents are located poleward of the R2 currents. (b) Electric field distribution resulting from currents in (a). (c) Typical $\mathbf{E} \times \mathbf{B}$ drift pattern resulting from (b). (Modified from *Kivelson and Russell*, 1995).

Associated with the ionospheric electric field is an electric potential over the polar caps. The potential reaches a maximum in the dawn cell and a minimum in the dusk cell. The difference between the two is called the cross polar cap potential (CPCP). The CPCP

has an average value around 50 kV, but varies depending on solar wind and ionospheric conditions.

1.3 Coupling Function

The concept of the coupling function came along when researchers decided to find out a function describing the energy deposition into the Earth's ionosphere from known parameters of the solar wind and IMF. One benefit of having such a function is a capability of forecasting strong and harmful (for technological systems) space weather events.

Over the years, many coupling functions have been proposed. Some of them had theoretical arguments while others were introduced empirically. The southward component of the IMF, $B_z < 0$, has always been considered a key parameter as it controls the merging processes at the front-side magnetosphere (*Dungey*, 1961). As a result of merging, the interplanetary (solar wind) electric field $E_{sw} = v_x B_z$ is transferred, along the reconnected magnetic field lines, into the polar cap and thus a global-scale potential difference (CPCP) between the dawn and dusk sectors of the ionosphere is set. The CPCP drives the ionospheric current systems. Thus, the simplest coupling function could simply be B_z or the IEF.

Perrault and Akasofu (1978) took into consideration a contribution to merging from the IMF B_y component and proposed a formula, known now as the ε parameter:

$$\varepsilon = v_x B_T^2 \sin^4(\theta_c/2). \tag{1.12}$$

Here B_T is the magnitude of the IMF component in the Y-Z plane in the GSM coordinate system, θ_c is the IMF clock angle, defined as

$$\theta_c = \arctan(B_y/B_z). \tag{1.13}$$

The clock angle is measure clockwise from the positive B_z axis, such that for $B_y = 0$, $\theta_c = 0$ when $B_z > 0$ and $\theta_c = \pi$ when $B_z < 0$. Later on, the reconnection electric field, or Kan-Lee function, became more popular:

$$E_r = v_x B_T \sin^2(\theta_c/2). \tag{1.14}$$

For many years, no criterion existed for a better choice of the coupling function. *Newell et al.* (2007) suggested that the most relevant coupling function should have the best correlation with the parameters characterising energy deposition in the Earth's ionosphere. These authors found that the function

$$E_c = v_x^{4/3} B_T^{2/3} \sin^{8/3}(\theta_c/2) \tag{1.15}$$

has the best correlation with 10 parameters, including the Auroral Electrojet (AE) index, Disturbance storm time (Dst) index, and size of the polar cap.

A similar approach was followed by *Lyatsky et al.* (2007) who correlated their coupling function with the so-called Polar Cap North (PCN) magnetic index. The PCN index is derived from Thule magnetometer data (in the central polar cap) while correlating them with the parameters of the solar wind (*Troshichev et al.*, 2006). The PCN index is considered to be a good proxy for the reconnection electric field.

1.4 Objectives of the Undertaken Research

This thesis is aimed at investigation of the cross polar cap potential (CPCP), one of the major parameters characterising the electrodynamic state of the high-latitude ionosphere. Although at the beginning of the research the target was more specific, the phenomenon of CPCP saturation at strong external drivers, the project eventually evolved into a more general investigation of CPCP relationship/correlation with the parameters of the solar wind and interplanetary magnetic field. Such a broadening of the scope of the work happened after it was realised that the currently available CPCP data from the Super Dual Auroral Radar Network (SuperDARN) HF radars, the major instrument for the Thesis, are not really suitable for studying the saturation phenomenon.

The other issue, which has been around the SuperDARN CPCP estimates for a while, is the fact that these radars generally produce CPCP values that are smaller than estimates given by other techniques, first of all through direct ionospheric drift measurements on satellites, such as the Defense Meteorological Satellite Program (DMSP) satellites. How strong the effect is still needs to be established. In addition, the exact reasons for the

discrepancies have not been identified although a number of them have been discussed in the literature. In this view, further investigation of the potential reasons was undertaken. To address the issue, data from the Canadian High Arctic Ionospheric Network (CHAIN) ionosondes (that can measure the velocity of plasma motions at F region heights) were utilised.

More specific targets of the Thesis are:

1. Investigate the compatibility of the ionospheric plasma velocity measurements by the CHAIN ionosonde at Resolute Bay and the PolarDARN radars at Rankin Inlet and Inuvik. It should be noted that although $\mathbf{E} \times \mathbf{B}$ drift measurements from ionosondes are available for a number of locations and, in some places, for extended periods of time, insufficient efforts have been made in validating these instruments. This is an important issue since published results clearly indicate that the ionosondes can produce velocities that are quite different from the ones measured by the incoherent scatter radars (*Sedgemore et al.*, 1996, 1998; *Scali et al.*, 1995) and DMSP satellites (*Koustov et al.*, 2007). Besides general interest to the ionosonde performance as a method of plasma convection monitoring, there is another important aspect of validation work. In the future, velocity data from multiple ionosondes, especially in exotic places such as the Canadian High Arctic, could be very valuable as additional data for proper construction of the global-scale plasma convection maps and thus for derivation of the CPCP. It is then highly desirable to establish the compatibility between ionosonde velocities and velocities measured by the SuperDARN HF radars in a statistical sense, at least to have an idea about the general trends between the data. An interesting side aspect of ionosonde and HF radar velocity measurements is the fact that ionosondes operate at a frequency $\sim$3 times lower (4 MHz versus 12 MHz). It means that the index of refraction for ionosonde radio waves is smaller than that for the SuperDARN radars. It is well accepted now that the SuperDARN velocity is an underestimation of the real $\mathbf{E} \times \mathbf{B}$ ionospheric plasma drift (by at least 10%). It might be that the "index of refraction" effect is applicable to ionosonde measurements as well, and this would imply that ionosondes underestimate the $\mathbf{E} \times \mathbf{B}$ drift more than the SuperDARN radars do.

2. Establish whether the SuperDARN CPCP, inferred from the data of all SuperDARN radars, is proportional to the average velocity over the polar cap as measured by the Resolute Bay (RB) CADI ionosonde. Such a comparison makes sense even for a single-point velocity measurement since the plasma flow within the polar cap (extremely high latitudes) is expected to be uniform and a measurement in one spot does reflect the strength of the average plasma flow. Such a comparison allows one to conclude if the reasons for the SuperDARN CPCP underestimation is only the HF radar velocity underestimation effect.

3. Investigate the relationship/correlation of the CPCP with various parameters of the near-Earth space. Research in this area has been going on for almost three decades. Over the years, various instruments have been used, but none of these provided relatively long datasets covering periods of minimum and maximum solar activity. Importantly, current computer and analytical models are inadequate to describe empirical findings. In many previous publications, episodic data from various, perhaps drastically different, conditions were merged into a single database to reach reasonable statistics. With the SuperDARN data, these difficulties can be significantly alleviated. However, this is not to say that the SuperDARN data are continuous and without problems.

   The more specific issues of the investigation are as follows. First, the ones based on SuperDARN data that have not been published in the past are listed:

   - SuperDARN CPCP variation with the IMF B_z, B_y, B_T and solar wind velocity, each of the parameters being considered individually,
   - SuperDARN CPCP dependence on Alfvén-Mach number and Alfvén velocity,
   - SuperDARN CPCP as a parameter characterising the coupling function,
   - Inter-hemispheric differences including dependence on the IMF B_x and B_y.

   Effort was also put into confirming, on a different and usually larger database, the following dependences reported earlier, with various amounts of SuperDARN data

involved: SuperDARN CPCP dependence on IMF clock angle, interplanetary electric field, and solar wind pressure.

4. Test several quantitative theories predicting the CPCP variation with various parameters of the near-Earth space and comment on the areas of agreement and disagreement. It should be noted that several SuperDARN publications have dealt with this issue, for example the works by *Shepherd et al.* (2003), *Khachikjan et al.* (2008) and *Koustov et al.* (2009a). However, since then a couple of new theories have emerged. In addition, previous comparisons have been done with a database selected by hand-picking individual convection maps, which might be subjective. In this Thesis, more objective (not necessarily more relevant) criteria of data selection were adopted which makes it easy to double-check or reprocess obtained results.

1.5 Thesis Outline

The Thesis is organised as follows. In Chapter 2, what is known about the ionospheric CPCP experimentally is summarised and then a description of theoretical models predicting the CPCP is given. The emphasis is made on one theory, the Hill-Siscoe model, because it is the most advanced, widely cited and tested with various datasets. In Chapter 3, instruments whose data will be used in the Thesis are introduced: the SuperDARN radars, CADI ionosondes and satellite-based OMNI data. Chapter 4 is devoted to the investigation of the velocity data collected jointly by the Resolute Bay CADI and PolarDARN radars to establish the data compatibility, as well as the investigation into the relationship between SuperDARN CPCP and CADI velocities. Chapter 5 is an investigation of the SuperDARN CPCP relationship/correlation with various parameters of the solar wind. Finally, in Chapter 6, major findings of the Thesis are summarised and suggestions for future research are given.

CHAPTER 2

CROSS POLAR CAP POTENTIAL: EXPERIMENTAL FINDINGS AND THEORETICAL UNDERSTANDING

CPCP has been of interest to space physicists since the emergence of the concept of the IMF merging with the Earth's magnetic field because this parameter characterises the efficiency of energy delivery into to the Earth's (electrodynamic) environment. However, for CPCP measurements, ionospheric plasma data on a global scale are needed, and for a long time, this was partially achievable only with satellites and these have always been limited. Satellite measurements give convection along an individual path that might not pass through the foci of the convection cells so that the reported CPCP can be actually underestimated. Also, satellite measurements are not a "snapshot" of the ionosphere at a given time but sequential measurements made as the satellite crosses the polar cap, which may not reflect a rapidly-changing ionosphere. The introduction of the SuperDARN coherent radars provided opportunities for more regular measurements of the CPCP.

The CPCP has traditionally been considered to be dependent on the parameters characterising the near-Earth space. Over the years, several such functions were introduced, mostly reflecting efficiency of the merging processes, although the exact mechanisms were largely unknown. These functions, while having some physical significance, are nevertheless empirical and there is no clear preference to a single one. The most popular parameters considered are the IEF, Akasofu-Perrault ε parameter and the reconnection electric field E_r (Equation 1.14). In some studies, the PCN index was considered.

2.1 Experimental Findings on the CPCP and its Dependence on Plasma Parameters of Near-Earth Space

The first investigations of the ionospheric CPCP were reported in the 1980s. *Reiff et al.* (1981) considered Dynamic Explorer (DE-C, DE-D) and S3-3 data and found linear CPCP variation with IMF B_z, IEF, E_r and ε. The correlation coefficient ranged from 0.59 (IMF magnitude) to ∼0.9 (ε parameter). The correlation with the solar wind velocity was found to be very low, r = 0.04. The highest CPCPs in the study were ∼120 kV. *Wygant et al.* (1983) considered S3-3 satellite data, which orbited at heights ranging from 240 to 8040 km, and found that typical CPCP values were 40-80 kV. They noticed a saturation effect of the CPCP to ∼120 kV for strong values of ε.

Doyle and Burke (1983) reported the same maximum values of the CPCP but did not identify the effect of saturation while plotting CPCP against $V_{sw}\ B\ \sin^2(\theta_c/2)$. The empirical model of *Weimer* (1995) based on DE-2 satellite data predicts maximum CPCP values of 120 kV for southward IMF and ∼30 KV for northward IMF. For IEF > 3 mV/m, though, the DE-2 data showed some tendency for saturation.

Troshichev et al. (1996) analyzed several cross-polar passes of the EXOS-D satellite and reported a linear dependence of the CPCP versus the PCN index. The correlation coefficient of the dependence was found to be 0.82, but maximum IMF values were only ∼10 nT.

de la Beaujardiere et al. (1991) considered incoherent scatter radar data. The range of the CPCP was found to be smaller with average values around 50 kV. Seasonal variation was reported with the strongest CPCP being in the fall, followed by winter, spring and summer. It is worthy to note that the differences were small, on the order of several kV.

More comprehensive CPCP studies have been performed with ion drift meters on DMSP satellites (*Boyle et al.*, 1997). These authors used about 58,000 crossings of the polar cap and found that the CPCP is strongly dependent on the IMF; as the IMF becomes more and more negative, the CPCP increases from the IMF-independent values of ∼16 kV (for $V_{sw} \sim 400$ km/s). The IMF B_y effect was less obvious, as well as the dependence on

the plasma density. When the solar wind velocity increased, the CPCP increased; however, this increase was not strong so that no CPCP variation with solar wind pressure was found. Fitting all the data available to a single equation, *Boyle et al.* (1997) arrived to the empirical formula

$$\Phi_B = 10^{-4} v_x^2 + 11.7 B \sin^3(\theta_c/2). \tag{2.1}$$

The above equation implies that there is no CPCP saturation effect at large v_x and B, in contrast with other studies. It is interesting that the average potential was found to be $\sim$10 kV larger during equinoxes as compared to winter/summer time. Winter CPCPs are larger than summer CPCPs by $\sim$5 kV.

Boyle et al. (1997) also reported an increase of the CPCP with the K_p index, a measure of disturbances in the horizontal component of the Earth's magnetic field, by presenting a plot with a near linear dependence of the CPCP upon K_p up to $K_p \sim 6$. Because of a general interest with plasma parameters during great storms in the early 2000s, *Hairston et al.* (2003) made a focused study of the CPCP for the strongest storms and found deviations from linearity with $E = V_x B_T$, although the saturation per se has not been seen. The maximum CPCP values were as high as 400 kV, although typical values were up to $\sim$250 kV. Later data on CPCP during superstorms (*Hairston et al.*, 2005) were plotted as a function of the reconnection electric field, convincingly demonstrating the CPCP saturation effect in DMSP data. It should be stressed that the *Weimer* (1995) DE2 satellite drift data did not show large CPCPs of $\sim$250 kV and the reasons for such large discrepancy with DMSP measurements for different periods is worth understanding.

A new era in CPCP studies began with the introduction of SuperDARN global-scale convection maps in the early 2000s (*Shepherd and Ruohoniemi*, 2000; *Shepherd et al.*, 2002; *Bristow et al.*, 2004). It was clear from the very beginning that SuperDARN CPCP increases with the IMF strength but maximum CPCP values do not normally exceed 100 kV. A more systematic study of the CPCP dependence on IMF and solar wind conditions was undertaken by *Shepherd et al.* (2003). The selected dataset showed CPCP values below 80 kV for moderate reconnection electric fields. A saturation effect was found to begin starting from $E_r \sim 2$ mV/m. No clear dependence on the solar wind pressure was found. The saturation effect of the CPCP was also obvious in data presented by *Bris-*

tow et al. (2004) and a later paper by *Khachikjan et al.* (2008). *Khachikjan et al.* (2008) insisted that the threshold for the saturation effect is $\sim$3 mV/m, in terms of the IEF. Extending that analysis, *Koustov et al.* (2009a) undertook a focused study by hand-selecting data with good coverage in both hemispheres and found that the threshold for the CPCP saturation occurs indeed at $\sim$3 mV/m, for both the E_r field and the IEF and in both hemispheres. The threshold in terms of PCN index was found to be 3, in clear disagreement with results by *Troshichev et al.* (1996) who did not see saturation even at PCN = 5. Interestingly, in terms of the trend, the saturation effect was shown to start earlier and achieve the saturated values faster during winter as compared to summer. *Koustov et al.* (2009a) also reported that for about 150 points of simultaneous data in the northern and southern hemispheres, sunlit ionosphere had larger CPCP, contrary to theoretical expectations and DMSP measurements by *Boyle et al.* (1997). Finally, it was found that the entire SuperDARN database does not have CPCP values above 120 kV, which identifies the major disagreement between the ground-based and satellite measurements of the CPCP.

Very similar results were obtained by *Grocott et al.* (2009), who created a SuperDARN CPCP database by simply imposing a condition on the number of vectors available for the CPCP estimates. Specifically, they selected the value of 200. These authors showed that the CPCP is well described by the $\sin^2(\theta_c/2)$ clock angle function. They selected as the plotting parameter the IEF multiplied by the $\sin^2(\theta_c/2)$ term. The CPCP was shown to grow almost linearly with this parameter at small values and it saturates at large values. The CPCP was found weakly dependent on the solar wind magnetosonic Mach number.

SuperDARN studies indicate that the CPCP estimates at large IEFs could be erroneous. Some of these reasons will be discussed in Chapter 3. Here another reason will be mentioned, one more widely accepted by the SuperDARN community. It is well known that as the IMF becomes more and more negative, the auroral oval, characterising areas with strong particle precipitation and enhanced E fields, expands equatorward so that the radars either lose echoes or may detect E region echoes, which have velocities well below $\mathbf{E} \times \mathbf{B}$ plasma drift. *Baker et al.* (2007) attempted to include data from the mid-latitude Wallops Island radar into the analysis. For the event considered, they were able to show that the CPCP is about 20 kV larger than the one estimated without considering the mid-latitude

data.

A number of studies estimated the CPCP from the magnetometer data using the Assimilative Mapping of Ionospheric Electrodynamics (AMIE) approach (*Richmond and Kamide*, 1988; *Richmond*, 1992). In terms of maximum CPCP values, these studies are roughly in agreement with DMSP measurements, i.e. maximum values can be of several hundred kV, although *Kihn et al.* (2006) showed that while there is linearity between AMIE and DMSP, statistically DMSP CPCP can be greater than AMIE CPCP by as much as 25%. The AMIE-produced CPCPs do show saturation effect but to very high values, greater than 200 kV. There is disagreement regarding the threshold IEF starting from which the nonlinearity begins. While *Russell et al.* (2001) identified it as $\sim$3 mV/m, *Liemohn and Ridley* (2002) argued that it is actually as large 10 mV/m.

Recently, multi-year data from electric field instruments on CLUSTER satellites have been processed to infer a statistical convection pattern and estimate the CPCP (*Haaland et al.*, 2007; *Förster et al.*, 2007). These studies showed CPCPs up to 100 kV, somewhat larger than the ones known from SuperDARN measurements and measurements on DMSP satellites (e.g., *Papitashvili and Rich*, 2002). An almost linear increase with E_r and IMF B_T was reported. A deviation from linear trends was noticed starting from E_r = 2 mV/m. A weak positive correlation with the solar wind ram pressure was reported. However, for small solar wind ion densities, suggesting a low ram pressure, the CPCP showed some decrease. Another interesting conclusion is that CPCPs in the northern and southern hemispheres were found to be very close to each other, implying that the effect of conductance is insignificant. The only clearly identified effect was a summer increase in average electric field for quiet conditions, given as D_{st} > -30 nT, where D_{st} is the disturbance storm time index, a measure of the fluctuations in the Earth's magnetic field strength.

The saturation of the CPCP has been also articulated in terms of typical/average velocity of the plasma flow across the central polar cap. *MacDougall and Jayachandran* (2001, 2006) considered convection data gathered by CADI ionosondes deep in the polar cap, at Eureka (magnetic latitude (MLAT) = 88.7°) and Resolute Bay (MLAT = 83.6°). Originally, the plots of the ionosonde velocity versus IMF B_z were interpreted in terms of linear dependencies (*MacDougall and Jayachandran*, 2001), despite that some saturation

had been seen. Later (*MacDougall and Jayachandran*, 2006), similar data were shown to have a saturation at $|B_z| >$ 3-5 nT. The saturation effect in the velocity was more clearly seen in DMSP data (*Troshichev et al.*, 2000) and PolarDARN HF radar velocity data (*Fiori et al.*, 2009) once the velocities were plotted against the PCN magnetic index. These studies indicated that the threshold for saturation to begin was of the order of PCN $\sim$ 3 and 2, respectively.

Lastly, a number of studies have investigated the CPCP dependence upon external drivers for sunlit (high-conducting) and dark (low-conducting) ionospheres. *Boyle et al.* (1997) noticed that CPCPs are larger during equinoxes and smallest during summer. The differences though are on the order of 5 kV. Cluster CPCPs are almost independent on the conductance (*Haaland et al.*, 2007; *Förster et al.*, 2007). However, AMIE modelling by *Ridley and Kihn* (2004) shows a very strong dependence on conductance for the convection velocity and, although much weaker, for the CPCP; they showed $\sim$2 times larger rates of average velocity increase with the PCN index for summer conditions (as compared to winter conditions) and only $\sim$1.1 times larger for the CPCP. *Förster et al.* (2007) showed some dependence for the velocity (but none for the CPCP) in their CLUSTER data. *Fiori et al.* (2009), by considering PolarDARN radar data, did not confirm the above results regarding velocity variation.

Interesting results have been reported very recently by *Pettigrew et al.* (2010) and *Cousins and Shepherd* (2010). These authors reconsidered the SuperDARN database for 1998-2002 and created a new convection model, more flexible than the one developed earlier by *Ruohoniemi and Greenwald* (2005). *Cousins and Shepherd* (2010) found that the new CPCPs are $\sim$10% larger than the ones reported previously from SuperDARN data. From their more detailed analysis of SuperDARN data, *Pettigrew et al.* (2010) showed that CPCP in the south to be systematically larger than the CPCPs in the north for negative IMF B_z. The differences between hemispheres are less than 10% on average, but the strength of the convection in the individual cells can differ by 15% to 20% on average. This is in contrast to *Koustov et al.* (2009a) who observed larger CPCPs for the sunlit (summer) hemisphere and a similar result was reported by *Shepherd* (2007). It should be noted that the former two papers used the standard SuperDARN processing software and this might

be the reason for different results. *Cousins and Shepherd* (2010) believe that this is not the correct approach as the startup convection models that they developed are apparently somewhat different between the two hemispheres. This result, however, poses questions as to what extent the SuperDARN CPCPs are affected by the startup convection model (see Discussion in *Koustov et al.* (2009a)). For this reason, it is worth performing a statistical study of the CPCP with the model-independent approach by *Fiori et al.* (2010).

2.2 The Hill-Siscoe Model: a Theory of the Cross-Polar Cap Potential Formation

One of the more advanced theories predicting the CPCP dependence on parameters of the solar wind, including the saturation effect, was introduced by *Hill et al.* (1976) and improved upon by *Siscoe et al.* (2002b), who specified the physics involved and combined it with results from magnetohydrodynamic (MHD) simulations. In this section, major points and arguments of this theory are described.

2.2.1 Derivation

Hill et al. (1976) proposed that the CPCP is limited by 2 factors: the total electrical energy available from the solar wind and a feedback process that restricts the maximum intensity of the Region 1 current system. The overall expression for the CPCP was introduced as a combination of these two values:

$$\Phi_{PC} = \left(\frac{1}{\Phi_m} + \frac{1}{\Phi_S} \right)^{-1}, \tag{2.2}$$

where Φ_m is the magnetospheric potential, the electric potential applied by the solar wind across the dayside magnetopause, and Φ_S is the saturation potential, the maximum potential that is achievable across the ionosphere through the R1 current system. In this form, the CPCP remains less than the minimum of the two potentials and under strong solar wind conditions, $\Phi_m \gg \Phi_S$, $\Phi_{PC} \approx \Phi_S$, which implies saturation.

The CPCP formulation given by *Hill et al.* (1976) is

$$\Phi_m \leq v_A B_{sh} R_{ms}, \tag{2.3}$$

$$\Phi_S \leq \frac{R_{ms} B_d}{\mu_0 \Sigma_P}, \tag{2.4}$$

$$\Phi_{PC} \leq \frac{\Phi_m}{1+\frac{\Sigma_P}{\Sigma_0}} = \frac{v_A B_{sh} R_{ms} B_d}{B_d + \Sigma_P \mu_0 v_A B_{sh}}, \tag{2.5}$$

where B_{sh} is the strength of the IMF in the magnetosheath, $B_d \approx \sqrt{2\mu_0 p_{sw}}$ is the strength of Earth's magnetic dipole at the magnetopause, and $\Sigma_0 \equiv B_d/(B_{sh}\mu_0 v_A)$ is called the critical conductivity, the point where saturation becomes important. Φ_S can be derived by equating the Poynting flux to resistive losses in the ionosphere, i.e. Joule heating.

Siscoe et al. (2002b) expanded the initial concept of *Hill et al.* (1976) by detailing the processes of the solar wind electric field mapping to the ionosphere from the merging site, assumed to be the stagnation point at the front of the magnetopause. According to *Siscoe et al.* (2002b), the CPCP is generated primarily by the R1 currents following Ohm's law:

$$I_1 = \xi \Sigma_P \Phi_{PC}, \tag{2.6}$$

where Σ_p is the height-integrated ionospheric Pedersen conductance and ξ is a magnification factor dependent on the geometry of the currents flowing into the ionosphere. MHD simulation runs showed this to be $\xi = 4.45 - 1.08\log\Sigma_P$, which typically has a value between 3 and 4.

The magnetospheric potential Φ_m is the potential applied across the magnetopause by E_{sw}. It is defined by *Siscoe et al.* (2002b) as

$$\Phi_m = \chi E_r L_{r0}, \tag{2.7}$$

where L_{r0} is the length of the reconnection line and χ is the magnetosheath compression factor, which accounts for changes in the solar wind plasma and the IMF after entering the magnetosheath:

$$\chi = 4 f_r (2\kappa\rho_{sw}/\rho_{sh})^{1/2}. \tag{2.8}$$

Here f_r is the reconnection efficiency (typical value of 0.1), ρ_{sh} is the plasma mass density in the magnetosheath, ρ_{sw} is the solar wind mass density, and κ is the ratio of the total

solar wind pressure at the magnetopause to the upstream pressure. The coefficients are from the compression of the IMF through the bow shock and magnetosheath. The magnetosheath compression factors come from an aerodynamic model (*Spreiter et al.*, 1966), which serves as a reasonable approximation. In particular, $\rho_{sh}/\rho_{sw} = r$ (Eq. 1.2) for the limit where $M_A \to \infty$, since the aerodynamic model does not include magnetic contributions. The compression factors are dependent upon the solar wind Mach number. For typical Mach numbers, around 7-8, κ is 0.884 and the density in the magnetosheath is a factor of about 3.8 higher than the upstream density, giving $\chi = 0.27$. The length of the reconnection line is assumed to be 30 $R_E\, p_{sw}^{-1/6}$.

With all of these values considered, Equation (2.7) becomes

$$\Phi_m(\mathrm{kV}) = 57.6 E_r(\mathrm{mV/m})\, p_{sw}^{-1/6}(\mathrm{nPa}). \tag{2.9}$$

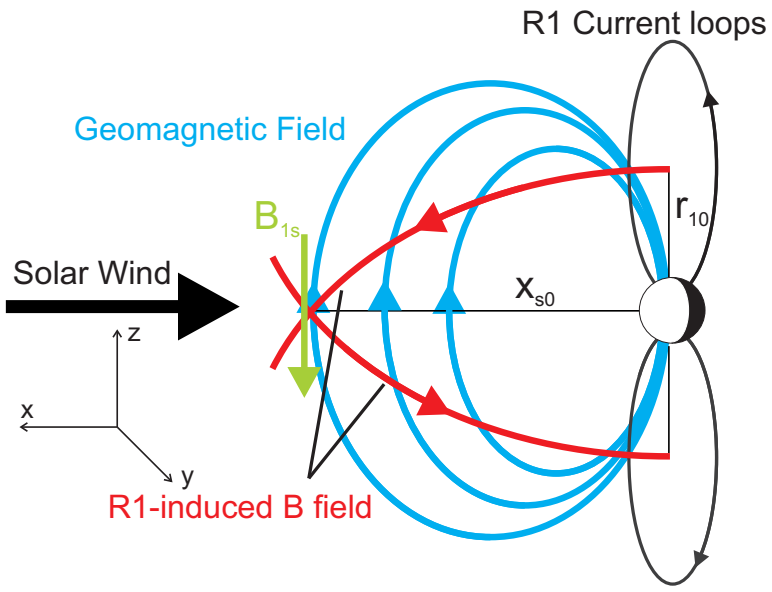

Figure 2.1: R1 current loops in the terminator plane, generated southward magnetic field at the stagnation point (red), and the Earth's dipole field (blue).

The saturation mechanism in the Hill-Siscoe model is the weakening of the geomagnetic field at the stagnation point by the R1 currents (Figure 2.1). The geometry of the R1 currents implies that they generate a net southward magnetic field at the stagnation point, opposing the northward geomagnetic field. As a result, the magnetic field strength at the stagnation point is reduced and the merging rate is decreased as well, weakening the R1

currents. Hill postulated that when the R1 current-generated magnetic field is a significant fraction β (about 1/2) of the value of the geomagnetic field at the stagnation point, the R1 currents become saturated. MHD simulations by *Siscoe et al.* (2002b) found that $\beta = 0.41$ fits best.

Assuming that the R1 currents are closed through the magnetopause in the terminator plane and approximating the R1 currents as two circular loops, one in each hemisphere, the magnetic field generated by these currents at the stagnation point, determined by the Biot-Savart law, is

$$B_{1s}(\mathrm{nT}) = 2.8\,\mu_0 I_1(\mathrm{MA})\,p_{sw}^{1/6}(\mathrm{nPa}). \tag{2.10}$$

The dependence upon solar wind pressure in Equation 2.10 exists due to the involvement of the size of the magnetosphere in the calculation. Using Hill's postulate, Equation 2.10 is equal to $0.41\,B_d$ when $I_1 = I_S$. Here, $B_d = \sqrt{2\mu_0 p_{sw}}$ is the strength of the geomagnetic field at the stagnation point. This implies that the saturated R1 current is

$$I_S(\mathrm{MA}) = 4.61\,p_{sw}^{1/3}. \tag{2.11}$$

The saturation potential is related to the saturated R1 current via Ohm's law:

$$\Phi_S(\mathrm{kV}) = \frac{4610\,p_{sw}^{1/3}}{\xi\Sigma_P}. \tag{2.12}$$

The final form obtained from Equation 2.2 is

$$\Phi_{PC} = \frac{57.6\,p_{sw}^{1/3}E_r}{p_{sw}^{1/2} + 0.0125\xi\Sigma_P E_r}. \tag{2.13}$$

While Equation 2.13 looks different from Equation 2.5, the basic form is still intact. $v_A B_{sh}$ is effectively an electric field, which parallels E_r, and the p_{sw} terms are obtained by $R_{ms} \propto p_{sw}^{-1/6}$ and $B_d \propto p_{sw}^{1/2}$.

2.2.2 Predictions

Figure 2.2a shows some conclusions that can be made from Equation (2.13). Using baseline values of p_{sw} = 1 nPa, Σ_P = 6 S, and $\theta_c = \pi$, it can be seen that the CPCP (solid line labelled Baseline) is roughly equal to the magnetospheric potential (dotted line) for low

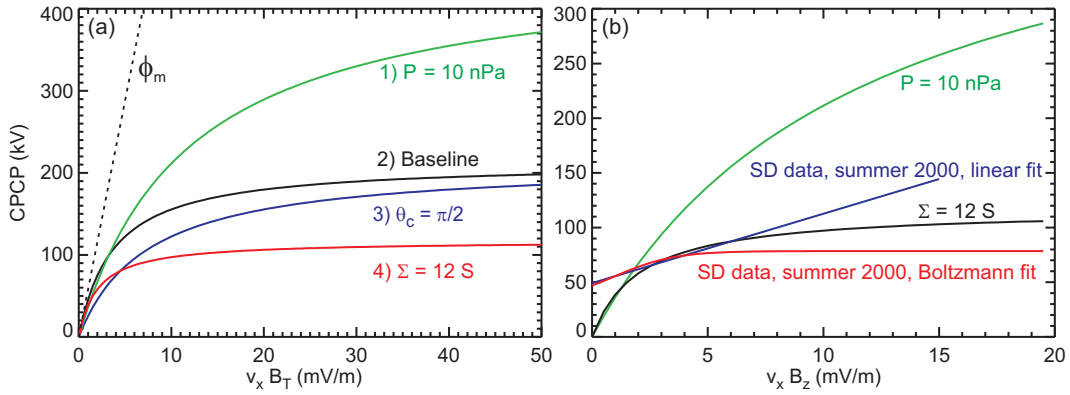

Figure 2.2: (a) CPCP predictions of the Hill-Siscoe model versus solar wind electric field for various parameters. The baseline (2) uses parameters $p_{sw} = 1$ nPa, $\theta_c = \pi$ and $\Sigma_P = 6$ S. Curves (1), (3) and (4) use the baseline values for parameters not listed on the plot. (b) Linear and Boltzmann fits for SuperDARN CPCP data from summer 2000 and curves (1) and (4) from (a).

values of E_{sw}, but deviates at about 3 mV/m, where saturation starts to become apparent. When the pressure is increased to 10 nPa (top curve), the CPCP saturates at a much higher potential, implying that the saturation effect is less pronounced at higher pressures. Doubling the conductance, however, reduces the saturation value to nearly half of the baseline (Σ_P = 12 S curve). The $\theta = \pi/2$ curve shows more typical IMF conditions. The saturation level is not affected by the clock angle, but it takes a larger E_{sw} to reach the same potential as the baseline.

Figure 2.2b shows how the Hill-Siscoe model predictions compare to data obtained from the SuperDARN radars (see Section 5.11 for further discussion). Curves (1) and (4) from Figure 2.2a are shown compared to linear and Boltzmann fits to CPCP data from April-July 2000. It should be noted that although the x-axis for each graph uses a different expression for the electric field, they are equivalent under the assumption $\theta_c = \pi$, which implies that $E_r = v_x B_z$ for $B_z < 0$.

2.3 MHD Modelling

When one models the near-Earth environment with MHD equations, it is very natural to look at the dependence of the CPCP upon the solar wind parameters. The development of the Hill-Siscoe model has always been based on results of MHD modelling. It is not

a surprise that the proponents of this scenario linked the saturation to the limiting of R1 FACs. It was shown that as R1 currents reconfigure, they usurp and eventually replace the Chapman-Ferraro currents at the magnetopause and create a $\mathbf{J} \times \mathbf{B}$ force to withstand the solar wind dynamic pressure *Siscoe et al.* (2002a). The other effect of the R1 currents is a decrease in the magnetic field intensity on the frontside magnetopause and thus a reduction in the reconnection rate. These are two sides of the same process.

Merkin et al. (2005a) and *Merkin et al.* (2005b) stress the importance of the magnetospheric "flaring," where the shape of the dayside magnetopause becomes more obtuse, which reduces the reconnection rate. Their claim is that the changes in magnetopause shape are produced by an increase of the ionospheric conductance. *Raeder and Lu* (2005) noticed that the compression and erosion of the magnetosphere by the solar wind under strong conditions causes the stagnation point to move inward significantly, forming a dimple in the magnetosphere. As a result, the plasma flow is stagnated, reducing the reconnection rate.

Siscoe et al. (2004) further note that the results from *Merkin et al.* (2005b), *Raeder and Lu* (2005), and *Siscoe et al.* (2002a) are all equivalent interpretations of the same phenomenon. The R1-generated magnetic field that weakens the dipole field at the nose of the magnetopause can also explain the dimple effect. The dimple formation also leads to a broadening of the magnetosphere, which is equivalent to the "flaring" mentioned by *Merkin et al.* (2005b).

Results of MHD modelling with respect to CPCP, published so far, are somewhat inconsistent with the proposed analytical theories. For example, *Borovsky et al.* (2009) fixed parameters of the solar wind and investigated the CPCP for two values of the ionospheric conductance, 5 and 20 S. They discovered that the CPCP decreases dramatically for larger conductance. They claim that the solar wind acts as a voltage generator that produces limited current.

A note must be made that computer modelling does not allow us to address the question of what the maximum CPCP that can be achieved is, as many parameters of the modelling are not well known. However, the insights provided are useful.

2.4 Kivelson-Ridley Alfvén Wing Formulation

Ridley (2007) and *Kivelson and Ridley* (2008) formulated a theory of saturation based on the formation of "Alfvén wings" at low Mach numbers. Alfvén wings are flux tubes that are caused by the reflection of Alfvén waves in the R1 FACs incident to the ionosphere. For typical Alfvén-Mach numbers, > 8, the angle of the Alfvén wings is small enough such that they are indistinguishable from the magnetotail, but at low Alfvén-Mach number, ∼2, they appear at higher angles, an effect similar to the magnetosphere flaring out at the flanks described by *Merkin et al.* (2005b).

The reflection of the Alfvén waves results in the partial reflection of the solar wind electric field, leading to saturation under low M_A conditions, typically indicating a strong solar wind. The transmitted electric field is given as

$$E_t = E_i \frac{2}{1+\frac{\Sigma_P}{\Sigma_A}} \tag{2.14}$$

where

$$\Sigma_A = \frac{1}{\mu_0 v_A} \tag{2.15}$$

is the Alfvén conductance of the solar wind. The amount of reflection is dependent on the ratio of Pedersen conductance to Alfvén conductance. It should be noted that this is very similar to the formulation given by *Hill et al.* (1976) in Equation 2.5.

The CPCP formula given by *Kivelson and Ridley* (2008) is obtained by using the reconnection electric field as the incident electric field, $E_i = E_r$, which is converted to a potential by multiplying by a distance, $D = 0.1\pi R_{ms}$. The v^2 quasi-viscous term from *Boyle et al.* (1997) is also included. The final equation is

$$\Phi_{KR} = 10^{-4} v_x^2 + 0.2\pi E_r R_{ms} \frac{1}{1+\mu_0 v_A \Sigma_P}. \tag{2.16}$$

Lyatsky et al. (2010) also added to the theory in terms of the ionospheric conductance. Instead of a uniform ionospheric conductance, two conductances were used, one for the polar cap and one for the auroral oval, where it is assumed that the conductance is higher from particle precipitation.

2.5 Other Theories of CPCP Saturation

Among others, the simplest suggestion for the saturation mechanism is that the length of the reconnection line on the dayside magnetopause is not increasing proportionally to the applied IEF (*Ridley*, 2005; *Khachikjan et al.*, 2008). Ridley also takes into account the effect of the Alfvén-Mach number, which tends to be small for large CPCP. For small M_A, the increase in IMF strength across the bow shock (Eq. 1.2) is not as large, which may also contribute to saturation. He proposes the following formula for the CPCP:

$$\Phi_R = \left[10^{-4} v_x^2 + 11.7 B_T \sin^3(\theta_c/2)\left(1 - e^{-M_A/3}\right)\right] \frac{R_{ms}}{9}. \tag{2.17}$$

This is a modification of Boyle's formula, with the addition of the M_A and R_{ms} terms.

MacDougall and Jayachandran (2006) suggested that the CPCP is also affected, in significant way, by the Region 2 FACs. In their argument, the voltage across the polar cap is supported by a magnetospheric current generator, and not a magnetospheric voltage generator as assumed, for example, in the Hill-Siscoe formulation. *MacDougall and Jayachandran* (2006) argued that with an increase of the magnitude of negative IMF B_z, the R2 currents become progressively more intense as compared to the R1 currents, and this effectively slows down the increase in the cross polar cap flow velocity (and the CPCP) as, progressively, larger and larger portions of R1 FACs becomes closed not through the polar cap but through "local loop" R2 Pedersen currents across the auroral oval. To support this scenario, *MacDougall and Jayachandran* (2006) demonstrated that with an increase in magnitude of B_z, the partial ring current (the source of R2 currents), characterised by the horizontal asymmetric (Asym-H) magnetic index, increases even faster. In criticising this explanation, *Siscoe and Siebert* (2007) agreed that the R2 effects cannot be denied but they point out the fact that computer codes successfully explain the CPCP saturation, although at levels about 2 times larger than the observed ones, without involving complex processes of R2 current creation. At the same time, they also acknowledge that MHD models (upon which *Siscoe et al.* (2002b) based their theory) are not suitable to model R2 currents of observed strength, due to particles in the inner magnetosphere, where R2 currents are generated, being dominated by particle drift physics and not MHD equations.

The importance of R2 currents, as well as an increase in the conductance of the auroral oval region of the ionosphere, have been stressed by *Liu* (2007) who argued on the basis of energy conservation principles that the CPCP, being dependent upon these factors, should saturate at strongly driven conditions.

Kan et al. (2010) focused on the fact that as the IMF B_z magnitude increases, auroral oval conductance increases as well, with a nonlinear relationship. They formulated the model in analogy with electric circuit with the oval resistance being fed by both R1 and R2 current loops. The current loops also have magnetospheric resistances. On the dayside, the loop resistance reflects the energy dissipation in the reconnection regions: bow shock, magnetosheath and LLBL. On the nightside, the loop resistance is due to collisionless dissipation in the plasma sheet. The saturated level of the CPCP was found to strongly depend on the actual values of the above resistances. An important assumption of this theory is that the auroral oval conductance is linearly proportional to E_r; it needs to be tested in future. The authors believe that the saturation potential is controlled by the length of the merging line on the dayside.

CHAPTER 3

INSTRUMENTATION

This Thesis considers data from multiple instruments. Two major ones are the Super Dual Auroral Radar Network (SuperDARN) HF radars and the Canadian Advanced Digital Ionosondes (CADI). Data was also considered from a number of instruments on satellites flying upstream from the Earth; these are summarised by the OMNI dataset (ftp://nssdcftp.gsfc.nasa.gov/spacecraft_data/omni/).

3.1 The Super Dual Auroral Radar Network

SuperDARN is a system of coherent HF radars positioned around the northern and southern polar regions with a major goal to continuously monitor plasma convection in the high-latitude ionosphere (*Greenwald et al.*, 1995). The radars are designed to transmit radio waves into the ionosphere obliquely and detect echoes that scatter off ionospheric structures such as plasma irregularities. There are currently 24 radars in operation, 16 in the northern hemisphere and 8 in the southern hemisphere. The positions of the radars and their fields-of-view are presented in Figure 3.1 and their coordinates and boresight directions are shown in Table 3.1. Coordinates are given in geographic and altitude-adjusted corrected geomagnetic (AACGM) coordinates. Radars used in this study are marked with an asterisk in Table 3.1; there are 10 northern radars and 5 southern radars. Two of the radars, at Rankin Inlet (see shaded FoV in Fig. 3.1) and paired with it the radar at Inuvik, are called PolarDARN; data from these two radars will be additionally used in combination with CADI ionosonde measurements at Resolute Bay (Fig. 3.1, solid red dot).

The plasma irregularities that SuperDARN detects are fluctuations in electron density that, in the F region, are commonly attributed to the gradient drift plasma instability. The

Table 3.1: SuperDARN radar locations and boresight directions. Radars used in this Thesis are marked with asterisks.

Radar Station	Geog. Lat. (°N)	Geog. Long. (°E)	AACGM Lat. (°N)	AACGM Long. (°E)	Boresight Direction (°)
Goose Bay*	53.32	-60.46	61.94	23.02	5.0
Kapuskasing*	49.39	-82.32	60.06	-9.22	-12.0
Saskatoon*	52.16	-106.53	61.34	-45.26	23.10
Prince George*	53.98	-122.59	59.88	65.67	-5.0
Kodiak*	57.60	-152.2	57.17	-96.28	30.0
Stokkseyri*	63.86	-22.02	65.04	67.33	-59.0
Þykkvibær	63.86	-19.2	64.59	69.65	30.0
Hankasalmi*	62.32	26.61	59.78	105.53	-12.0
King Salmon*	58.68	-156.65	57.43	100.51	-20.0
Wallops Island	37.93	-75.47	30.63	75.52	35.86
Blackstone	37.10	-77.95	48.59	-3.627	-32.0
Hokkaido	43.53	143.61	38.14	-145.67	30.0
Inuvik*	68.42	-133.5	71.58	-87.40	29.47
Rankin Inlet*	62.82	-93.11	73.25	-28.23	5.71
Fort Hayes West	38.86	-99.39	49.30	-33.28	-25.0
Fort Hayes East	38.86	-99.39	49.30	-33.28	45.0
Sanae*	-71.68	-2.85	-61.52	43.18	173.20
Syowa South*	-69.00	39.58	-55.25	23.00	165.0
Syowa East*	-69.01	39.61	-55.25	22.98	106.5
TIGER*	-43.38	147.23	-55.31	-133.36	180.0
Kerguelen*	-49.35	70.26	-58.73	122.14	168.0
Unwin	-46.51	168.38	-55.15	-106.54	-132.1
McMurdo	-77.88	166.73	-80.00	-33.39	-96.6
Falkland Islands	-51.83	-58.98	-38.30	9.91	178.20

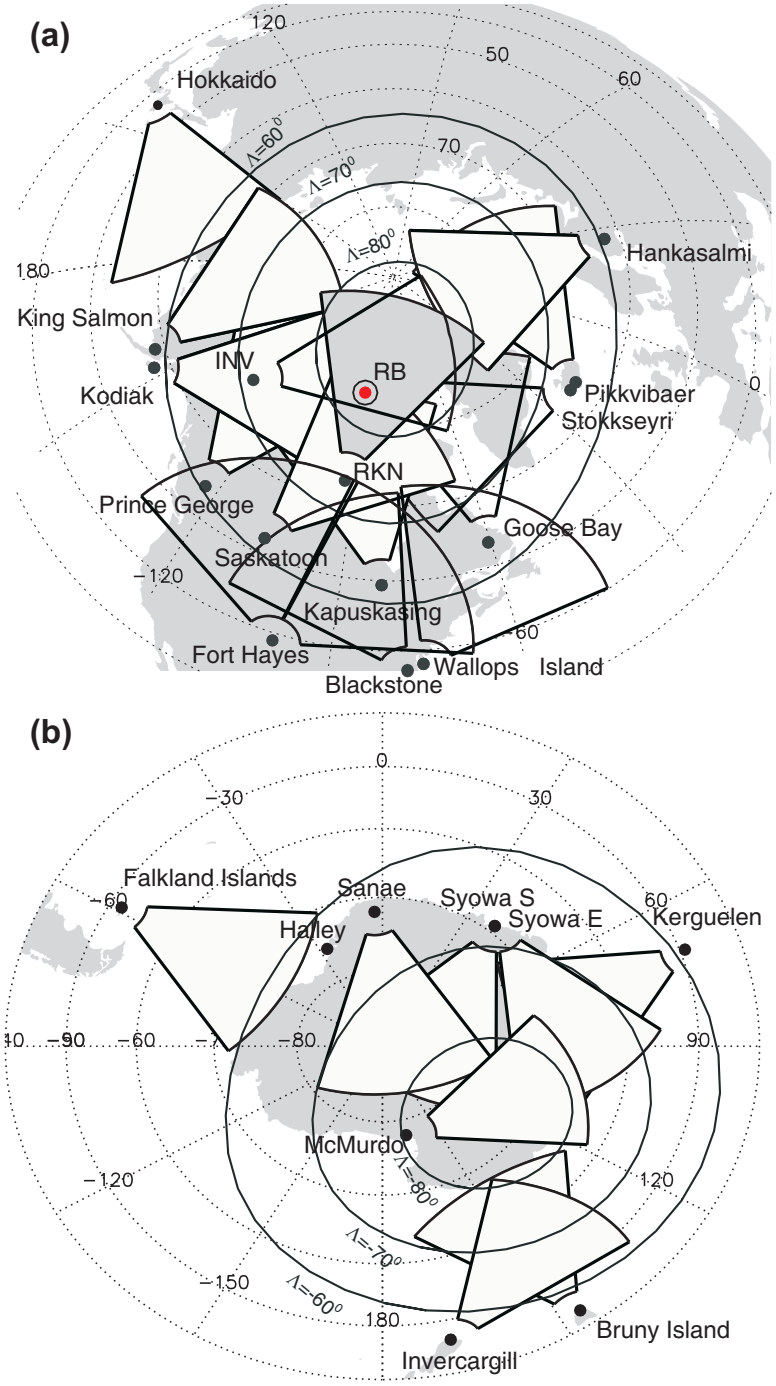

Figure 3.1: Fields-of-view of the currently-operating Super Dual Auroral Radar Network radars in the (a) northern hemisphere and the (b) southern hemisphere.

irregularities are highly-aligned with the geomagnetic field. For the radars to detect echoes from such irregularities, the transmitted radio waves must propagate perpendicular to the wave fronts of the irregularities, and thus be perpendicular to the geomagnetic field. This is achieved by choosing radio wave frequencies such that the ionospheric refraction is significant enough to turn the waves towards normal to the magnetic field. The radars operate at frequencies in the range of 8-20 MHz.

Backscatter occurs when the irregularities are spaced along the path of the transmitted wave such that the scattered signals interfere constructively along the same path, producing an echo that may be strong enough to be detected by the radar. This is known as Bragg scattering. The size of the irregularities to which the SuperDARN radars are sensitive can be determined by the Laue equation:

$$\vec{k}_{irr} = \vec{k}_r - \vec{k}_t. \tag{3.1}$$

Here $\vec{k}_{irr}$ is the wave vector of the irregularity and $\vec{k}_r$ and $\vec{k}_t$ are the wave vectors of the received and transmitted radio waves. Since backscattered radio waves must travel back along the initial path, $\vec{k}_r = -\vec{k}_t$. This with Equation 3.1 means that $\|\vec{k}_{irr}\| = 2\|\vec{k}_t\|$. Relating the wave vectors to wavelengths, via $k = 2\pi/\lambda$, gives $\lambda_{irr} = \lambda_t/2$, i.e. the irregularity size is half the wavelength of the transmitted wave. SuperDARN radars, at frequencies of 8-20 MHz, can receive backscatter from irregularities of sizes 7.5-18.75 m.

In standard operation, each radar transmits a fixed sequence of eight 300 μs wave pulses along one of sixteen beam directions, achieved by using a phasing network to delay the transmission to 16 transmitters. The sequence is repeated $\sim$30 times over $\sim$3 seconds before moving on to the next beam direction, $\sim 3.24^\circ$ away. The 16 beam directions cover an azimuthal range of 52°. A full scan of all 16 beam directions is done in a 1-minute interval. Previously, a seven-pulse sequence was repeated $\sim$60 times over 7 seconds each 2-minute interval.

The 8-pulse sequence used is $\{t_i\} = \{0, 14, 22, 24, 27, 31, 42, 43\}$, where each number is the lag time behind the first pulse, in multiples of 1.5 ms. This gives 28 distinct lag numbers. For example, lag 1 is between the last 2 pulses, while lag 0 is given by the first pulse of the sequence. While lag numbers range from 0 to 43, not all lags between are

available. The first missing lag in this sequence is 6. Missing lags can also occur at various ranges if the returning echo would be received at the same time as another pulse is being transmitted, since the radars cannot transmit and receive simultaneously. For example, range gate 5 is at a distance such that the return signal from pulse 7 arrives just as pulse 8 is transmitted.

Detected echoes are gated into 300 μs bins, which, assuming that the pulse travels at the vacuum speed of light c (3.00×10^8 m/s), correspond to range gates of length 45 km. Velocities are determined for 75 range gates. The first gate is selected to be 180 km and the last gate is then at 3555 km, giving a total coverage of 3375 km.

3.1.1 Determination of Velocity

The Doppler shift of the backscatter is required to find the line-of-sight (l-o-s) velocity of the irregularity. Since the irregularity is moving, the transmitted radio wave, of frequency f_t and assumed speed c, will appear Doppler-shifted in the irregularity's rest frame. The wave backscatters at the shifted frequency relative to the irregularity and is Doppler-shifted again when detected by the radar at frequency f_r. For the limit of v $\ll c$ (v is typically under 1000 m/s), the total Doppler shift is given by

$$f_D = f_r - f_t = 2 f_t \frac{v}{c}. \tag{3.2}$$

Given the Doppler frequency (and using $\omega_D = 2\pi f_D$), the velocity is determined by

$$v = \frac{\omega_D c}{4\pi f_t}. \tag{3.3}$$

The Doppler frequency is determined for each range gate by using an autocorrelation function (ACF) (Fig. 3.2a). The ACF is a function of the lag time between pulses in the pulse sequence, so there are potentially 29 points available, although missing lags can decrease this number. For each lag, the ACF value is given by combining the two signals separated by that lag. The ACF has both a real and imaginary part, coming from the in-phase and quadrature (phase shifted by $\pi/2$) components of each return signal.

The phase of the ACF is determined by comparing the real and imaginary components (Fig. 3.2c), $\Delta\Phi = \arctan(Im/Re)$. The Doppler frequency is determined by the best fit

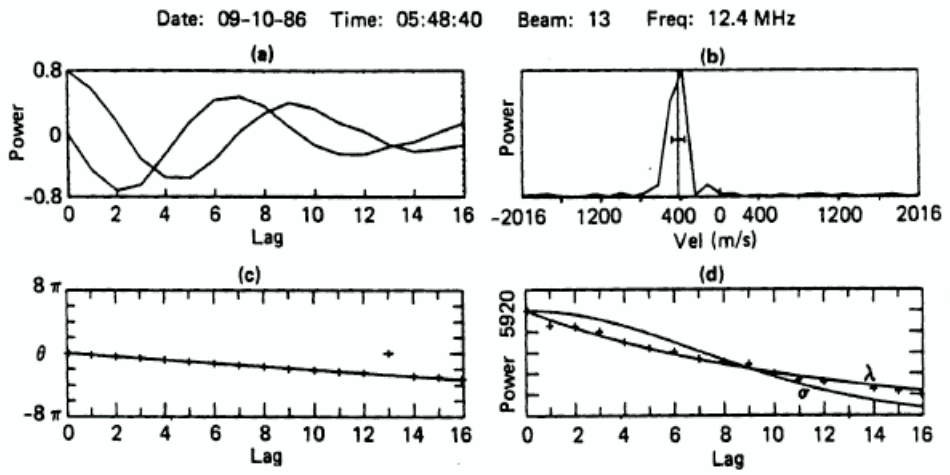

Figure 3.2: An example of the radar signal processing techniques. (a) Real and imaginary parts of the ACF. (b) Doppler spectrum obtained through FFT of the ACF. (c) Phase angle as a function of lag and its linear squares fit. (d) Power variation of the ACF as a function of lag with exponential (λ) and Gaussian (σ) least squares fits. (From *Villain et al.* (1987).)

line to the phase, $\omega_D = \Delta\Phi/\Delta\tau$. Using the Doppler frequency, the Doppler velocity is determined via Equation 3.3.

The power and spectral width of the echo are determined using the amplitude of the ACF. Power as a function of spectral density can be determined from the Fourier transform of the ACF (Fig. 3.2b), but in practice Fourier transforms are not used and the power is determined by the amplitude of lag zero. Figure 3.2d illustrates a procedure to estimate the spectral width of the echoes. It is possible to fit the ACF amplitude with an exponential ($P_\lambda(\tau) = P_0 \exp(-\lambda\tau)$) or Gaussian ($P_\sigma(\tau) = P_0 \exp(-\sigma^2\tau^2)$) function. Each fit gives a spectral width value independent of the other:

$$W_\lambda = \frac{c\lambda}{2\pi f_T}, \tag{3.4a}$$

$$W_\sigma = \frac{c\sigma\sqrt{\ln 2}}{\pi f_T}. \tag{3.4b}$$

For F region echoes, a Gaussian fit is generally used.

3.1.2 Merge Technique

When the SuperDARN radars were first implemented, they were arranged such that pairs of radars would have overlapping fields-of-view. The main purpose of this was to combine

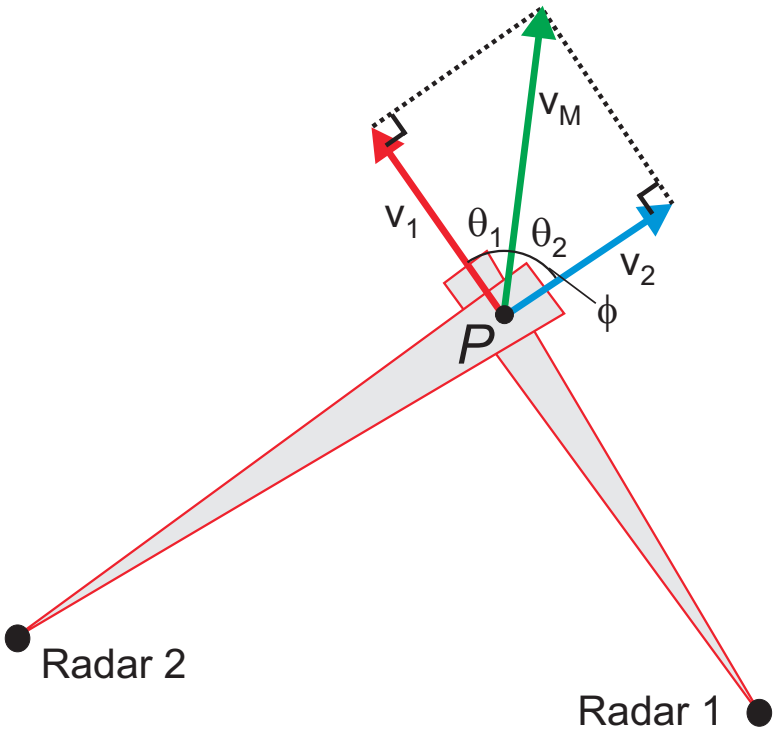

Figure 3.3: The SuperDARN merge technique.

line-of-sight measurements from both radars to get 2-D velocity vectors on a global scale. As shown in Figure 3.3, the l-o-s velocities from each radar beam are cosine components of the full vector:

$$\begin{aligned} v_1 &= v_M \cos(\theta_1) \\ v_2 &= v_M \cos(\theta_2), \end{aligned}$$

where v_M is the merged velocity magnitude, θ_1 and θ_2 are the angles between each radar beam and the merged velocity direction, and v_1 and v_2 are the l-o-s velocities from each radar. To fully determine $\vec{v}_M$ at a given point P, one only needs the magnitude and one of the angles, say θ_1, which will tell us the direction of the $\mathbf{E} \times \mathbf{B}$ drift relative to the radar beam direction. The second angle is still an unknown however, so one more piece of information is required to find the full velocity vector. This last piece is found by noticing that the sum of the 2 angles is equal to the angle between the radar beams, ϕ, which is a fixed value. One can then calculate ϕ by finding the difference in the bearings from point P to each radar site, which is determined using the coordinates of all 3 locations. The coordinates of point P can be determined by its beam/gate location in one of the radars'

FoV. Solving for v_M and θ_1 gives

$$\theta_1 = \arctan\left(\frac{v_2 - v_1\cos(\phi)}{v_1\sin(\phi)}\right), \tag{3.5a}$$

$$v_M = \frac{v_1}{\cos(\theta_1)}. \tag{3.5b}$$

Earlier experiments showed that the number of merged vectors that can be generated is usually not high compared to the amount of l-o-s data available. For this reason, more advanced techniques for making global-scale convection maps have been developed.

3.1.3 FIT Technique

The technique currently employed by the SuperDARN community to generate global convection maps is known as the FIT technique (*Ruohoniemi and Baker*, 1998). The l-o-s velocity data from all available radars are used to generate the convection map, from which the CPCP is determined. Convection maps can be generated for one radar scan (1- or 2-minute intervals) or for multiple scans.

Before calculations are done, the l-o-s velocity data are preprocessed. L-o-s velocities with errors greater than 200 m/s and ground scatter (signals that reflect from the ground after refracting through the ionosphere) are discarded. For each beam/gate cell $(b,g)_i$ at time t_i, a "boxcar" filter is performed using the data in the 3x3 grid centered at $(b,g)_i$ for three consecutive scans, centered at t_i, with a weight applied to the value at $(b,g)_i$. The median value of the dataset is assigned to $(b,g)_i$ if the weighted dataset is sufficiently large, otherwise the cell is not used.

Farther from the radar, the distance between the beams increases, meaning that cells farther away are larger in area than those closer to the radar. To avoid oversampling of data near the radar, the filtered velocities are placed in a grid with cells of similar area. The grid cells are separated by 1° of magnetic latitude ($\sim$111 km) and separated longitudinally such that each cell width is as close to 111 km as possible. For each grid cell, the average of all filtered velocities is assigned to a cell if at least 25% of possible measurements in the cell return values.

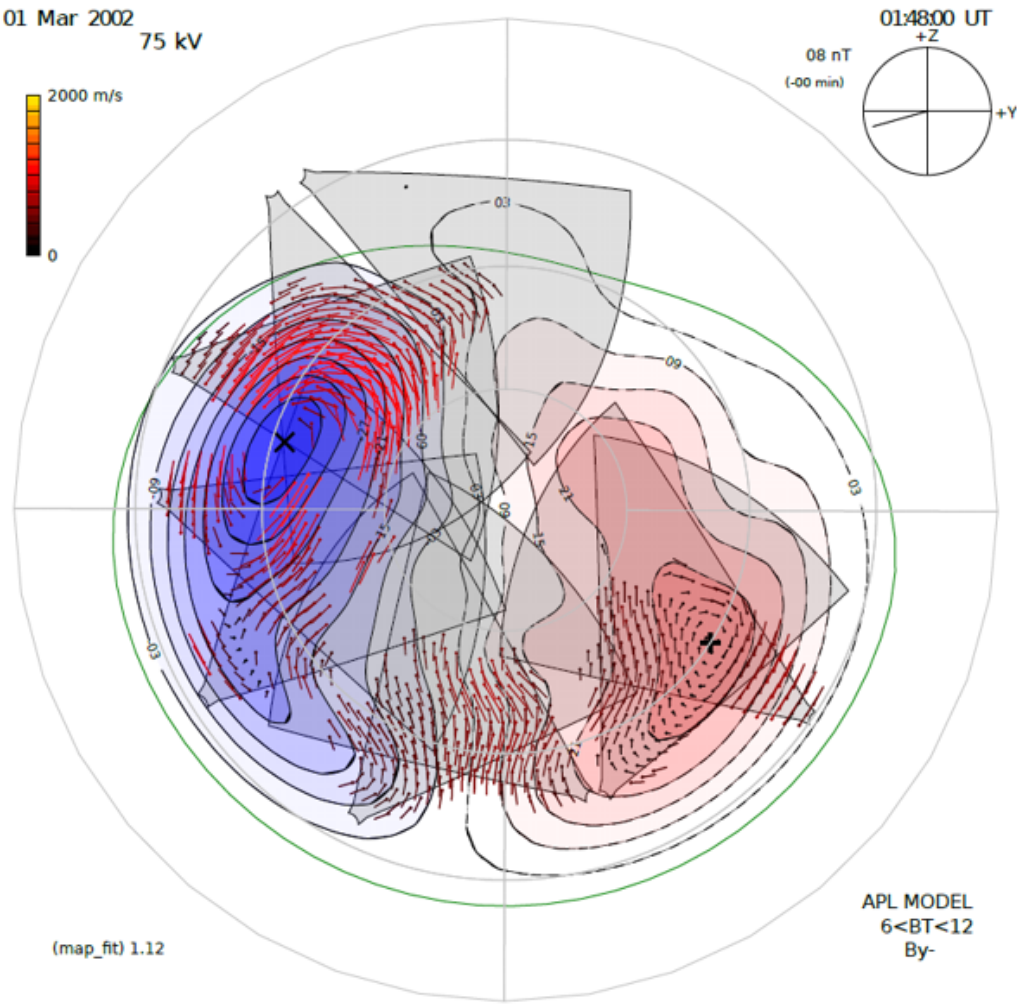

Figure 3.4: Convection and electric potential distribution in the high-latitude ionosphere derived from SuperDARN radar measurements of plasma velocity. The CPCP is the potential difference between the locations labelled $+$ and $\times$.

Two different constraints are placed on the data to prevent the solution from becoming nonphysical. First, as a constraint to areas without data, values from a statistical model are added; there are 24 different statistical models available, covering 8 different IMF clock angle conditions and 3 IMF B_T magnitude ranges (0-4 nT, 4-6 nT and 6-12 nT). The second constraint is the addition of a Heppner-Maynard boundary (HMB) to the edge of the auroral zone to define a lower latitude convection boundary at magnetic latitude Λ_0. The HMB is circular on the nightside, at Λ_0, and contracted poleward on the dayside. Cells between the low-latitude boundary and the HMB are assigned the value 1 m/s to indicate that there should be no convection.

The potential is assumed to be a solution of the spherical Laplace equation at constant radius, where the radius is the Earth's radius plus the height of the scatter region ($\sim$ 300 km). It is related to the velocity through the equations

$$\mathbf{E} = -\nabla\Phi, \mathbf{v} = \frac{\mathbf{E}\times\mathbf{B}}{B^2}. \tag{3.6}$$

The global convection pattern is obtained using a best fit with observed l-o-s velocities v_{los_i}. This is done by minimising the expression

$$\chi^2 = \sum_{i=1}^{N} \frac{1}{\sigma_i^2}\left(\mathbf{v}_i\cdot\hat{\mathbf{k}}_i - v_{los_i}\right)^2, \tag{3.7}$$

where $\mathbf{v}_i$ is the full velocity vector and $\hat{\mathrm{k}}_i$ is the line-of-sight direction of the radar beam associated with the observed l-o-s velocity. The expression is weighted using the velocity error, σ_i. Minimisation of χ^2 is done using singular value decomposition, resulting in the determination of the electric potential everywhere in the polar region.

Figure 3.4 gives an example of the global-scale plasma convection map, produced for 01:48 UT on March 01, 2002. The statistical model used is for $6 < B_T < 12$, B_y- (shown in the bottom right corner). The plot shows convection vectors at each grid point and contours of the electrostatic potential ϕ (3 kV apart). The gradient of ϕ is denoted by the colour of the contours. The Heppner-Maynard boundary is shown by a green line. The IMF orientation (clock angle) and magnitude used for producing the map can be seen in the top right corner of the diagram. The CPCP, here 75 kV, is determined by considering the potential difference between the $+$ and $\times$, indicating the highest and lowest potentials.

One can recognise two cells of plasma flow in Figure 3.4. This is a very typical pattern for a southward IMF ($B_z < 0$).

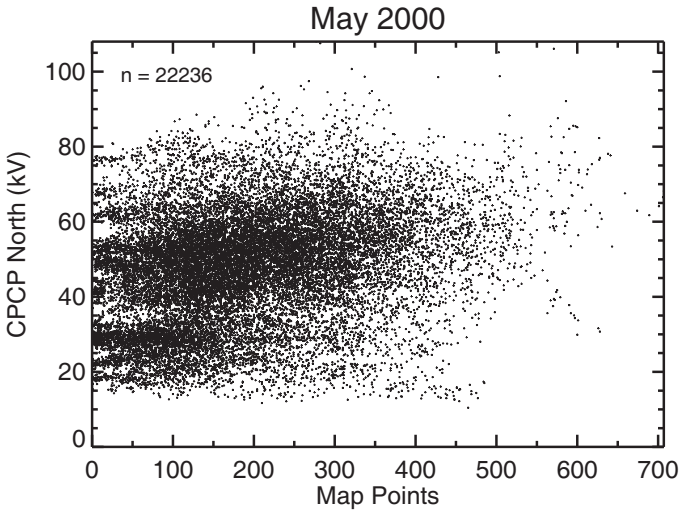

Figure 3.5: Scatterplot of the CPCP versus the number of points per SuperDARN convection map for all available data in May 2000. Total number of available points is shown in the top-left corner.

It has been noted in the past that the SuperDARN global convection maps are sensitive to the statistical model used in the FIT technique (e.g., *Shepherd et al.*, 2002; *Grocott et al.*, 2009), but the extent of this influence on the CPCP has not been shown explicitly. Figure 3.5 shows a scatterplot of the CPCP versus the number of convection map points, N_{map}, for all data in May 2000. For small values of N_{map}, the CPCP tends to cluster around certain values, appearing to be "quantized." The values about which the CPCP clusters are the values that would be obtained by calculating the CPCP only using each statistical model; these values are listed in Table 3.2 (courtesy of R. Fiori). At large N_{map}, the derived CPCP values seem to spread across all potentially possible values, implying that the "quantization" effect is less significant. The minimum threshold for poor coverage seems to be on the order of $N_{map} = 200$.

3.2 Canadian Advanced Digital Ionosonde

CADI is a modern, digital version of the ionosonde. An ionosonde is a type of radar that works on the principle of reflection of radio waves. A radio wave is transmitted into

Table 3.2: The CPCP values derived using only the statistical models employed by the SuperDARN FIT technique.

B_z	B_y	$0 < B_T < 4$	$4 < B_T < 6$	$6 < B_T < 12$
-	-	49	57	65
-		55	67	73
-	+	54	62	78
	-	39	44	53
	+	42	45	47
+	-	27	30	34
+		22	18	16
+	+	29	27	23

the ionosphere vertically and, if a strong enough electron density is present, is reflected and received by the ionosonde. The time Δt between transmitting and receiving a signal determines the distance to the reflector, called the virtual range, $R = c\Delta t/2$. Often the real range is smaller than this due to the group velocity of the radio wave being decreased by the refractive index. Range is equivalent to height if the zenith angle is zero.

Radio waves that propagate through the ionosphere are affected by the charged particles and the geomagnetic field. The index of refraction for an HF radio wave (neglecting collisions) is given by the Appleton-Hartree equation, which, in its most basic form, is

$$n = \sqrt{1 - \frac{f_P^2}{f^2}}, \tag{3.8}$$

where f is the frequency of the radio wave, $f_P = 8.98\sqrt{N_e}$ is the plasma frequency, and N_e is the electron density in m^{-3}. When the radio wave encounters an area with a plasma frequency equal to or larger than the transmitted frequency, the radio wave will undergo total internal reflection. With respect to ionosondes, such areas are referred to as reflectors or sources. The maximum plasma frequency in a layer is called the critical frequency.

Ionosondes transmit a sweep of frequencies, 1 to 20 MHz for CADI. All waves with a frequency above the critical frequency will pass through the layer, while all below will be reflected. The time between transmission and reception of all received signals is translated into virtual height, which are plotted against frequency to create an ionogram. Real height can be obtained by accounting for the index of refraction slowing down the wave speed.

CADI also measures plasma motion by using interferometry. CADI uses four receivers arranged in a square to determine Doppler shift and angle of arrival. For drift measurements, CADI transmits 40 μs pulses with a coded waveform on a fixed frequency. The pulses are coded with a 7-bit Barker code, which are commonly used with pulse radars. The angle of arrival (AOA) of the received echo is determined by the phase difference between the antennae and the Doppler shift is determined by the ACF. The Doppler shift corresponds to velocity via Equation 3.2. The final data product is a 3D velocity vector.

To get a more accurate velocity measurement, multiple pulses, about 60, are transmitted and a velocity vector $\vec{v}$ is fit to the velocities of received echoes from all sources via least squares. The fitting is done by minimising the expression

$$\sum_{s=0}^{n} \left[w_s (d_s - \vec{v} \cdot \vec{k}_s / \pi) \right]^2, \tag{3.9}$$

where s denotes the sources, $\vec{k}_s$ is the wave vector of the echo, w_s is the source weight, based on the echo power. For every 30 s interval, a drift measurement is obtained for 4 frequencies: $\sim$3, $\sim$4, 5, and 6 MHz. Depending on the station, the frequencies can vary; 3.00 MHz is sometimes 2.73 MHz and 4.00 is sometimes 4.20 MHz.

Multiple CADIs are installed across northern Canada as part of the Canadian High Arctic Ionospheric Network (CHAIN) (*Jayachandran et al.*, 2009). Currently, 5 CADIs are operational: Resolute Bay (74.75°N, -95.00°E), Eureka (79.99°N, -85.90°E), Hall Beach (68.78°N, -81.26°E), Pond Inlet (72.69°N, -77.96°E) and Cambridge Bay (74.75°N, -95.00°E).

3.3 OMNI

The solar wind and IMF data used in this thesis were obtained from the High Resolution OMNI dataset (ftp://nssdcftp.gsfc.nasa.gov/spacecraft_data/omni/high_res_omni/). OMNI is a collection of data obtained from 4 satellites (ACE, Wind, Geotail and IMP 8) that contains measurements of various parameters related to the solar wind and the IMF. These parameters include IMF B_x, B_y and B_z; solar wind velocity magnitude and components; proton density and temperature; ram pressure; and the bow shock nose location,

which is determined by ram pressure and B_z.

Since OMNI combines data from multiple spacecrafts at various locations into a single dataset, the data are time-shifted to the bow shock nose. Time-shifting of the IMF is based on the assumptions that the IMF values measured by a spacecraft lie on a planar surface, or "phase front," and the magnetic field values of the phase front are assumed to be unchanging as it propagates with the solar wind, i.e. the IMF flux is frozen-in. The time shift is determined by the solar wind velocity and the distance between the spacecraft and the bow shock nose. The IMF values at the bow shock nose are determined by a minimum variance analysis, known as MVAB-0, of the $\sim$16 sec IMF measurements by the spacecraft in question, as described by *Haaland et al.* (2006), which is a "corrected" version of *Weimer et al.* (2003) (which had the wrong derivation but correct computer code due to a serendipitous error). The plasma data are time-shifted along with the IMF data.

The data used in this thesis are time-shifted an additional 6 minutes to allow for propagation to the front of the ionosphere. 2-minute resolution data were generated by taking averages of every two 1-minute readings.

The OMNI dataset also includes ancillary data from other sources. These include various indices such as the AE-index, SYM/H, and the PCN index.

3.3.1 Solar Wind Parameters

Not all of the parameters presented in the OMNI dataset are direct measurements. Plasma measurements such as density and temperature only reflect the proton population of the solar wind and do not account for alpha particles (He^{2+}) and electrons. Certain assumptions are made to account for this (http://ftpbrowser.gsfc.nasa.gov/bow_derivation.html).

First, the assumption is made that the alpha particle density is a fixed fraction f of the proton density, $N_\alpha = fN_p$; a typical value for f is 0.05, although it will vary. Assuming that the solar wind is neutral, the electron density is $N_e = N_p + 2N_\alpha = N_p(1+2f)$.

The solar wind mass density ρ_{sw} is the sum of the mass densities of the three particle types: $\rho_{sw} = m_pN_p + m_\alpha N_\alpha + m_eN_e$, where m is the mass of the particle denoted by the subscript. The electron mass (9.11×10^{-31} kg) is small compared to the mass of a proton ($m_p = 1.67 \times 10^{-27}$ kg) and an alpha particle, composed of 2 protons and 2 neutrons, is

about the mass of 4 protons. The mass density, with units, then becomes ρ_{sw} (kg/m^3) $\simeq$ $2.00 \times 10^{-27}\, N_p$ (cm^{-3}).

The modified mass density is used in the determination of the Alfvén velocity (Eq. 1.6). Using the appropriate units, the Alfvén velocity is

$$v_A \text{ (km/s)} \simeq 20\, B \text{ (nT)} / \sqrt{N_p \text{ (cm}^{-3})}. \tag{3.10}$$

The Alfvén-Mach number given by the OMNI dataset is then calculated using Equation 1.4.

The ram pressure is the sum of the pressures for each particle type (ignoring electrons due to mass) is $m_p N_p v_p^2 + m_\alpha N_\alpha v_\alpha^2$. Assuming equal velocities for protons and alpha particles, this is $p_{sw} = (1+4f) m_p N_p v_{sw}^2$. With the assumptions listed above, the ram pressure in the OMNI dataset is

$$p_{sw} \text{ (nPa)} \simeq 2.00 \times 10^{-6}\, N_p \text{ (cm}^{-3}) \left[v_{sw} \text{ (km/s)} \right]^2. \tag{3.11}$$

CHAPTER 4

SUPERDARN DATA AND THE $\mathbf{E} \times \mathbf{B}$ DRIFT MEASURED BY THE RESOLUTE BAY CADI

In the near future, several convection-measuring instruments will be monitoring the same area of the ionosphere near Resolute Bay (RB), Canada (geog.: 74.75°N, 95.00°W, geom.: 82.87°N, 32.05°E). Currently operational are the two PolarDARN radars at Rankin Inlet (RKN) and Inuvik (INV), the Saskatoon (SAS), Kodiak (KOD) and Kapuskasing (KAP) SuperDARN radars, the CADI ionosonde at Resolute Bay and the north-facing array of the Resolute Incoherent Scatter Radar (RISR-N). New instruments are a third PolarDARN radar at Clyde River, which is to be installed in 2012, and RISR-C, the south-facing array of RISR, also to be installed in 2012.

Because velocity data from all these instruments will be used for research in space physics, it is highly desirable to establish compatibility between the instruments. This is not a simple task as the instruments work with different spatial and temporal resolutions, and joint operation is not as frequent as one would wish.

Koustov et al. (2009b) made a first step in assessing velocity measurements by the RKN and SAS radars, RB CADI, and ion drift meters onboard Defense Meteorological Satellites Program (DMSP) spacecrafts. The comparisons were limited as not much data were available at the time of the work. It was shown that generally RKN-measured velocities are comparable to those obtained by the other instruments. A general tendency was for the RKN velocity to be somewhat smaller then expected from observations of the other instruments, especially the DMSP satellites.

Since 2007, with installation of the INV radar and inclusion of the RB CADI into the Canadian High Arctic Ionospheric Network (CHAIN) network, a significant amount of

plasma velocity data has been accumulated for the PolarDARN radars and RB CADI. This provides an opportunity for a more comprehensive comparison of the data. An attempt for a more comprehensive study has been undertaken recently by *Mori et al.* (2011). Unfortunately, it has been realised recently that the PolarDARN radars have been operating with too narrow a receiver bandwidth, so that the actual resolution of the measurements was not the nominal value of 45 km. The Polar-DARN radars' bandwidth was adjusted in late October 2010. The new data collected since that time are of the best quality available to date and can be compared with RB CADI data.

In this chapter, the initial work by *Mori et al.* (2011) is extended and the dataset gathered between November 2010 and March 2011 is the main focus.

4.1 Geometry of Observations and Approach to the Analysis

Figures 4.1a,b show the FoV of the RKN and INV PolarDARN radars and the location of the RB CADI. The intersection between the beams closest to the RB zenith is made by RKN beam 5, gate 27 and INV beam 13, gate 30. For this reason, these radar cells were selected for the comparison.

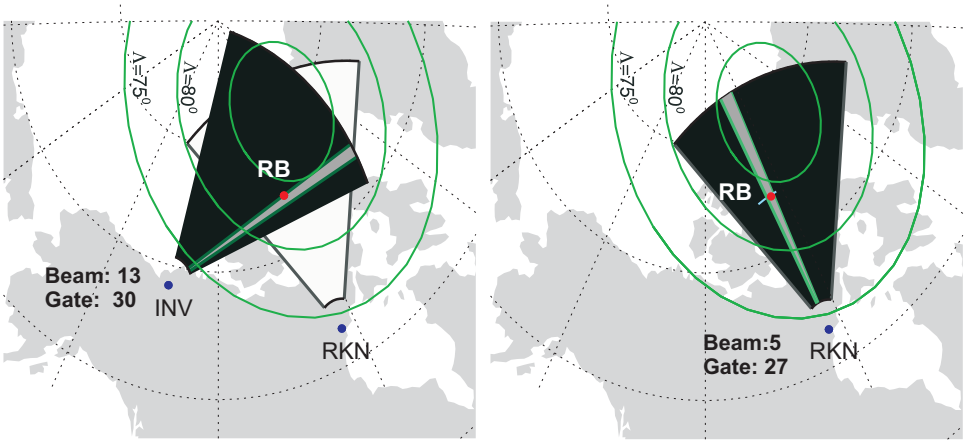

Figure 4.1: Fields-of-view (FoVs) of the PolarDARN radars at (a) Inuvik and (b) Rankin Inlet. Considered beams are shown by grey sectors within the respective radar FoVs. RB location is shown by a red dot.

Assessment of the PolarDARN-RB CADI velocities can be done in a number of ways.

The CADI instrument provides a 2-D vector of plasma flow roughly in the zenith of RB. Each PolarDARN radar measures only the component of the $\mathbf{E} \times \mathbf{B}$ flow along the individual beam positions. Therefore, it is natural to compare the measured PolarDARN radar l-o-s velocity with the projection of the CADI $\mathbf{E} \times \mathbf{B}$ velocity vector onto the respective beam (Fig. 4.2a). This has been a popular way of assessing the velocity data in the past (e.g., *Xu et al.*, 2001; *Drayton et al.*, 2005). For the experimental configuration at hand, since the point of the INV-RKN radar beam intersection is not far from the RB zenith, it is possible to merge PolarDARN l-o-s velocities and obtain a full vector of the $\mathbf{E} \times \mathbf{B}$ drift. In this case, a 2-D comparison of a RKN-INV merged velocity vector with a CADI vector is possible (Fig. 4.2b).

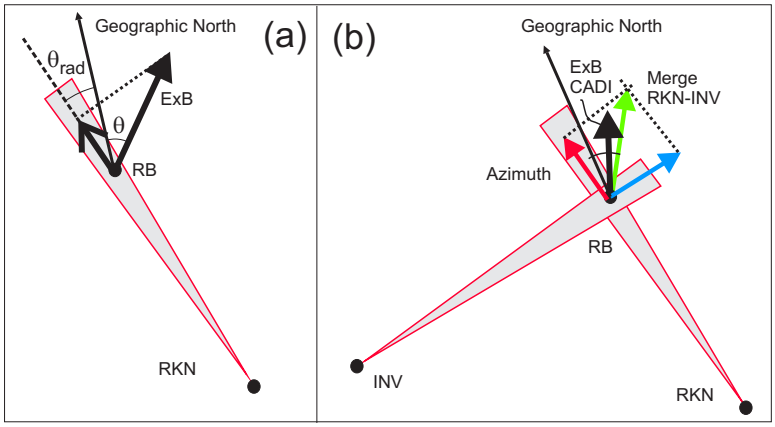

Figure 4.2: A sketch illustrating (a) projection and (b) full vector comparisons of the PolarDARN HF velocities and RB CADI velocity.

The CADI projection velocities were determined by $v_{proj} = -v_H \cos(\theta - \theta_{rad})$, where v_H is the horizontal velocity magnitude measured by CADI, θ is the azimuth and θ_{rad} is the angle between azimuth 0 and the PolarDARN radar beam onto which the velocity is being projected. For RKN beam 5, $\theta_{rad} = -4.17^\circ$ and for INV beam 13, $\theta_{rad} = 83.76^\circ$. The negative sign is included in the expression for the projected velocity because a positive projected velocity corresponds to irregularities moving away from the radar, which PolarDARN measures as a negative Doppler shift.

Since the projected velocity is a function of two different CADI parameters (magnitude

and direction), it was necessary to consider error propagation:

$$\frac{\delta v_{proj}}{v_{proj}} = \sqrt{[\delta\theta \tan(\theta - \theta_{rad})]^2 + \left(\frac{\delta v_H}{v_H}\right)^2}. \tag{4.1}$$

Error in a parameter is denoted here by δ. Notice that for azimuths that are nearly perpendicular to the radar beam, the *tan* function will cause the relative error to be very large. It was decided to remove these points from the analysis because they can cause disagreement in the l-o-s polarity (positive or negative along the beam). The actual $\mathbf{E} \times \mathbf{B}$ direction should be within the range $[\theta - \delta\theta, \theta + \delta\theta]$, but if the angle perpendicular to the beam is within that range, then it is possible for the azimuthal error to cause the CADI projected velocity to have the wrong polarity. These points, and others with high error, were filtered out by selecting $\delta v_{proj}/v_{proj} < 0.3$. It should be noted that errors in radar l-o-s velocities were not available.

The PolarDARN merged velocities and azimuths were determined using Equations 3.5a,b assuming RKN for radar 1 and INV for radar 2. The azimuthal angle given by Equation 3.5b is measured from the radar 1 beam direction, which was RKN beam 5 in this case. In order to match this with CADI azimuth data, which is measured from the direction of geographic north, a shift of -4.17° was required, the angle between beam 5 and geographic north over RB. To increase statistics for the merged analysis, the median velocity was taken from three gates, centered over RB, instead of using the velocity from one gate.

The CADI ionosonde makes measurements at several frequencies, 2.73, 4.00, 5.00 and 6.00 MHz, so that a velocity report is available for every 30 seconds at each frequency. A limited analysis showed that the CADI data obtained at various frequencies are generally consistent, although data obtained using the lowest transmitter frequency are noisier while the data at the largest frequencies are very infrequent. The decision was made to use 4 MHz data. At this frequency the data are still somewhat noisy. One of the reasons for this is a lack of a sufficient number of sources involved in the velocity derivation (see Chapter 3). To alleviate the problem, and to remedy the difference in temporal resolution between CADI and PolarDARN measurements, the CADI data were averaged over multiple scans. For each available 1-minute PolarDARN measurement, three consecutive CADI

measurements centered around the PolarDARN measurement are averaged, weighted by error. CADI velocities that were determined using less than 20 reflectors (via Eq. 3.9) were not considered.

It should be noted that although 5 months were considered, data were not continuously available for the entire period. Data from the Inuvik radar were only available for a few days in November 2010 and RB CADI data were only available for 9 days in January 2011.

Lastly, a point should be made about how the linear regression is performed when comparing instruments. Ordinary least squares fitting minimises the sum of the square of the vertical distances between the data and the best fit line. This assumes that uncertainty exists in only one variable. In this case, two instruments with uncertainty are compared. This requires an unbiased approach that accounts for this. In this Thesis, least squares fitting was performed using perpendicular offsets, minimising the square of the perpendicular distances between the data and the best fit line. The best fit line for datasets $\{x_i\}$ and $\{y_i\}$, of form $y = mx + b$, is then given by

$$m = -B + sgn(r)\sqrt{B^2 + 1}, \tag{4.2}$$

$$b = < y > - m < x >, \tag{4.3}$$

$$B = -\frac{\sigma_y^2 - \sigma_x^2}{2Cov(x,y)}, \tag{4.4}$$

where angle brackets denote the mean, r is the correlation coefficient, Cov is the covariance, σ^2 denotes the variance and sgn is the signum function.

4.2 Joint RKN-RB CADI Observations on December 24, 2010

Although both the PolarDARN radars and RB CADI work continuously, not many joint measurements can be found. One factor is that RKN echo occurrence over RB is not frequent (*Liu*, 2010). If RKN echo detection rates at ranges ∼900 km can be as large as 30% of the observational time, it is only ∼3% at ranges of ∼1350 km for the RB zenith (*Ghezelbash et al.*, 2011). There is also a seasonal variation in the echo detection rate.

Fewer echoes occur in the summer than in the winter. This is thought to be caused by the variations in the solar illumination of the high-latitude ionosphere (e.g., *Koustov et al.*, 2004).

Another factor is the inherent property of the radars to measure velocity along its beam in a specific direction. If the radar beam direction is nearly perpendicular to the plasma flow, it will measure a very small velocity. These small velocities were typically not used in this study due to possible ground scatter contamination at low velocities; PolarDARN velocities with magnitudes under 100 m/s were not included. In order to keep the statistics balanced, CADI projected velocities under 100 m/s were also removed, although many of these points were filtered due to high relative error from the azimuth being near perpendicular to the beam direction.

CADI can also be subject to limitations on detection rate. CADI relies on radio wave reflection, which requires that the transmitted frequency is less than the largest plasma frequency in the ionosphere; typically this is the critical frequency of the F2 layer, f_0F2. If the electron density is too low, then the transmitted wave will not be reflected, but will pass through the ionosphere. Often there are fewer CADI measurements when the polar cap is dark than when it is sunlit and photoionisation occurs. Thus more CADI data are available in the summer than in the winter, opposite that of variations in PolarDARN echo detection rates. Despite this trend, CADI data are still available in the winter, with the highest occurrence around local noon, $\sim$18 UT for RB, and the lowest occurrence in the post-midnight sector, $\sim$6-12 UT.

Figure 4.3 gives an example of joint PolarDARN-RB CADI data on December 24, 2010. The top two panels, Figs. 4.3a,b, show the $\mathbf{E} \times \mathbf{B}$ magnitude and azimuth, counted clockwise from the direction of geographic north, as measured by the RB CADI. The top panel also gives the number of individual scatterers/reflectors involved in the velocity determination. One can see that the number of measurements is larger at later times, corresponding to closer to local noon, where the ionosphere is expected to be denser. Figure 4.3c gives the projection of the $\mathbf{E} \times \mathbf{B}$ velocity vector onto RKN beam 5, the closest beam to the RB zenith. Negative velocities here correspond to irregularity motion away from the radar, matching the convention used by PolarDARN. Figure 4.3d presents the

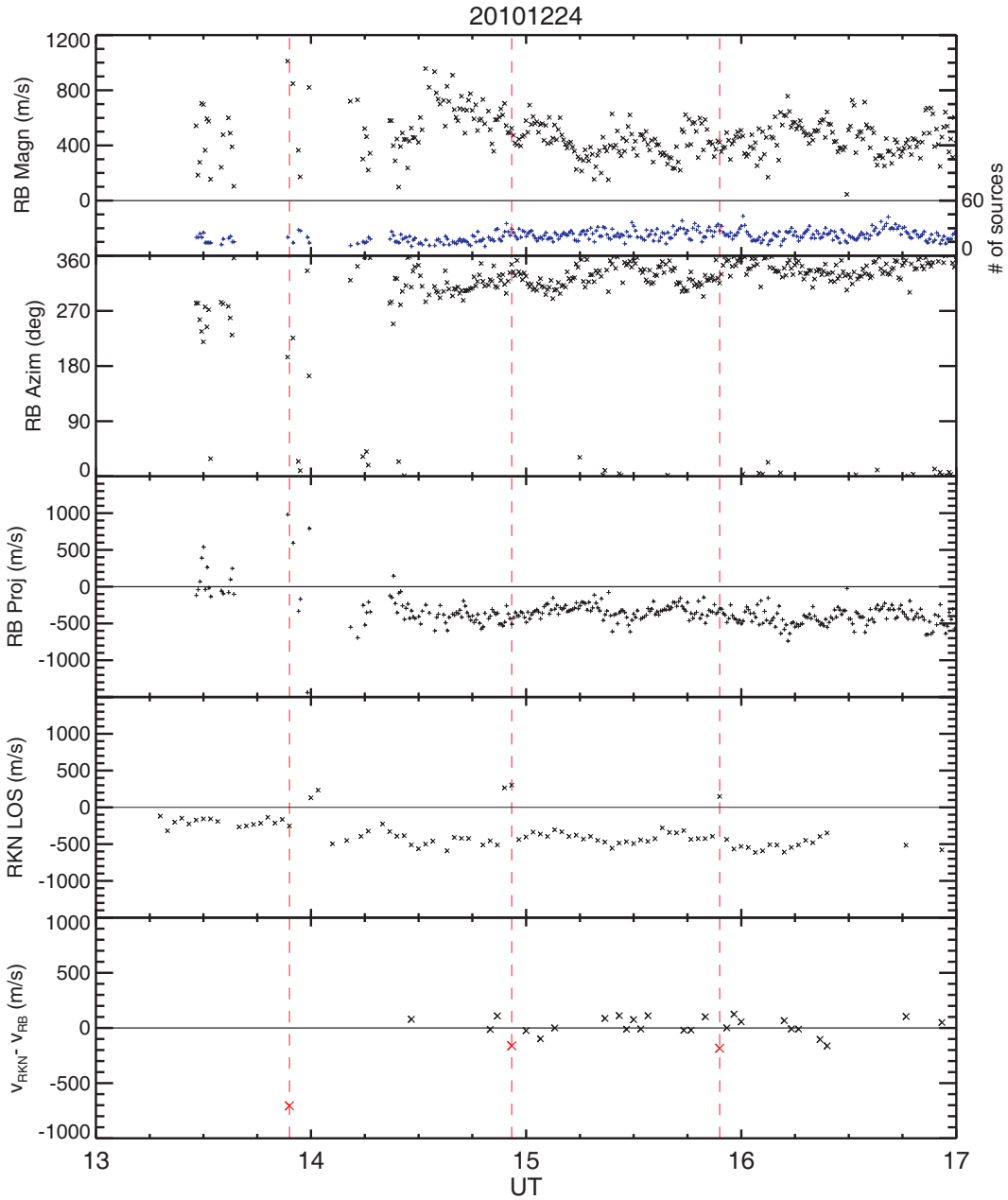

Figure 4.3: Temporal variations of (a) the $\mathbf{E} \times \mathbf{B}$ magnitude and (b) direction (counted clockwise from geographic north) as measured by the RB CADI, (c) CADI $\mathbf{E} \times \mathbf{B}$ projection on the RKN beam 5 (range gate 27), (d) RKN l-o-s velocity and (e) the difference between the CADI expected and RKN-observed l-o-s velocity along beam 5 over RB.

RKN l-o-s velocity while Figure 4.3e shows the difference between the CADI velocity projections and the radar l-o-s measurements. The vertical red dashed lines show points where CADI projected velocity and RKN l-o-s are of opposite polarity.

One can see that the $\mathbf{E} \times \mathbf{B}$ magnitude varied between 200 and 800 m/s and the general direction of the l-o-s was antisunward, something that one would expect for the two-cell convection pattern in the pre-noon sector. The expected l-o-s velocity along RKN beam 5 from CADI measurements was between 100 and 500 m/s. This velocity was generally consistent with RKN velocities; the typical differences were on the order of 100 m/s. There were several instances when the velocities had opposite polarity and differed significantly, by more than 200 m/s. Three of these, well seen in Figure 4.3e, are marked by red crosses and vertical dashed lines. These will be discussed later.

Comparison of Figure 4.3a and 4.3e gives a good sense as to how difficult it is to identify joint radar-CADI data; despite numerous points for CADI, not many of these meet the criteria for good data (20 reflectors, 0.3 relative error for projected velocity), and not all of these would have concurrent RKN observations.

4.3 Statistics for 1-D (Projection) Comparison

Figure 4.4 presents data of joint PolarDARN-CADI velocity measurements. Scatterplots of Figs. 4.4a,b indicate that points can be in any quadrant of the comparison plane, but the majority of them are located in the expected quadrants so that the velocity polarities are the same. For a fraction of total points, 5-10%, the radar velocity has different polarity as compared to the RB CADI projection velocity, called here "bad" points. The reasons for such a drastic disagreement will be discussed later. For points in quadrants 1 and 3, red is used to denote where the difference in velocity is less than a factor of 2. These are considered to be points of "good" agreement. The fraction of good points was typically $\sim$85% of all available points. It should be noted that the definitions of "bad" and "good" here do not add up to all the points but leave out points that agree on direction but not magnitude. The slopes of the best fit lines of the good points (blue) in Figures 4.4a,b are 0.93 (INV) and 0.97 (RKN), implying that PolarDARN velocities may be slightly

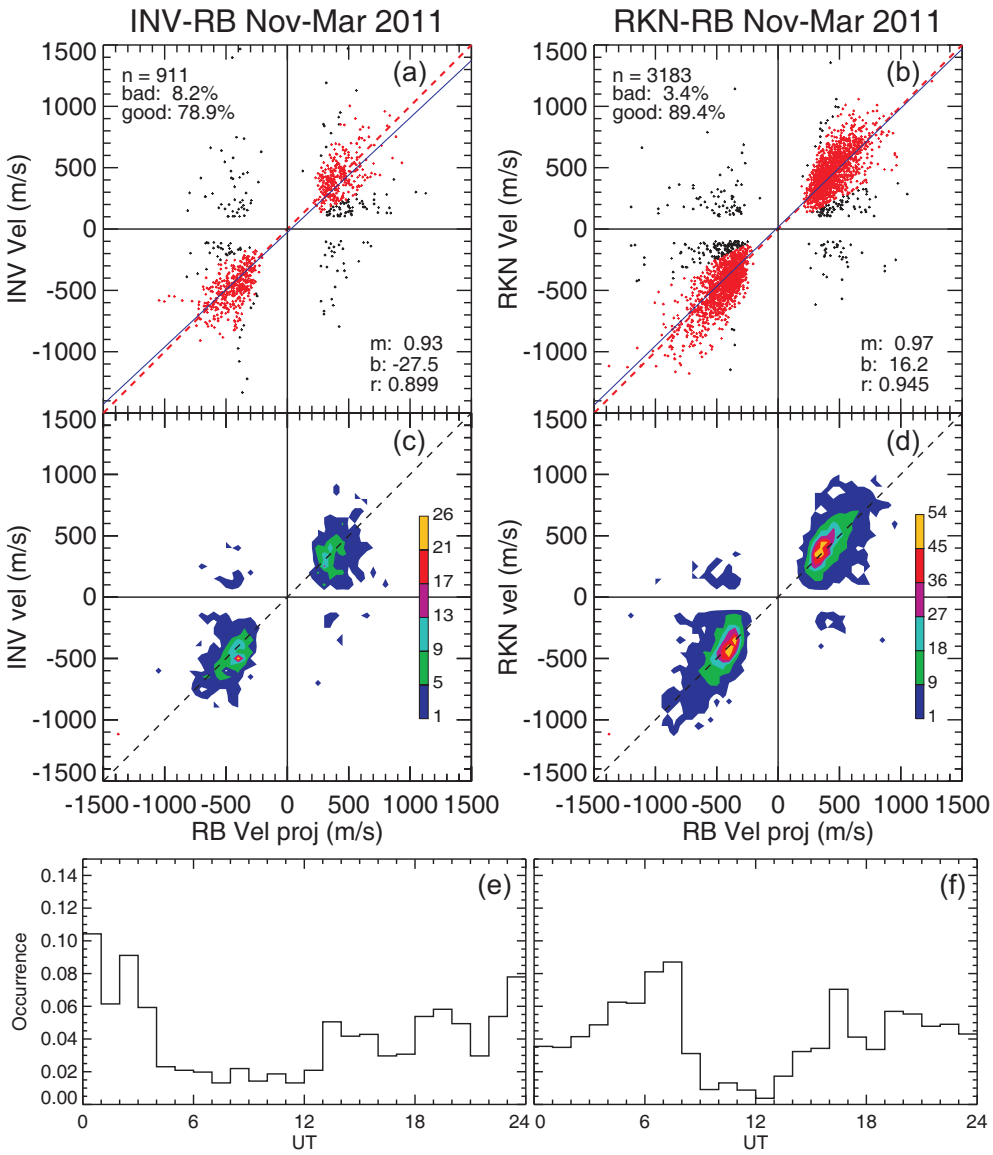

Figure 4.4: Scatterplots of the l-o-s velocity from (a) INV beam 13, gate 30 and (b) RKN beam 5 gate 27 versus RB CADI velocity projected onto the respective beams. "Good" points (red) are where the PolarDARN-CADI velocities differ by at most a factor of 2. Total number of points n, the percentage of good points, and the percentage with opposite polarity (bad) are shown in the upper left corner. The slope m and y-intercept b from linear regression and the correlation coefficient r of non-bad points are shown in the right bottom corner. The blue line shows the linear fit. (c) and (d) are contour plots of the occurrence of the data from (a) and (b). Occurrence of points vs UT for the (e) INV- and (f) RKN-RB CADI comparisons.

smaller in magnitude than expected from concurrent CADI measurements. Figures 4.4c,d show that the majority of the points considered are located near the bisector of perfect agreement.

The above comparisons have been made for mostly echoes during the daytime and pre-midnight, as can be seen in Figs. 4.4e,f; not too many concurrent data points were available in the post-midnight sector, between 05 and 11 UT. This is to be expected from the scattering/reflecting conditions for PolarDARN/CADI.

4.4 Statistics for 2-D (Vector) Comparison

Figure 4.5 compares merged PolarDARN velocities and RB CADI full vectors by considering magnitude and direction separately. For both plots, there is a significant spread of points. For the magnitudes, Figure 4.5a, there appears to be good agreement with the majority of points. The linear fit line is off this trend and suggests much larger PolarDARN velocities. This is thought to be caused by the relatively low correlation coefficient and the spread of the data points away from the bisector. The azimuths, Figure 4.5b, appear to agree very well. About 76% of points have azimuthal difference of less than 30°. The same magnitude and azimuth data are presented in 4.5c,d in the form of contour plots for occurrence of magnitude and azimuth. These indicate that indeed the majority of points do agree very well.

One tendency seems to be clear in Figures 4.5a,c: the merged PolarDARN velocity is larger on average than the $\mathbf{E} \times \mathbf{B}$ magnitude reported by the RB CADI. The tendency covers a range of velocities between 200-700 m/s. Another indication of the trend is that the slope of the best fit line is greater than unity.

4.5 Discussion

Both performed comparisons showed reasonable overall agreement of PolarDARN and CADI velocities. The joint dataset covered a significant range of $\mathbf{E} \times \mathbf{B}$ magnitudes, from $\sim$100 to 800 m/s for both CADI and PolarDARN. It should be noted that the low velocity

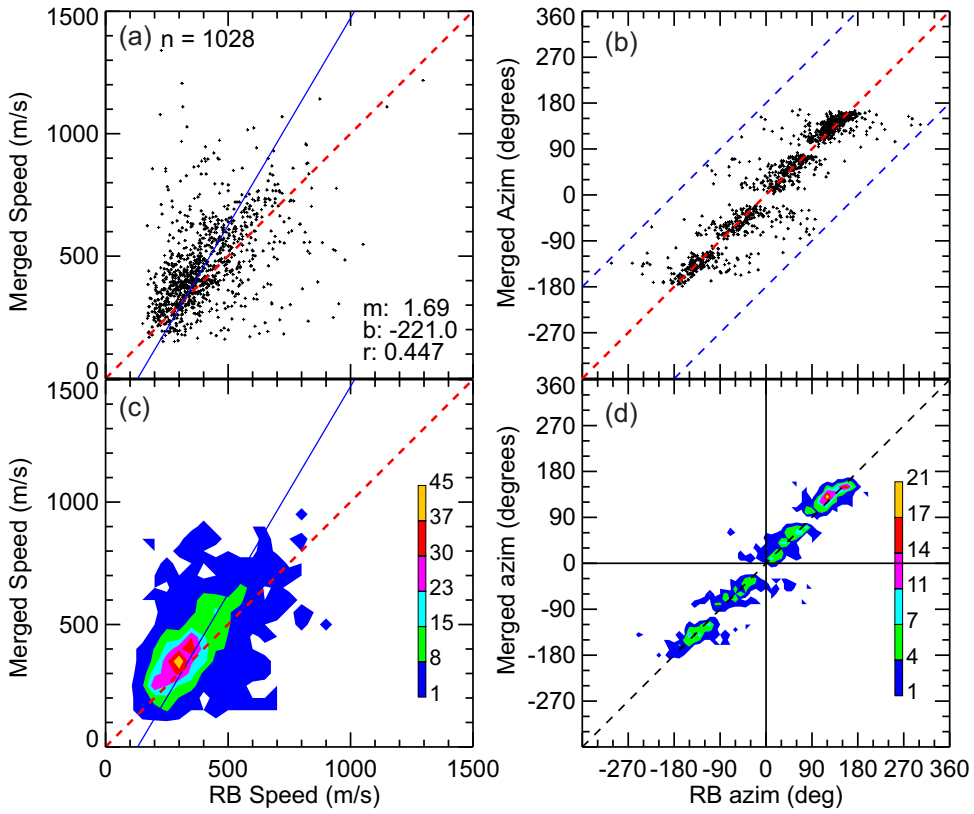

Figure 4.5: Scatterplots and contour plots comparing PolarDARN and RB CADI velocity magnitudes and directions from November 2010 to March 2011. The blue line is a linear fit to all points and the slope and the y-intercept of the line are indicated on the right side with the correlation coefficient *r*. Total number of points is n=1028.

data were completely excluded from the analysis; this happened naturally for CADI upon application of imposed requirement of having low projected velocity error for measurements with CADI. This limitation leaves room for future investigation of the low-velocity data. To accomplish this task, a careful analysis of the PolarDARN data quality is required as strong ground scatter contamination can be a serious factor influencing the radar velocities.

In this study, high-velocity data have not been achieved, as well. This is unfortunate, as large velocities of more than 1000 m/s are of special interest; in this range, the HF velocity has been shown to become significantly smaller than the $\mathbf{E} \times \mathbf{B}$ drift (*Xu et al.*, 2001; *Drayton et al.*, 2005; *Xu et al.*, 2008). In terms of magnetic local time, the data were

less present for the midnight sector (Figs. 4.4e,f). As explained, this is expected for winter conditions and further data accumulation, especially for equinoxes, is needed to improve data coverage. It should be noted that CADI data alone do show periods with very large velocities up to 2 km/s. Similarly, some PolarDARN velocities are significantly above 1000 m/s. The high velocities for both instruments are not observed simultaneously, for reasons that need to be further investigated.

The 1-D analysis showed better agreement for the RKN radar as compared to the INV radar (3.4% of bad points as compared to 8.2%; slope 0.93 versus 0.97). Reasons for the difference are not clear. A significant difference in the number of points available can be seen. This is an interesting fact by itself; the distance for the INV radar is only 3 gates farther than for the RKN radar, yet the number of joint points with CADI dropped by about a factor of 3. Perhaps a smaller database for the INV radar is an issue here and with further data accumulation, the differences between the INV and RKN radars would vanish.

The 1-D analysis revealed a number of points for which the CADI and PolarDARN velocity polarities were opposite. The magnitudes of the velocities involved were not necessarily small, which would be expected for periods when the radar beams are near-perpendicular to the plasma flow and can be sensitive to small fluctuations. Very typical $\mathbf{E} \times \mathbf{B}$ drifts for the polar cap are $\sim$300 m/s (*Mori et al.*, 2011) and the velocities of points with different polarities is $\sim$200 m/s (Figures 4.4a,b).

There are probably several reasons for such drastic differences. One might think that such points correspond to periods when a patch of plasma with a completely different E-field entered the radar FoV or was generated for a short period of time. One then would not expect agreement as CADI measurements would correspond to a somewhat different volume of the high-latitude ionosphere. There is a possibility that for some periods, due to strong lateral refraction, the systems monitor completely different spots of the high-latitude ionosphere. Time difference might be a factor as well. Initial attempts to locate a preferential time of day, corresponding to photoionisation in the ionosphere, for points of polarity disagreement were unsuccessful.

An analysis reported by *Mori et al.* (2011) considered nearly co-located INV and Kodiak (KOD) radar measurements along approximately parallel beams, as INV beam 14

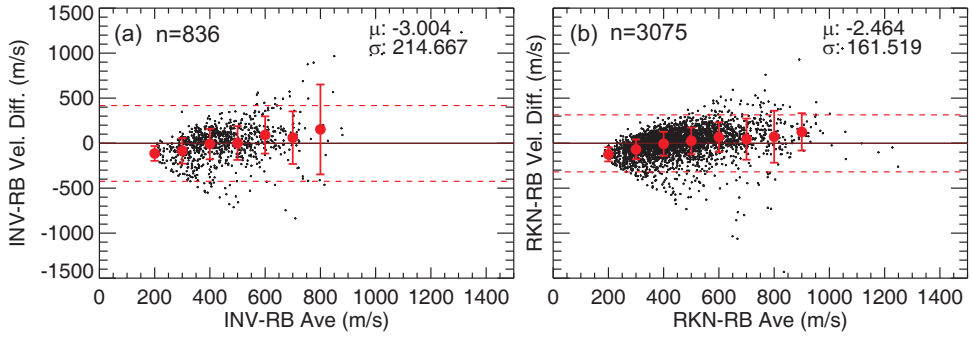

Figure 4.6: Scatterplots of the difference versus the average of each pair of (a) INV/(b) RKN l-o-s and RB CADI projected velocities from quadrants 1 and 3 of Figures 4.4a,b. The mean (μ) and standard deviation (σ) of the velocity differences are shown in the top right corner. The black solid line denotes perfect agreement and the dashed red lines are 2 standard deviations from the mean. Red dots mark average values over 100 m/s bins, with error bars denoting the standard deviation of each bin.

and KOD beam 7 nearly coincide. It was found that in about 15% of cases, the polarity of the measured velocities did not coincide. It may be that in these cases also the echoes were coming from different regions of the ionosphere.

Another reason could be that unflagged ground scatter is present in the radar data. Ground scatter contamination is notoriously difficult to detect (*Ponomarenko et al.*, 2008).

Another way of assessing the velocity differences was performed in Figure 4.6. Here, for every pair of PolarDARN-CADI measurements with agreement in polarity (quadrants I and III), the difference between the magnitudes is plotted against their average. The difference is taken such that it is positive for a larger PolarDARN velocity and negative for a larger CADI velocity. The mean difference is near zero, which would suggest a very good agreement between instruments. On closer inspection, however, it appears that the binned averages increase with velocity. It is expected that CADI is higher on average for lower velocities as Figures 4.4a,b show many black points where radar velocities are low. What is unexpected is that the PolarDARN radars, on average, report larger velocities than CADI for velocities over $\sim$500 m/s. A similar analysis for the merged radar velocities showed that the merged velocities were on average about 60 m/s larger than the CADI velocity magnitudes (Fig. 4.5). This is contrary to previous studies comparing PolarDARN velocities with other convection measuring instruments (*Xu et al.*, 2001; *Drayton et al.*, 2005; *Xu et al.*, 2008; *Koustov et al.*, 2009b), which showed that HF radars such as Super-

DARN/PolarDARN underestimate velocities when compared with other instruments such as incoherent scatter radars and ion drift meters on DMSP satellites. The above results imply that the RB CADI instrument perhaps underestimates the true $\mathbf{E} \times \mathbf{B}$ magnitude as well. *Koustov et al.* (2007) showed this by comparing RB CADI data with DMSP ion drift data, but to what extent CADI underestimates when compared to coherent radars, such as RKN and INV PolarDARN radars, was not well established. The data presented here hint that CADI underestimates the velocity slightly more than SuperDARN. This raises questions about the CADI method of the velocity determination.

Over recent years, the reason for the HF radar velocity underestimation has been thought to be due to the exclusion of the index of refraction in the velocity determination (*Gilles et al.*, 2009). Theoretically, CADI measurements should not be affected by the index of refraction in the ionosphere. No explanation can yet be offered for why CADI velocities are statistically smaller than PolarDARN velocities, but one possible explanation for velocity discrepancies during certain times is that some of the CADI individual reflectors are in reality coherent scatterers and not clouds of strong electron density.

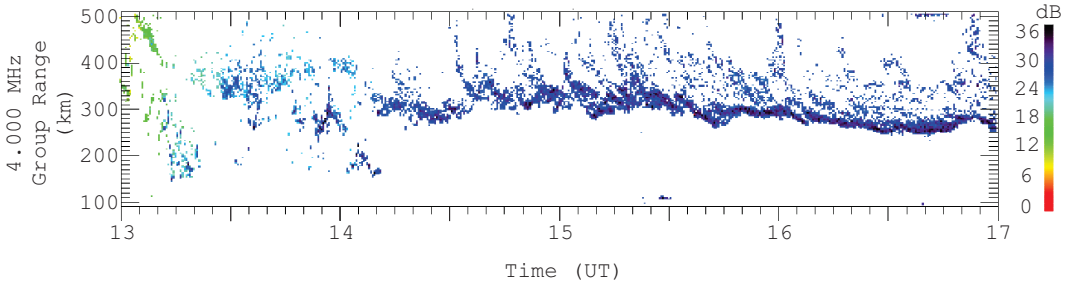

Figure 4.7: CADI 4 MHz virtual height of all sources for 13-17 UT on Dec 24, 2010. The colour scale on the right denotes the power of the signals.

During times of very low electron density, such as near midnight local time during winter, the plasma frequency can drop below 4 MHz, the CADI transmission frequency used in this study. Under these conditions, it is possible that the signals received by CADI are not reflections but coherent scatter, which would be received over a wider range of heights than reflections and have a lower power. In Figure 4.7 an example is given of CADI observations where from 15 to 17 UT the reflections are clustered near a well defined height in the ionosphere and have a high power (> 30 dB). Between 13 and 14 UT,

however, the power is much lower and the heights are widespread. This is only a possibility, however, and weak reflections off small dense patches cannot be rules out. It should be noted though that this is the same timespan that the first polarity discrepancy occurred in Figure 4.3.

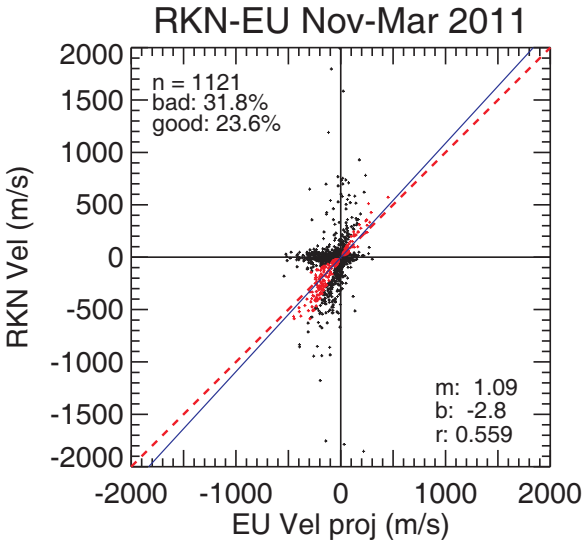

Figure 4.8: Scatterplot of LOS velocity from RKN Beam 7 Gate 40 vs. EU CADI projected velocity for Nov 2010-Mar 2011.

Although a reasonable agreement between RKN radar and RB CADI data is reported here, similar comparisons with other CHAIN ionosondes did not give similar results. In Figure 4.8, RKN data and EU data were compared for the same period of November 2011-March 2011. Here one can see there are a number of points that agree well, but significant amount of points strongly disagree. One obvious effect is detection of very large RKN velocities simultaneously with very small EU velocities. Reasons for such disagreements are not known. In future, data from both instruments will undergo scrutiny to reveal any deficiency of the measurements. This task is beyond the scope of this thesis.

4.6 SuperDARN CPCP and CADI

With reasonable agreement between CADI and PolarDARN velocities, how SuperDARN CPCP compares with CADI velocity can now be tested. Plasma velocities at very high latitudes, i.e. near the center of the polar cap, are expected to be somewhat uniform,

so RB CADI velocities can be taken as an average polar cap velocity. The strength of the ionospheric electric field is proportional to the polar cap velocity, so it is expected that CPCP will also be proportional to the polar cap velocity. Assuming the ionospheric electric field is constant, the relationship between the CPCP and electric field is $\Phi_{pc} = E\,L$, where L is the distance between the locations of the maximum and minimum potentials used to calculate the CPCP. The distance measurements were not available, so another method was required to limit the effect of this parameter.

The max-min points sit at, or very near, the edge of the polar cap, which expands to lower latitudes at times of large magnetic disturbances. To keep the size of the polar cap from varying, the dataset was selected for times when only small fluctuations in the geomagnetic field occur, Sym-H > -30 nT. Data were also selected for negative IMF B_z values, to ensure that the two-cell convection pattern, upon which these assumptions are made, was present.

If SuperDARN CPCP underestimation is only due to the velocity underestimation effect, then a linear trend is expected. A nonlinear trend (i.e. saturation) would then suggest another issue with SuperDARN CPCP. Saturation here should not be confused with the saturation effect between the solar wind/IMF and CPCP as this is a comparison between 2 parameters reflecting ionospheric convection.

Data from the years 2000-2002 were considered in the comparison, when more data were available from SuperDARN. Considering 3 years also allows for better statistics, because during this period, data from the RB CADI contains many gaps. The SuperDARN data were selected for periods for which the CPCP was based on convection maps containing more than 300 vectors, as discussed in Chapter 3. The CADI data were selected under the condition that the velocities were determined with at least 20 reflectors (Eq. 3.9). Additionally, CADI velocities were limited to those with errors less than 150 m/s.

Figure 4.9 shows a contour plot of SuperDARN CPCP plotted versus CADI velocity. Average values for 100 m/s bins are shown by black dots and the vertical bars reflect the standard deviation of the values in each bin. The binned values appear to increase linearly, although the spread in the CPCP data for each bin is quite large, $\sim$40 kV for the denser areas (excluding the blue). Nevertheless, there appears to be good agreement between

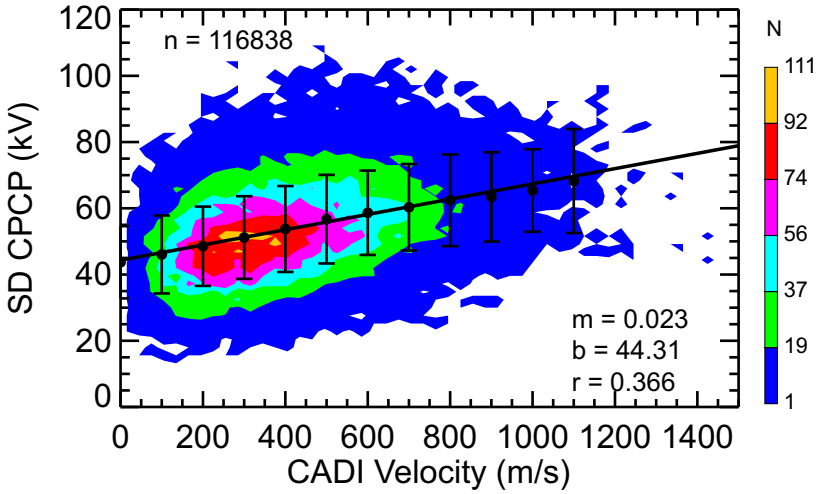

Figure 4.9: Contour plot of SuperDARN CPCP and CADI velocity for available data in the years 2000-2002. Black dots indicate average CPCP for each 100 m/s bin. Bars on each dot indicate the standard deviation for each bin. Linear regression (slope, y-intercept, correlation coefficient) is shown in the bottom right and number of points used in the plot is shown in the top left.

SuperDARN CPCP and RB CADI under quiet conditions.

4.7 Conclusions

In this chapter, it was shown that:

1. Overall, velocities of the PolarDARN radars and the Resolute Bay CADI differ by less than a factor of 2 in ∼85% of all cases for the range of velocities 100-800 m/s. This implies that one can consider data from these instruments for a statistical type of studies by merging them into a common data block. In individual events, the differences can be very large, and care must be exercised.

2. The discrepancies in the polarity of the PolarDARN and RB CADI occur about 5% of the time. The reasons for this effect were not able to be determined. Among potential factors are a difference in spatial coverage of the instruments and a difference in timing of measurements which is important for dynamical ionospheric events.

3. For cases of the same PolarDARN/RB CADI velocity polarity, the HF radars show somewhat larger velocity than the RB CADI for large velocities ($>$ 400 m/s). Since

the PolarDARN HF velocity is below the $\mathbf{E} \times \mathbf{B}$ magnitude, this result implies that the RB CADI underestimates (stronger that the PolarDARN radars) the $\mathbf{E} \times \mathbf{B}$ drift of the ionospheric plasma.

4. A comparison of the RB CADI velocity and SuperDARN CPCP showed linearity with the CADI velocity magnitudes in the range of 0-800 m/s.

The comparisons undertaken pose a question on the reasons for the effect of CADI underestimation of the $\mathbf{E} \times \mathbf{B}$ drift. The fact itself is not well-documented since little validation work has been done for CADI. In this view, future work on joint dataset that includes PolarDARN, CADI and ISR velocities is of great interest.

CHAPTER 5

SUPERDARN CPCP DEPENDENCE ON THE SOLAR WIND AND COMPARISON WITH MODELS

Since the late 1990s, a significant CPCP database has been accumulated by the SuperDARN community. Unfortunately, not all of these data are reliable. It was demonstrated in Chapter 3 that the number of points in an individual convection map, N_{map} is one of the crucial parameters that must satisfy certain conditions for proper estimates of the CPCP, since the FIT technique can be dominated by a startup convection model. In several previous studies (e.g., *Shepherd et al.*, 2003; *Koustov et al.*, 2009a) a database of CPCP was built by hand-picking those maps that visually had "reasonable" vector coverage around both the dusk and dawn convection cells' foci/vortices. Typically, such maps had several hundred points, but not all maps necessarily had an amount of points above a certain threshold. On the other hand, some maps had significant data coverage but were rejected for lack of points in one of the cells. This might imply that the database selected was actually dominated by some special conditions in the near-Earth space. In this Thesis, a simpler approach was adopted; only convection maps that have a "sufficient" number of points to constrain the FIT technique were considered. A similar approach was undertaken by others, such as *Grocott et al.* (2009).

To demonstrate the relationship of the SuperDARN CPCP with parameters in near-Earth space, one full year of data for the northern hemisphere were selected, the year 2000. A similar analysis was performed for 2001 and the results obtained are very consistent with what is reported here for 2000. A subset of simultaneous data in both hemispheres was also considered. The latter is certainly a smaller dataset. For the northern hemisphere dataset alone, N_{map} = 300 was chosen as the minimum threshold of individual map acceptance to

the database and N_{map} = 200 for the southern hemisphere in the joint N-S dataset. The threshold for data selection used in this Thesis is more stringent than the one adopted by *Grocott et al.* (2009) who used N_{map} = 200 points for only northern hemisphere data.

To advance some previous studies, the data were split into three separate seasons. The seasons were introduced as follows: Summer is May 1 - July 31, Winter is November 1 - January 31, and Equinox is March 1 - April 30 and September 1 - October 31. Consideration of various seasons was done to investigate the potential role of the ionospheric conductance due to photoionisation.

The initial part of the investigation involved considering CPCP dependence on various individual parameters of the near-Earth space that have been discussed in the literature and then investigating the dependence of the CPCP on functions that involve multiple parameters.

5.1 SuperDARN Map Coverage and the Range of External Parameters

First, the ranges of various parameters for the selected datasets were established. Data for the northern hemisphere dataset are reported here. The analysis showed that the subset of simultaneous N-S data has a similar distribution of parameters.

The first parameters that were considered were the magnitude and polarity of IMF B_z and B_y. Figure 5.1 is a contour plot of event occurrence in the B_z-B_y plane for the northern dataset. Overall, the data are distributed fairly uniformly in the plane with values within +/- 10 nT. The majority of points have small magnitudes of < 5 nT for both B_z and B_y. Minor tendencies in the denser regions (non-blue) include some predominance of negative B_z values for winter and some predominance of negative B_y values for summer.

Figure 5.2 presents histogram distributions for a number of parameters that have been discussed in the context of the CPCP saturation. These are solar wind ram pressure (Eq. 3.11), solar wind velocity, interplanetary electric field, the radius of the magnetosphere (Eq. 1.1), Alfvén-Mach number (Eq. 1.4) and the Alfvén velocity of the solar wind plasma (Eq. 1.6).

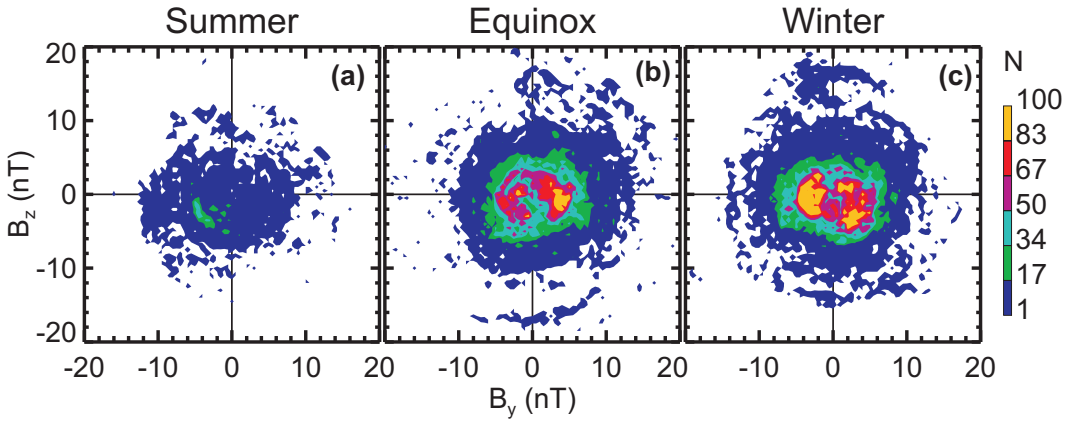

Figure 5.1: Contour plots for the number of occurrences in the IMF B_z-B_y plane where more than 300 map points were available in the northern hemisphere. Three seasons are considered separately.

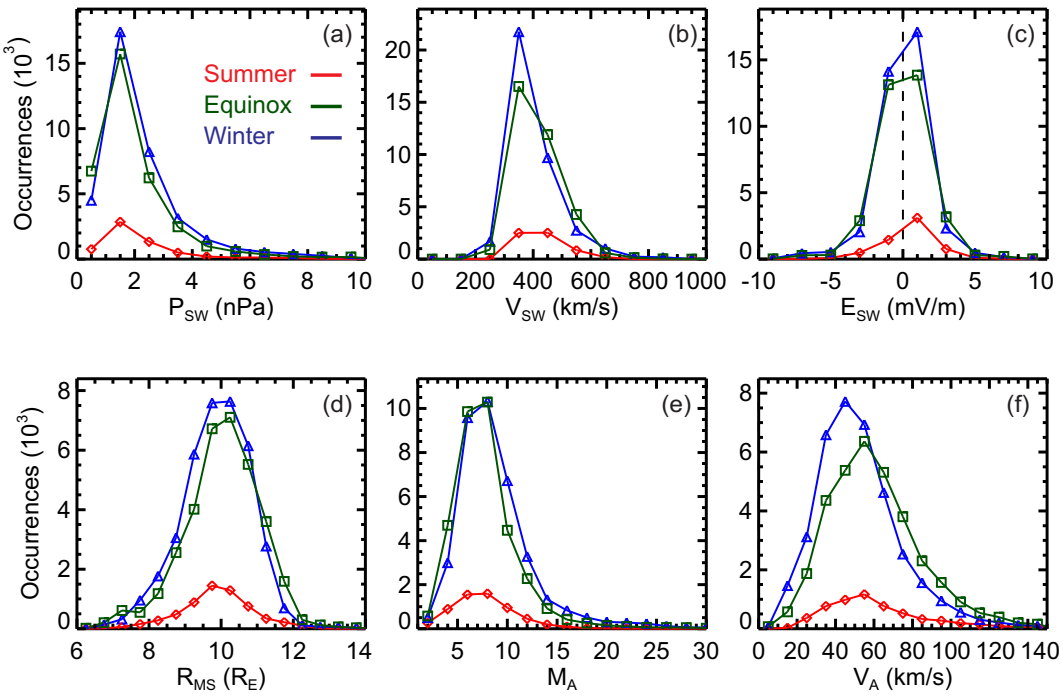

Figure 5.2: Histogram distributions for three seasonal datasets for a number of solar wind parameters that characterize the CPCP, according to various theories.

The distributions for the seasons are fairly consistent with each other although winter and equinox have many more points than summer. Typical values are p_{sw} from 1 to 2 nPa, v_{sw} from 300 to 400 km/s, E_{sw} from -3 to 3 mV/m, R_{ms} from 9 to 11 R_E, M_A from 5 to 10 and v_A from 30 to 60 km/s.

5.2 CPCP and the Interplanetary Magnetic Field

Magnetic reconnection, controlled by the IMF, has been considered the primary factor controlling the CPCP (e.g., *Shepherd*, 2007). It is not a surprise that numerous attempts have been made to establish the relationship between CPCP and B_z and B_y.

Figure 5.3 shows contour plots of the SuperDARN CPCP versus both B_z and B_y for B_z < 0, for the selected datasets. The CPCP increases linearly with negative B_z in the range of -8 to +8 nT. The relationship between CPCP and B_y was considered separately for positive and negative B_y, although both show a weak relationship. Maximum CPCP values are $\sim$100 kV.

Each plot in Figure 5.3 shows the parameters of the linear fits to the data: m is the slope of the line, b is the y-intercept and r is the correlation coefficient. The slopes for the B_z dependence are $\sim$-5 kV/nT while the B_y dependence slopes are only $\sim$1 kV/nT. Slopes for B_y are shown separately for positive and negative B_y. A seasonal trend can be seen with the slopes of the B_z dependence; the slope magnitudes get smaller as the amount of sunlight increases in the ionosphere, with the smallest slope in summer and the largest slope in winter. For equinox, for which the linear fit parameters are in between the summer and winter values, the CPCP can be represented as

$$\Phi_{SD}(\mathrm{kV}) = -5.3B_z(\mathrm{nT}) + 46. \tag{5.1}$$

At large negative B_z, winter and equinox data (Fig. 5.3b,c) show clusters of points that deviate from the linear dependence; these may imply a saturation in the rate of the CPCP increase with B_z. A similar situation is seen for positive B_z; the points are clustered around 20 kV.

While B_z shows the largest CPCPs for larger negative B_z values, the largest CPCPs for B_y are spread out more, and even occur for small B_y values, such as for the equinox (Fig.

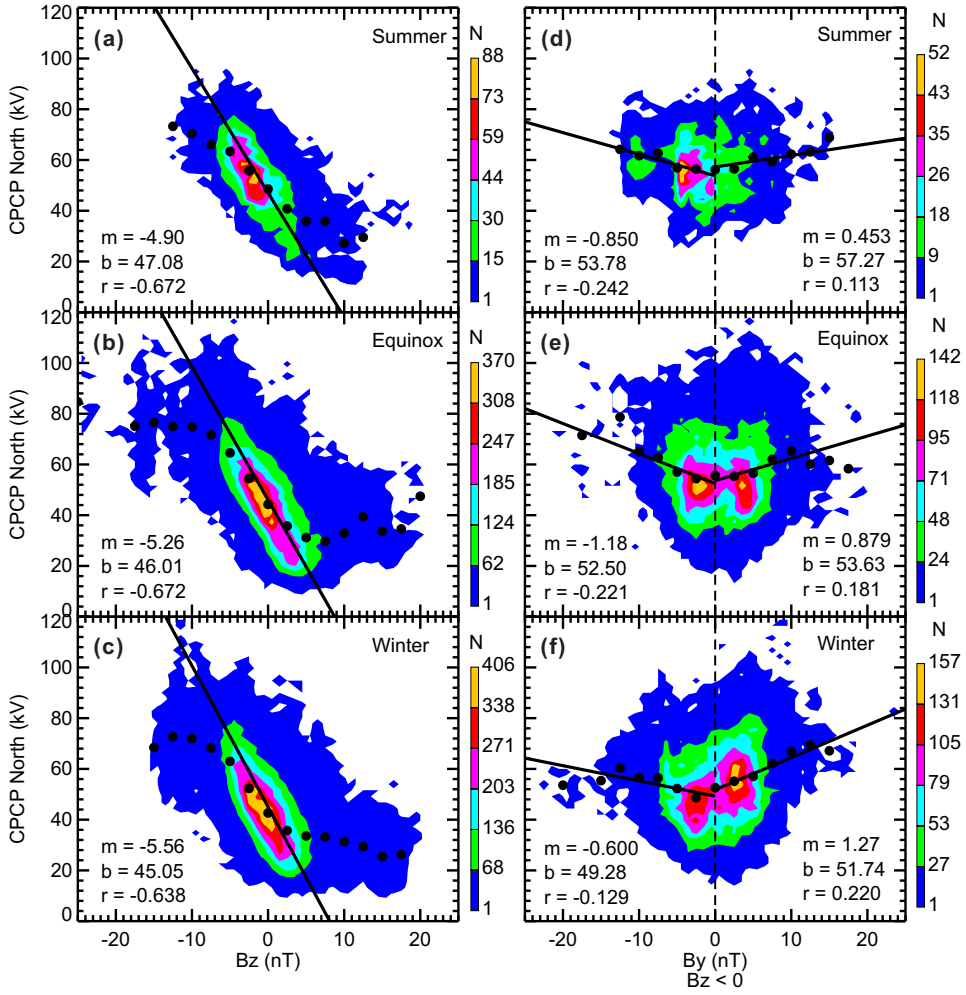

Figure 5.3: Contour plots of SuperDARN CPCP vs IMF B_z and B_y for three seasons. B_y data shown are only for periods when $B_z < 0$. Data trends are shown with binned values (black dots, bins of 2.5 nT) and linear fits. Each panel shows parameters of the linear fit (m is the slope of the line, b is the line's y-intercept and r is the correlation coefficient). B_y linear fits are done separately for positive and negative values.

5.3e). This, with the low correlation coefficient, implies that B_y on its own is not a good indicator of the CPCP. However, B_y is often used in combination with other parameters, such as B_z.

Dependence of the CPCP on the IMF magnitude is often considered. Typically, the tangential component of the IMF is used, B_T, which is involved in E_{KL}. The scatterplot of the CPCP versus B_T is presented in Figure 5.4. The general trend to increase is clearly seen here as well, although it is somewhat slower than the linear dependence with B_z. This is indicated by the linear slopes, which are $\sim$2 kV/nT here as opposed to $\sim$5 kV/nT. One can see a large cluster of points at small B_T that favours a stronger linear trend and a number of points for larger B_T that are below that linear dependence. The nonlinearity is also indicated by the binned values (red points, 2.5 nT bins). A square root fit (blue curve, functions given in Fig. 5.4) was also performed for all three seasons. The binned values match more closely with the square root fit than the linear fit.

The presented data are consistent with previous publications which insist on a linear trend (e.g., *Papitashvili et al.*, 1999; *MacDougall and Jayachandran*, 2001) with the exception that the slopes of the linear regression are about 2 times weaker in this case. *Papitashvili et al.* (1999) reported $\Phi = 33.1 + 11.5\,|B_z|$ for measurements with the DMSP satellites and a southward IMF, while *MacDougall and Jayachandran* (2001) had $\Phi = 44 + 10\,|B_z|$ with CADI measurements. On the other hand, *Ridley et al.* (1998) reported the slope of $\sim$4 kV/nT using the magnetometer-based AMIE technique, which is very close to what is shown here. A saturation effect for large B_y has been reported by *Mitchell et al.* (2010), but not enough points with large B_y were available in the northern dataset to say anything conclusively.

5.3 CPCP and the IMF Clock Angle

One other parameter dependent on B_y and B_z is the IMF clock angle. It has always been believed that the front side reconnection rate is dependent on the clock angle, here defined as $\theta_c = \arctan(B_y/B_z)$, following *Newell et al.* (2007). One would then expect this to affect the CPCP. In previous studies, a function of the clock angle in the form $\sin^n(\theta_c/2)$ was

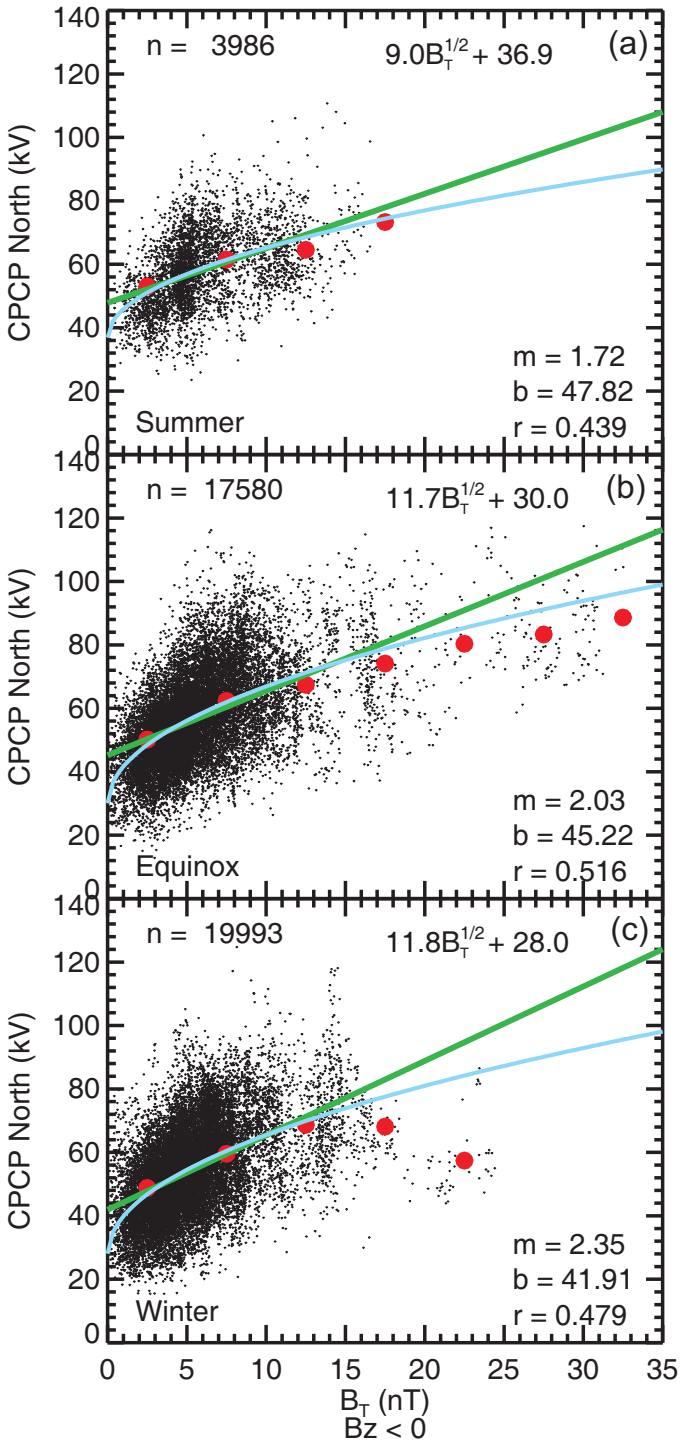

Figure 5.4: Scatterplots of SuperDARN CPCP vs IMF B_T for $B_z < 0$; three seasons are considered. Data trends are demonstrated with binned values (red dots, bins of 2.5 nT), a linear fit (green), and a square root fit (blue). Shown is the total number of points involved, the parameters of the linear fit (m is the slope of the line, b is the line's y-intercept and r is the correlation coefficient), and the square root fits.

considered.

Shown in Figure 5.5 is the northern SuperDARN CPCP versus $\sin^2(\theta_c/2)$, the function that showed the best correlation. CPCP versus $\sin^2(\theta/2)$, $\sin^3(\theta/2)$ and $\sin^4(\theta/2)$ were investigated. The correlation coefficients for the dependencies were, for the equinox dataset, 0.706, 0.689, 0.667, respectively. What is shown here is very consistent with the report by *Grocott et al.* (2009).

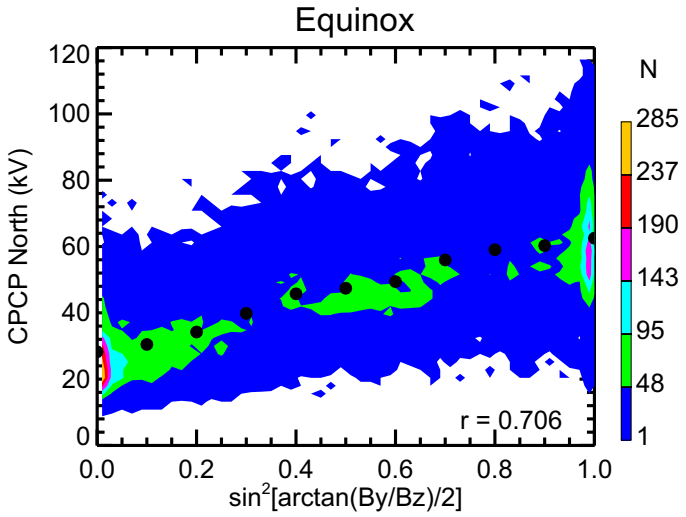

Figure 5.5: Contour plot of the SuperDARN CPCP vs $\sin^2(\theta_c/2)$. Black dots are binned values (bins of 0.1). The correlation coefficient is shown in the bottom right corner. Total number of points considered is n=34345.

5.4 CPCP and Solar Wind Velocity

The solar wind interplanetary electric field is ultimately transferred to the high-latitude ionosphere and produces the CPCP. Since the IEF is proportional to the solar wind velocity, one would expect the velocity to influence the CPCP.

Figure 5.6 shows the CPCP dependence on the solar wind velocity. The dependence does not appear to be strong, with almost no effect for summer. The correlation coefficients for all seasons are very low. Low correlation and a significant data spread indicate that no direct correlation exists between the CPCP and SW velocity. This does not rule out SW velocity contributing in combination with other parameters, such as the IMF strength or B_z.

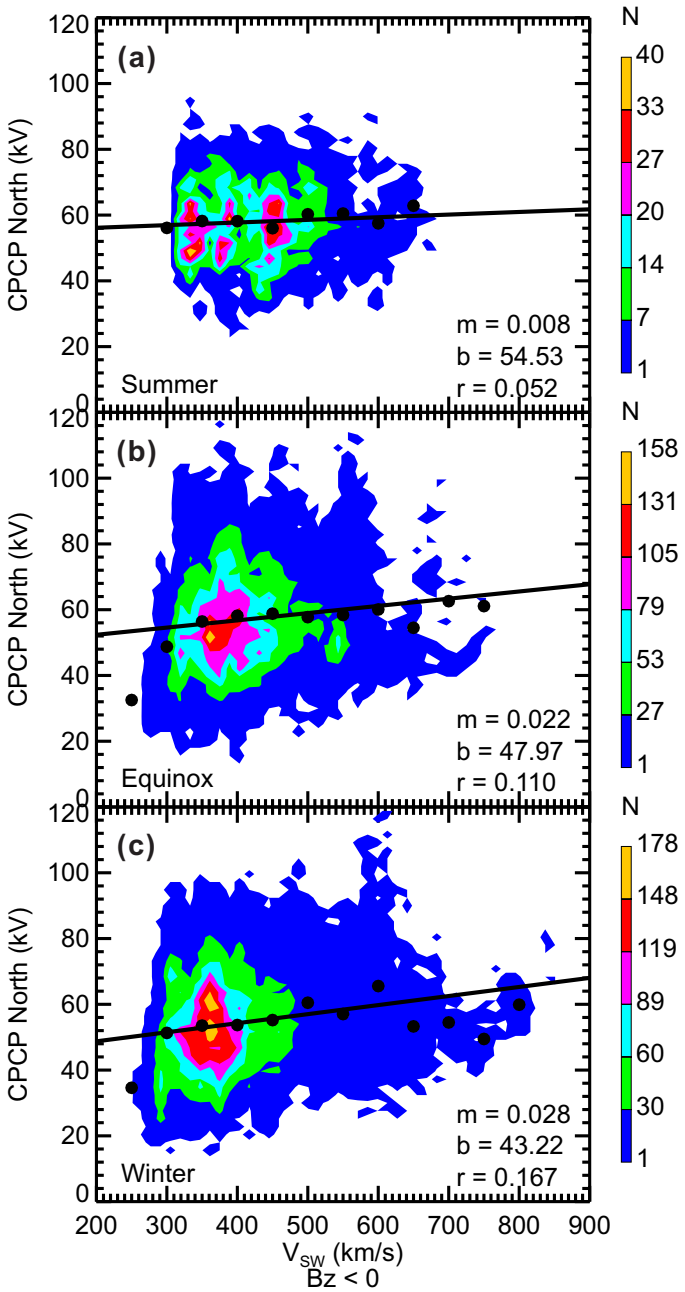

Figure 5.6: Contour plots of the SuperDARN CPCP vs solar wind velocity for three seasons. Black dots show average CPCP for each 50 km/s bin. Linear regression coefficients (slope, y-intercept, correlation coefficient) are shown in the bottom right corner of each plot. Best fit line is shown in black.

5.5 CPCP Dependence on IEF

The interplanetary electric field depends on both the IMF and solar wind velocity. Several definitions of the IEF have been used in literature. In this Thesis, the following definition of IEF was used:

$$E_{sw} = v_x B_z. \tag{5.2}$$

This form is the y-component of the full $-\mathbf{v} \times \mathbf{B}$ electric field. It should be noted that v_x, the x-component of the solar wind velocity, is always negative in the GSM coordinate system, so IEF > 0 corresponds to $B_z < 0$ and vice versa.

Figure 5.7 shows contour plots of the SuperDARN CPCP versus the IEF, again for 3 seasons separately. For all three plots, the points are spread between +/- 7 mV/m. Points for negative IEF are of less importance for this study as they correspond to northward IMF conditions ($B_z > 0$). All three plots clearly show the linear dependence for the majority of points. The departures from the linear trends are seen for |IEF| > 3 mV/m. These departures are better depicted by the binned values of the CPCP.

The data selected show a predominantly linear dependence between the CPCP and IEF. There are some points for IEF > 3 mV/m that suggest saturation. This effect is more noticeable in the equinox season where higher IEF values were available.

The linear fits are consistent with *Khachikjan et al.* (2008) and *Koustov et al.* (2009a). The slopes of the dependence show a seasonal trend; the highest slope is in the winter and lowest in the summer.

Saturation can also be seen for negative IEF. The CPCP appears to reach a minimum value of $\sim$30 kV. This is generally thought to be caused by secondary CPCP generators, such as quasi-viscous interaction or nightside processes, independent of dayside reconnection which is still present when dayside reconnection is not, possibly contributing up to 30 kV to the CPCP (e.g., *Milan*, 2004).

While the selected data do not contain enough points in the saturation regime, they still provide an opportunity to investigate the dependence of the CPCP upon various parameters of the near-Earth space.

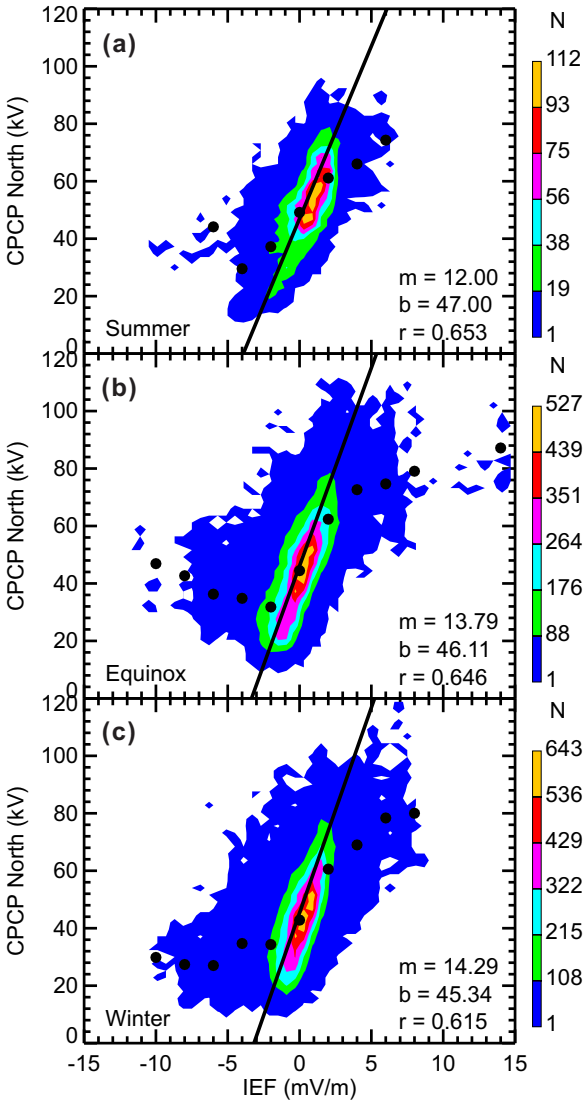

Figure 5.7: Contour plots of SuperDARN CPCP vs IEF for three seasons. Data trends are shown with binned values (black dots, bins of 2.5 mV/m) and linear fit (black line). Each panel shows the total number of points involved and the parameters of the linear fit, slope, y-intercept, and correlation coefficient.

5.6 Effect of the Size of the Magnetosphere

A number of researchers have expressed the opinion that the CPCP is strongly controlled by the size of the magnetosphere; a larger magnetosphere provides a longer reconnection line and generates a larger magnetospheric voltage. For example, *Ridley* (2007) hypothesized that CPCP is simply proportional to the radius of the magnetosphere, R_{ms}. *Khachikjan et al.* (2008) considered a small set the SuperDARN CPCP data and sorted the data according to the R_{ms}. It was found that with R_{ms} decrease, the slope of the CPCP-IEF dependence decreased dramatically. In this section this effect was investigated with a significantly larger dataset.

Figure 5.8 shows the slopes of the CPCP-IEF dependence for 1 R_E bins of the magnetosphere radius, considering three seasons. There is a clear trend for the slopes to increase with the R_{ms} bin values. Since the magnetopause radius is proportional to $p_{sw}^{-1/6}$, a higher pressure implies a smaller radius and thus a lower rate of CPCP increase with the IEF, which is an indicator of the saturation effect.

This trend is reinforced by Figure 5.9, which plots the slopes and y-intercepts of the linear fits against the magnetosphere radius bins used in Figure 5.8. The slopes increase almost linearly with the magnetosphere radius and the y-intercepts decrease almost linearly. The only exception is the 6-7 R_E bin, which breaks the trend for both slope and y-intercept. This could indicate that the effect is limited below a certain radius or could be due to the bins for the smallest magnetosphere radii having fewer points than the rest of the bins.

A seasonal dependence, presumably from the ionospheric conductance, is present in Figure 5.8. The slopes are highest in the winter, when the conductance would be smaller. This might imply that the CPCP saturation effect could occur at smaller IEF in the winter time, consistent with *Koustov et al.* (2009a) who reported faster overall CPCP increase winter time and saturation beginning at a lower IEF value than in summer. *Koustov et al.* (2009a) did not split the data by R_{ms} bins so that the saturation effect was evident. It could be that the saturation effect seen by the SuperDARN radars is simply an apparent effect; it is seen because of over-plotting data for various R_{ms}.

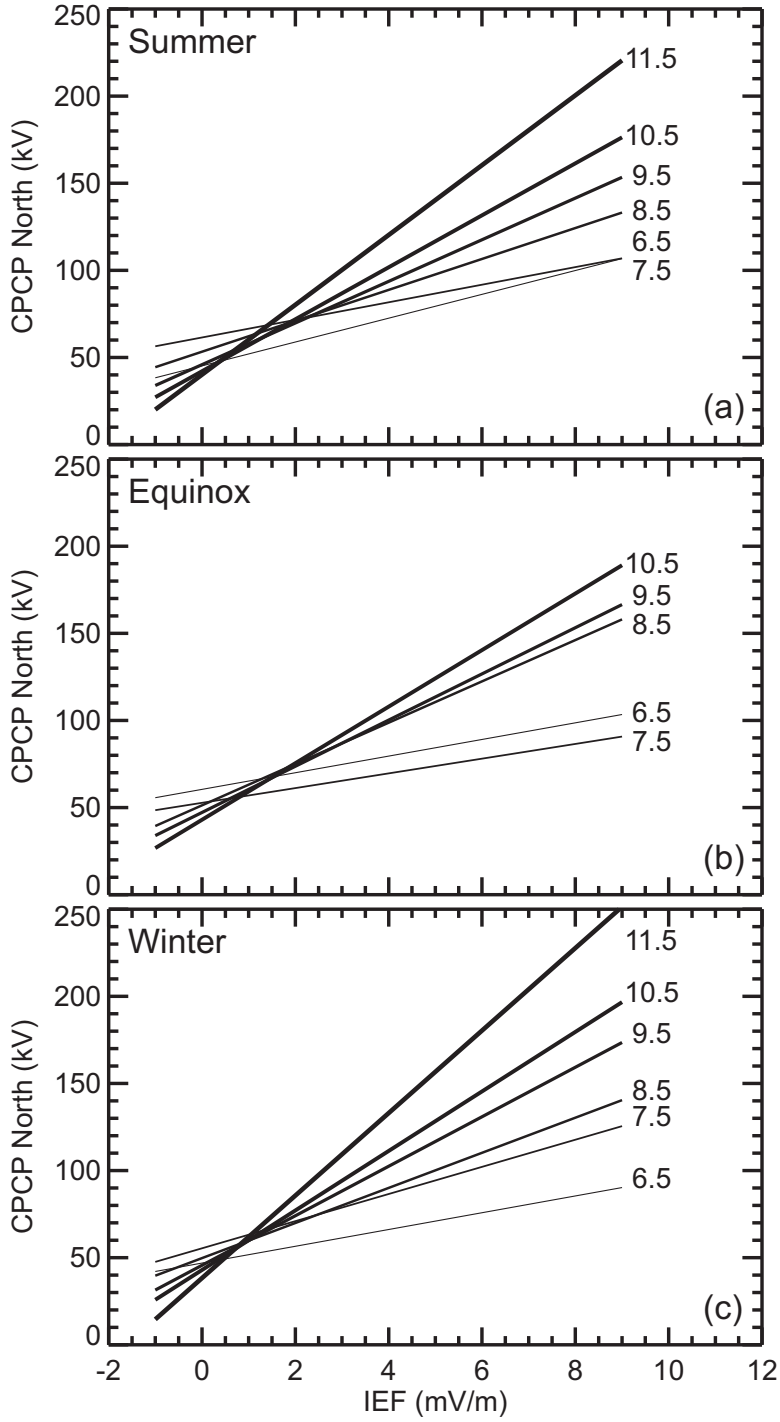

Figure 5.8: The linear fit lines for the SuperDARN CPCP dependence upon IEF for 1 R_E bins of the magnetosphere radius R_{ms} (values by each line are midpoints of the given bin, in units of R_E). Three seasons are considered separately.

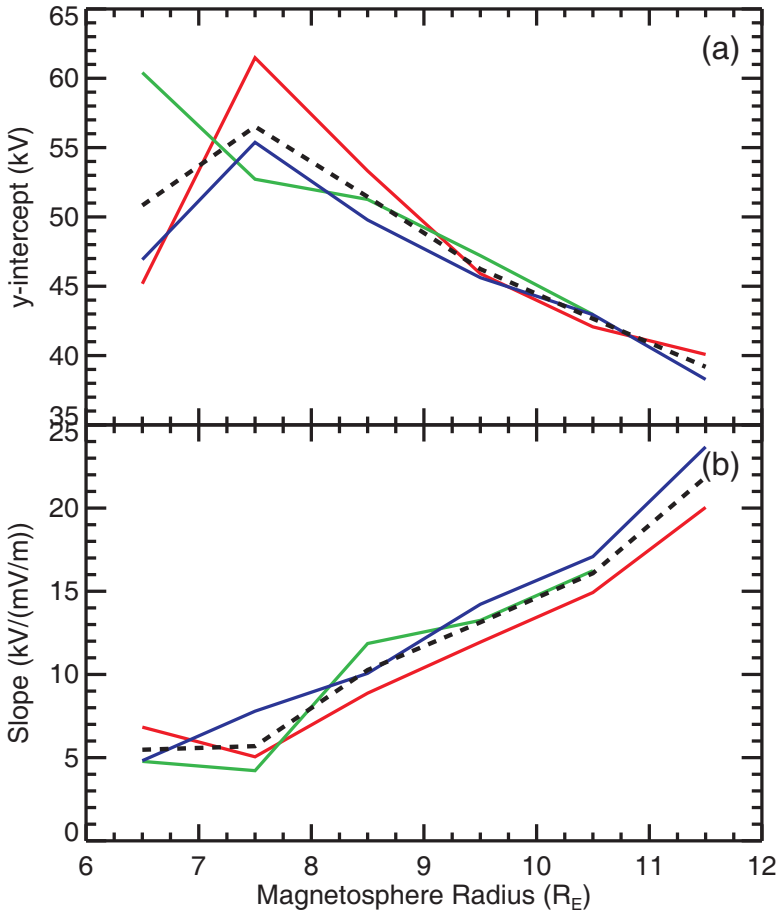

Figure 5.9: The coefficients (a) b (y-intercept) and (b) m (slope) in the linear dependence of the CPCP upon IEF (CPCP=$mE_{sw}+b$) for various magnetosphere radius bins R_{ms} for the data presented in Fig. 5.8. Three seasons are shown, winter (blue), equinox (green) and summer (red).

The y-intercepts are very similar to *Khachikjan et al.* (2008) (Table 5.1), although the slopes here are much larger. This could be due to the technique used in this Thesis to use perpendicular offsets in the linear regression, not vertical offsets, as is typically done. The intersection of the fit lines corresponding to various R_{ms} is not at 3 mV/m (*Khachikjan et al.*, 2008) but at 1-2 mV/m depending on season, with smaller values for winter.

5.7 SuperDARN CPCP and SW Coupling Functions

So far, it has been shown that the SuperDARN CPCP correlates with several parameters of the near-Earth space: IMF B_z, B_y (B_T), R_{ms}, and IMF clock angle. These factors are

Table 5.1: Y-intercepts and slopes of linear fit lines from Figs. 5.9.

Data Set	R_{ms} bin (R_E)	6.5	7.5	8.5	9.5	10.5	11.5
Khachikjan et al. (2008)	y-int	55.6	60.2	55.3	48.9	41.9	40.4
	slope	2.4	1.8	3.1	6.1	8.2	8.9
Summer	y-int	45.2	61.5	53.3	45.9	42.1	40.1
	slope	6.84	5.05	8.88	11.9	14.9	20.0
Equinox	y-int	60.4	52.7	51.3	47.2	43.0	n/a
	slope	4.78	4.22	11.9	13.3	16.2	n/a
Winter	y-int	46.9	55.4	49.8	45.6	42.9	38.3
	slope	4.82	7.79	10.1	14.2	17.1	23.7

thus very likely to reflect the energy transfer from the solar wind into the ionosphere since SuperDARN CPCP is a global parameter. To our mind, these dependencies must be considered while a most reliable coupling function is inferred. In this respect, it is noted that, in the past, SuperDARN CPCP has not been tried much. *Koustov et al.* (2009a) considered a limited SuperDARN dataset and found that the Newell coupling function provides better data clustering and correlation coefficient as compared to the IEF, reconnection electric field and PCN index. In this section a more extensive database is considered to assess how various coupling functions correlate with SuperDARN CPCP.

For the analysis, northern SuperDARN CPCP was compared to various coupling functions discussed in the literature. Three seasons were considered separately. All the coupling functions were inferred from the ONMI IMF and solar wind data with proper delay as discussed in Section 3.3. The correlation coefficient was calculated assuming that the relationship is linear.

Table 5.2 presents the obtained correlation coefficients. One can see that the best correlation is achieved by the variant of the *Wygant et al.* (1983) function closely followed by the functions by *Lyatsky et al.* (2007) and *Newell et al.* (2007). For these 3 best functions, winter data show better correlation and summer data show worse. The common feature of these functions is the power of the B_T term, with the exponent being 1/2 or 2/3. The other common feature is the dependence upon clock angle being close to $\sin^2(\theta_c/2)$. v_{sw} is involved in a different way in the best parameters but since CPCP does not depend strongly upon v_{sw}, these differences are not very critical.

Table 5.2: List of solar wind coupling functions and their correlation coefficient with SuperDARN CPCP for 3 seasons.

			Corr. Coeff., r		
Name	Functional Form	Reference	Summer	Winter	Equinox
ε	$v_x B_T^2 \sin^4(\theta_c/2)$	*Perrault and Akasofu* (1978)	0.522	0.361	0.504
E_r	$v_x B_T \sin^2(\theta_c/2)$	*Kan and Lee* (1979)	0.649	0.642	0.678
Φ_m	$v_x B_T \sin^2(\theta_c/2) p_{sw}^{-1/6}$	*Siscoe et al.* (2002b)	0.644	0.695	0.696
E_{rl}	$v_x B_T \sin^3(\theta_c/2)$	*Reiff and Luhmann* (1986)	0.664	0.639	0.683
E_{wyg}	$v_x B_T \sin^4(\theta_c/2)$	*Wygant et al.* (1983)	0.657	0.623	0.672
$E_{wyg}^{1/2}$	$v_x^{1/2} B_T^{1/2} \sin^2(\theta_c/2)$	Variant on E_{wyg}	0.736	0.779	0.747
E_{pud}	$n_{sw}^{-1/2} B_T^2 \sin^3(\theta_c/2)$	*Pudovkin et al.* (1985)	0.487	0.490	0.506
E_{TL}	$n_{sw}^{1/2} v_x^2 B_T \sin^6(\theta_c/2)$	*Temerin and Li* (2006)	0.541	0.487	0.549
E_c	$v_x^{4/3} B_T^{2/3} \sin^{8/3}(\theta_c/2)$	*Newell et al.* (2007)	0.680	0.705	0.702
E_{lyat}	$v_x B_T^{1/2} \sin^2(\theta_c/2)$	*Lyatsky et al.* (2007)	0.710	0.758	0.731

It should also be noted that coupling functions involving solar wind density (n_{sw}) or solar wind pressure (p_{sw}) performed poorly, with the exception of Φ_m, which differed from E_{KL} only by the term $p_{sw}^{-1/6}$ (R_{ms}), showed some improvement over E_{KL} in terms of correlation.

5.8 CPCP and Solar Wind Pressure

An increase in the solar wind ram pressure implies an increase in the intensity of the external driver, and one might generally expect larger CPCPs established in the high latitude ionosphere. The relationship between the CPCP and p_{sw} has been investigated in a number of studies (e.g., *Boyle et al.*, 1997; *Shepherd et al.*, 2003; *Ober et al.*, 2003; *Khachikjan et al.*, 2008). There is no general consensus on the issue except for the major one: the effect is not very strong. It was decided that a closer look at this relationship was necessary. With the data already presented in the previous section, one cannot expect a strong dependence because the radius of the magnetopause is closely related to the ram pressure and the dependence of CPCP on R_{ms} was found to be weak. Data are presented here for negative B_z only.

Figure 5.10 demonstrates tendencies seen on plots for other seasons. A tendency can

be seen for CPCP to increase with pressure, however the effect is not strong. The correlation coefficient was low for all seasons, the slope of the best fit line was between 1.0 and 1.5 kV/nPa, and the y-intercept was in the range of 50-55 kV. The range of CPCP for each bin is as large as 80 kV. An increase in CPCP with pressure is consistent with a number of studies where a sudden p_{sw} increase apparently leads to a jump in ionospheric convection velocity (e.g., *Coco et al.*, 2005).

Some studies (e.g., *Ridley*, 2005; *Khachikjan et al.*, 2008) use ram and magnetic pressure ($p_{sw} = \rho v^2 + B^2/2\mu_0$), claiming that under extreme conditions, magnetic pressure can be on the same order as ram pressure. In this study, the average magnetic pressure was 0.01 nPa and in the most extreme case, the magnetic pressure did not exceed 0.7 nPa.

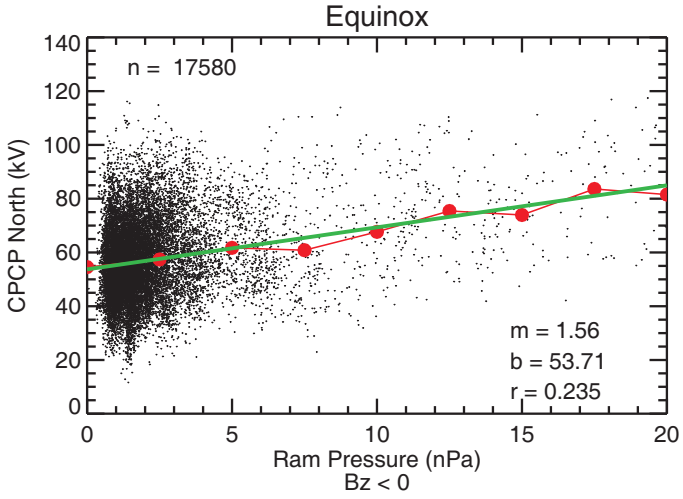

Figure 5.10: Scatterplot of the SuperDARN CPCP North vs SW pressure for equinox. Red dots are binned values (bins of 2.5 nPa) and the green line is the linear fit to the data (parameters of the fit shown in the right bottom corner). Total number of points considered was n=17580.

Next, the same dataset was considered but for different IEF bins. Figures 5.11a,b,c show the CPCP plotted against p_{sw} with bins of 1 nPa for three seasons, separated by IEF bins of 1 mV/m. To a first approximation, there is no direct dependence on pressure; the correlation coefficient for most of the IEF bins was under 0.2.

Figure 5.11d shows the slopes for the linear fit plotted against IEF bins from Figs. 5.11a,b,c. The dashed black line is the average of the three seasons. The slopes are higher at small (1-2 mV/m) and large (4-5 mV/m) IEF and are lowest at intermediate IEF bins ($\sim$3 mV/m).

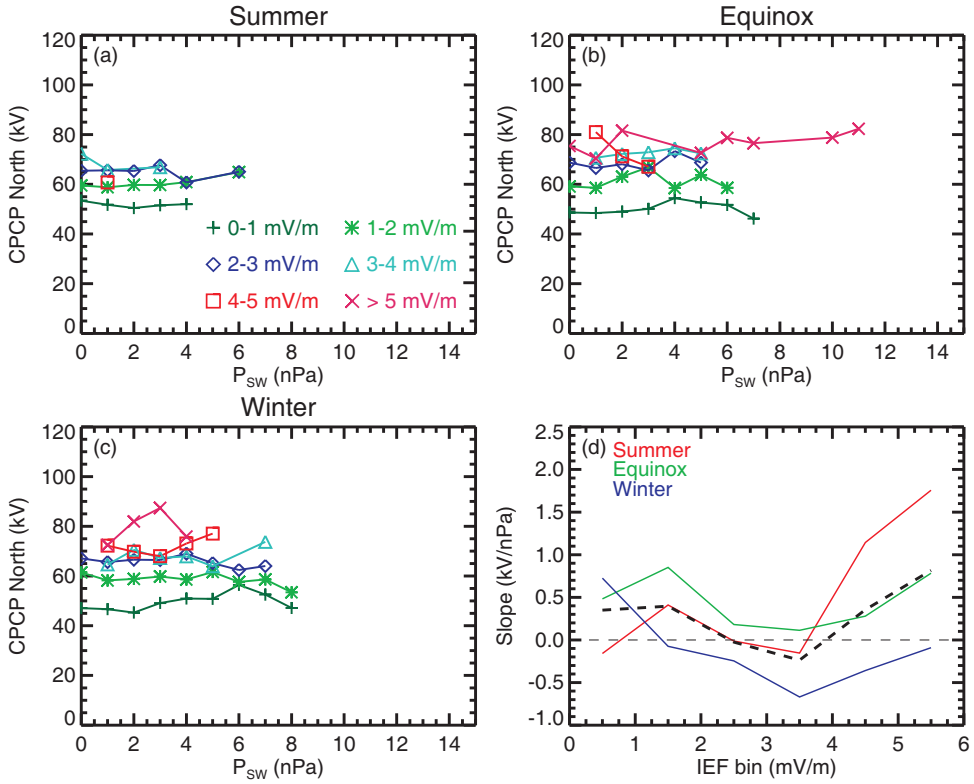

Figure 5.11: (a-c) Binned values for the scatterplots "SuperDARN CPCP-solar wind ram pressure" for three seasons. The data was divided into six IEF bins (units of mV/m): 0-1 (green), 1-2 (light green), 2-3 (blue), 3-4 (cyan) 4-5 (red) and > 5 (pink). (d) Slopes of the linear fit versus IEF bins for the scatterplots "SuperDARN CPCP-solar wind ram pressure" for three seasons: winter (blue), summer (red) and equinox (green). The dashed black line is the average of all seasons.

These results are at odds with *Khachikjan et al.* (2008) (who had a more limited dataset and used many points that were affected by the startup convection model). *Khachikjan et al.* (2008) reported CPCP increase at small IEF values (1-2 mV/m) and decrease at large values (4-5 mV/m). Our more extensive data set shows an increase for small IEFs, but the rate slows down and there is almost none, if not a decrease, at IEF ∼2-3 mV/m. For larger IEFs, the CPCP increases with p_{sw}. The trends are, however, very subtle. They are much slower than expected within the Hill-Siscoe model, according to which CPCP is proportional to $p_{sw}^{-1/6}$ for small IEFs and $p_{sw}^{1/3}$ for the regime of saturation (although, our data do not reach that stage).

Computer modelling by *Merkin et al.* (2005b) showed a tendency for CPCP to decrease versus pressure for small conductances and a minor increase at large conductances.

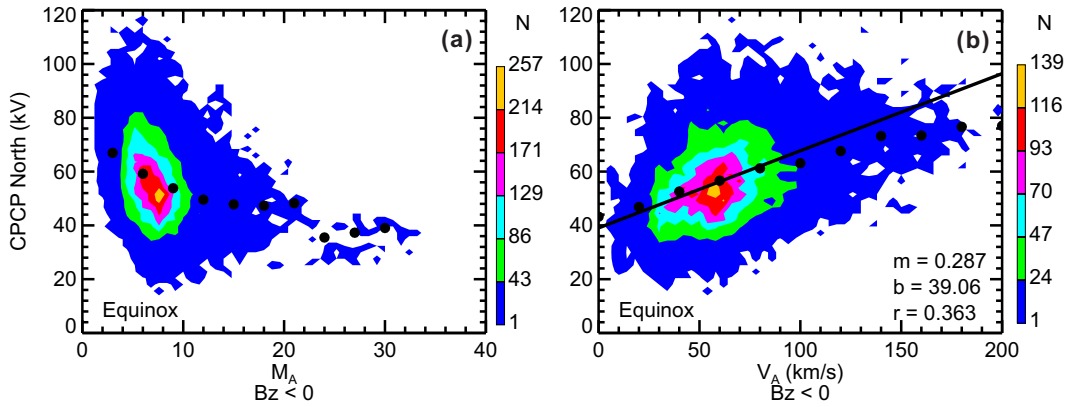

Figure 5.12: Contour plots of SuperDARN CPCP plotted versus (a) the SW Alfvén-Mach number and (b) Alfvén velocity for equinox 2000.

Our data are somewhat in agreement with this, as Figure 5.11d shows winter (lower conductance) having mainly negative slopes and summer and equinox generally have positive slopes.

5.9 Alfvén-Mach Number and the SuperDARN CPCP

A number of studies have suggested an influence on the CPCP by the Alfvén-Mach number, M_A (e.g., *Ridley*, 2007). The Alfvén-Mach number is one of the factors involved in the bow shock jump condition (Eq. 1.2), which determines the increase in IMF strength and SW density as the solar wind crosses the bow shock into the magnetosheath. Under typical conditions, M_A is large and the jump condition is roughly constant, staying between $\sim$3.5-4, but this value drops to 2-3 as M_A decreases below 3. *Ridley* (2007) claims this to be one factor involved in the saturation effect.

Figure 5.12a shows a contour plot of SuperDARN CPCP against M_A for the equinox dataset. There is a trend that shows a CPCP increase for decreasing M_A. The functional dependence of CPCP on M_A appears to be either a decaying exponential (as used by *Ridley* (2007)) or an inverse function.

The definition for M_A (as given by Eq. 1.4) is one way to view the parameter, but a

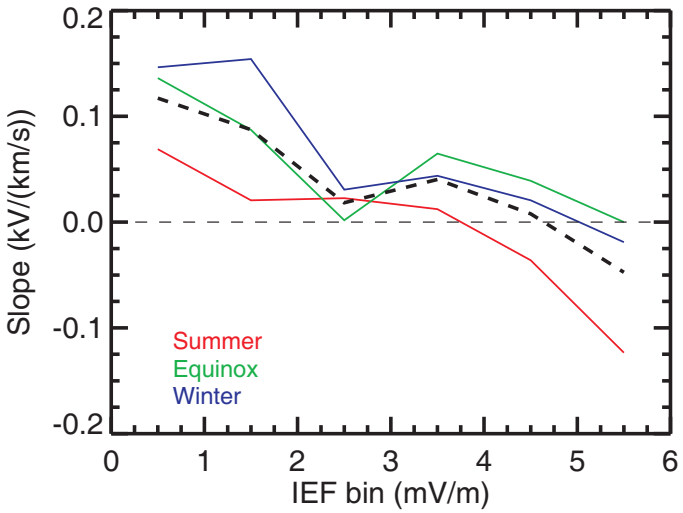

Figure 5.13: Plot of the best fit slope of CPCP vs v_A for varying IEF bins plotted against the average IEF value of each bin. Red/green/blue lines depict summer/equinox/winter datasets.

more revealing one is

$$M_A \approx \frac{\sqrt{\mu_0\, p_{sw}}}{B_T}. \tag{5.3}$$

Here, M_A is written in terms of parameters discussed above. It is approximate, as M_A is typically defined with the full IMF strength $B = \sqrt{B_x^2 + B_T^2}$, although there is little to no difference for small B_x. M_A is proportional to the square root of the solar wind pressure, which has little correlation with CPCP, and inversely proportional to the IMF strength, which had decent correlation with CPCP. With the inverse-like relationship between M_A and CPCP, it would appear that B_T dominates this dependence.

Figure 5.12b shows a contour plot of SuperDARN CPCP against Alfvén velocity. The relationship appears to be somewhat linear, although a large variance in CPCP data is present. As with M_A, the linear relationship is likely due to v_A being proportional to B_T.

To further investigate the effects of v_A, the slope of the CPCP versus v_A relationship for different IEF bins were plotted against the IEF values (Fig. 5.13). The slopes appear to decrease as the IEF value increases. This could be an indication of v_A affecting the growth of CPCP with the IEF, similar to what was seen with R_{ms}.

5.10 Comparison of Simultaneous SuperDARN CPCP in Both Hemispheres

The role of the ionospheric conductance is to "short out" the CPCP. In Ohm's law (Eq. 2.6), for a constant current, a higher conductance implies a lower electric field, implying a lower voltage. Thus, theoretically, it is expected that a sunlit ionosphere will show smaller CPCPs than a dark ionosphere, assuming the same currents are being applied.

Data for the northern hemisphere alone do not show a fundamental difference between statistically typical values for summer and winter. One possibility for this is the possibility that typical conditions in the solar wind are different enough between seasons to mask any conductance effects. To evaluate the differences between CPCP data in a dark and sunlit ionosphere, simultaneous data from both hemispheres were considered.

Figure 5.14 contains contour plots of northern SuperDARN CPCP data plotted against southern CPCP and relevant statistics. The CPCP in both hemispheres does not appear to differ significantly on average, with a mean difference of 1.5 kV in the summer and 3.2 kV in the winter, both favouring the northern hemisphere. Northern CPCP data are greater more than 50% of the time for both seasons.

As mentioned earlier, the threshold for CPCP data was N_{map}=300 for the northern hemisphere and N_{map}=200 for the southern hemisphere. The statistics were consistent when considering either N_{map}=200 or N_{map}=300 for both hemispheres.

So far it has been assumed that both hemispheres receive roughly the same energy from reconnection, but this is not necessarily true. *Lyons and Williams* (1984) show that particle precipitation along field lines into the ionosphere can differ between hemispheres by as much as one order of magnitude, depending on the direction of the IMF; in particular, B_x is said to be the cause, with $B_x < 0$ causing greater precipitation in the northern hemisphere and $B_x > 0$ doing the same for the southern hemisphere. The cause of this is the geometry between the IMF and geomagnetic fields at the reconnection site. Reconnection is said to occur where the IMF and geomagnetic field are antiparallel, but the addition of B_x will alter the angle of the IMF relative to the geomagnetic field, shifting the reconnection site

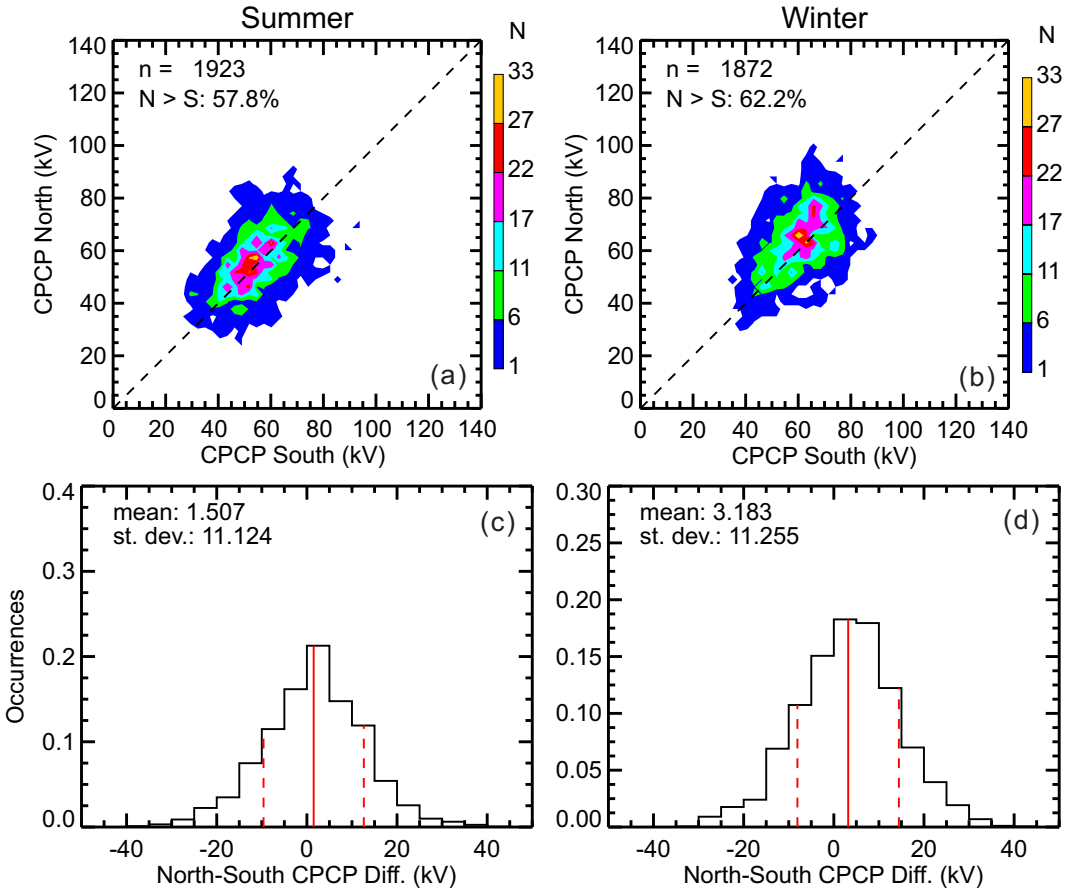

Figure 5.14: Northern vs southern SuperDARN CPCP for (northern) (a) summer and (b) winter 2000. Number of points is shown in the top left corner along with the percentage of points where northern CPCP is greater than southern CPCP. (c) and (d) show histograms of the CPCP difference, north minus south, of (a) and (b), respectively.

northward or southward depending on its sign, northward for $B_x < 0$ and southward for $B_x > 0$. This, in turn, causes an asymmetry in particle precipitation, which may imply that the R1 currents applied to each polar cap will undergo a similar asymmetry.

To further investigate this, the difference in CPCP between hemispheres was plotted against both B_x and B_y (Fig. 5.15). A trend can be seen for both seasons for B_x and B_y. The difference between northern and southern CPCP is larger for positive B_y and for negative B_x. Seasonal differences are negligible. B_z was also investigated but no trends were found.

While the CPCP difference is smaller for negative B_y and positive B_x, it should be noted that this does not imply that southern CPCP will be larger than the northern. Figure 5.15a shows CPCP differences up to 40 kV favouring both northern and southern data near -10 nT.

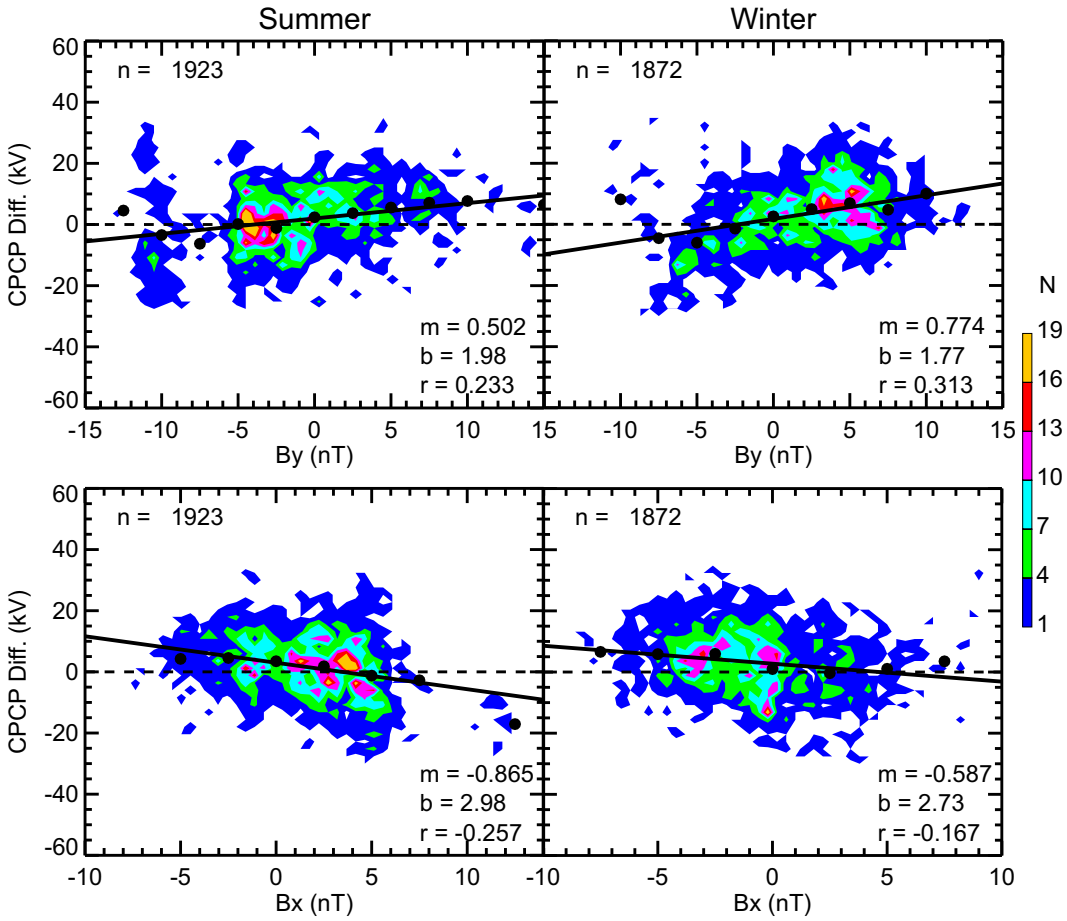

Figure 5.15: Contour plots of the CPCP difference, north minus south, for (a,b) B_y and (c,d) B_x for (northern) summer and winter.

5.11 SuperDARN CPCP and Expectations from Previous Work

The presented SuperDARN data demonstrate that the CPCP is affected by a number of parameters in the near-Earth space that might be, generally speaking, inter-related themselves. Theoretical understanding of these factors, as described in Chapter 2, is far from complete. In this section, some theories and predictions, published so far, were tested with the dataset considered in this Chapter. For this comparison, real values of the SW and IMF parameters were used, contrary to other studies where statistically average parameters were employed, for periods of concurrent SuperDARN measurements. Also, various seasons were considered; however, surprisingly, the results were very similar, independent of season. For this reason, only the winter data is discussed here.

5.11.1 Boyle Empirical Model and SuperDARN CPCP

In Figure 5.16a,SuperDARN data is compared with the *Boyle et al.* (1997) empirical relation given by Equation 2.1. The solid black line shows the best fit line. This line shows that for SuperDARN CPCP < $\sim$50 kV, the radar data are larger than the Boyle model predictions and for SuperDARN CPCP > $\sim$50 kV, the radar data are smaller than the Boyle model. The slope of the line is 2.3, indicating that, overall, the Boyle model potentials are much larger than the SD potentials. This is especially seen for Boyle CPCP > 100 kV. *Khachikjan et al.* (2008) reported very similar results. This result is not surprising when considering that the Boyle model is based on DMSP data, which is known to show larger values than SuperDARN CPCP.

The other difference with the Boyle model is that the SuperDARN measurements show hardly any seasonal variation with CPCP, contrary to season differences and an equinoctial maxima reported by *Boyle et al.* (1997). *Boyle et al.* (1997) also had a dependence on the SW pressure, which improved when the SW density term was removed, resulting in their v^2 term. SuperDARN CPCP showed a very weak, if any, dependence on SW pressure and velocity (Figs. 5.10,5.6). Among the agreements with the Boyle model are a strong

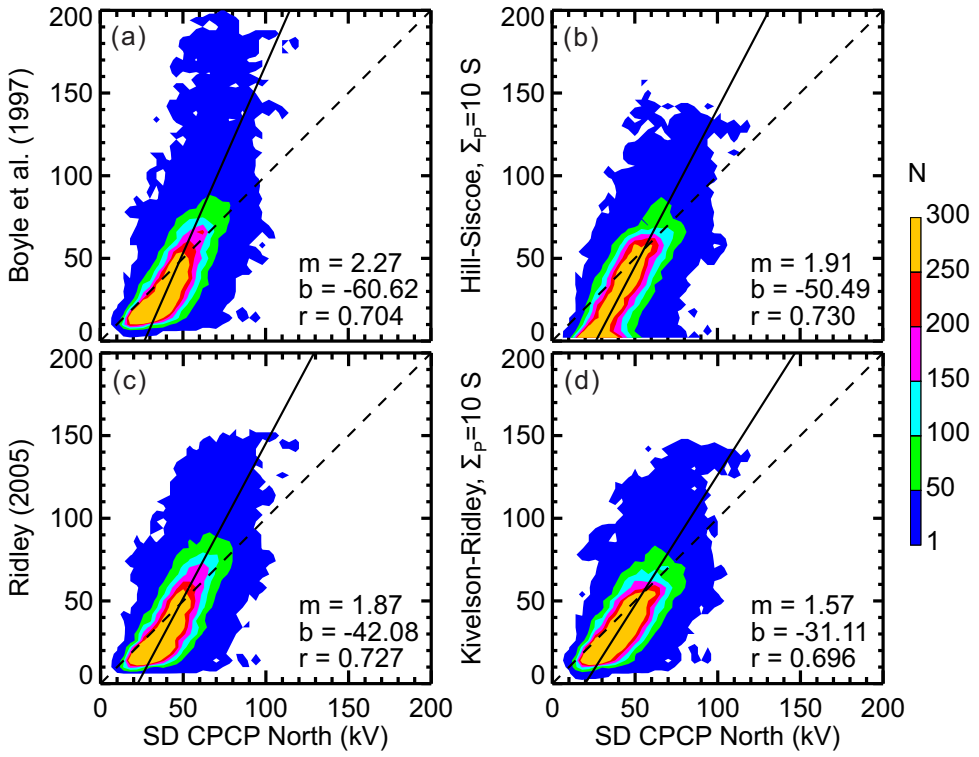

Figure 5.16: Contour plots of expected CPCP according to several models and SuperDARN CPCP. Linear regression coefficients are shown in the bottom right corner. Dotted black line shows one-to-one agreement. The solid black line is the best fit.

dependence upon B_z, a dependence on the IMF clock angle, and no detectable dependence upon B_x (see their Fig. 3). It should be noted that *Boyle et al.* (1997) selected data for periods with reasonably stable IMF conditions. The same cannot be said for the dataset in the current study.

5.11.2 Hill-Siscoe Model and SuperDARN CPCP

In Figure 5.16b, the Hill-Siscoe model predictions (Eq. 2.13) for the ionospheric conductance of Σ_P=10 S are plotted against SuperDARN data. The contour plot here looks very similar to the one in Figure 5.16a except the model does not predict CPCP values as large as the model by *Boyle et al.* (1997). The slope of the linear fit line and the correlation coefficient are slightly better, but a slope of 1.9 is still very large.

The comparison performed is in line with previous comparisons by *Shepherd et al.* (2003) and *Khachikjan et al.* (2008). It is noted that *Shepherd et al.* (2003) reported on

the best agreement between SuperDARN data and Hill-Siscoe model expectations for Σ = 23 S. This value is unreasonably high, and *Shepherd et al.* (2003) put forward a number of explanations why the agreement does not work out, including the possibility of tweaking the ξ term in Equation 2.6, which was determined by MHD model results. At the end of their discussion, the authors stated that it is possible that the "assumptions used to derive equation (1) are incorrect" (see Eq. 2.13). This seems to be a likely explanation, in particular, the large value of 57.6 as a coefficient. Indeed, beside overall disagreement, our data do not support the Hill-Siscoe model prediction that the CPCP depends strongly on the ionospheric conductance. This finding is echoed by the conclusions by *Haaland et al.* (2007) and *Förster et al.* (2007) who considered CLUSTER data. The Boyle equation is also conductance independent. Weak, if any, CPCP dependence on the ionospheric conductance seems to contradict theoretical expectations, notably the computer modelling, (e.g., *Borovsky et al.*, 2009). This discrepancy between the SuperDARN data and theoretical expectations is too important to ignore in future work.

One point of agreement between SuperDARN CPCP and the Hill-Siscoe model is the inclusion of $p_{sw}^{-1/6}$ in Φ_m. As discussed briefly in Section 5.7, this factor, reflecting the magnetosphere radius, improved linear correlation between SuperDARN CPCP and E_{KL}.

5.11.3 Ridley (2005) Model and SuperDARN CPCP

Figure 5.16c compares the *Ridley* (2005) formulation (Eq. 2.17) with SuperDARN data. The appearance is similar to that for *Boyle et al.* (1997) for small CPCPs, but Ridley's formula only reaches CPCP up to 150 kV, as opposed to 200 kV. Disagreements are still large for large CPCPs. The overall slope is similar compared to the Hill-Siscoe model.

Ridley (2005) included CPCP dependence upon the Alfvén-Mach number. His suggestion is that for small Mach numbers (large B_T) the reconnection contribution to the CPCP in the Boyle's model has to be multiplied by the term $1 - \exp(-M_A/3)$. With IMF increase, this would decrease the predicted CPCP and cause saturation. The current dataset does not cover the CPCP saturation regime so the importance of such a term cannot be commented upon.

Ridley (2005) hypothesized that the CPCP is proportional to the radius of the magnetosphere. Our data partially support this notion, but it is not clear whether this support is absolutely valid. It was shown that if the CPCP data are binned by the R_{ms} values, for each bin of the magnetosphere size the CPCP variation upon the IEF is different, with a smaller response at larger IEF. The last result might be interpreted as an indicator of the saturation effect at large IEFs. On the other hand, when the CPCP was plotted versus R_{ms} or p_{sw} for various bins of IEF, no strong dependence was found, while it should be if the effect of this factor is not compensated by something else.

5.11.4 Kivelson-Ridley (2010) Model and SuperDARN CPCP

In Figure 5.16d, predictions of the recent Kivelson-Ridley model for Σ_P = 10 S (Eq. 2.16) are compared to the SuperDARN CPCPs. Better agreement is noticeable in terms of the overall linear trend, i.e. a smaller slope. For this model, predictions are different whether one considers quasi-viscous contributions to the CPCP or not.

Presented in Figure 5.17 is the prediction for the winter dataset according to Equation 2.16, but without Boyle's v_x^2 quasi-viscous term. One can notice that for small IEFs, the slope of the line is getting even closer to the line of perfect agreement, which would have a slope of 1. The lack of agreement between SuperDARN CPCP measurements and the quasi-viscous-related term is expected as previously in this Chapter it was shown that the CPCP and solar wind pressure, dominated by the ram pressure term ρv^2, show little correlation. This is in agreement with other studies, such as *Papitashvili et al.* (1999).

Overall, the Kivelson-Ridley model compared best with SuperDARN data. The authors explained that the model is very close in form to the Hill-Siscoe model, both taking an unsaturated potential or electric field, such as the reconnection electric field, and adding a saturation term, but they differ in the physics used to explain the saturation effect. It should be noted, however, that the saturation terms in each model can be rewritten to look almost identical. Dividing each term in Equation 2.13 by $p_{sw}^{1/2}$ reveals that the numerator is Φ_m (Eq. 2.9), while the denominator contains a term with $E_r \Sigma_P / p_{sw}^{1/2}$. While this does not look familiar at first, $E_r / p_{sw}^{1/2}$, without the clock angle dependency, can be rewritten as $B_T / n_{sw}^{1/2}$, which is the Alfvén velocity, neglecting constants.

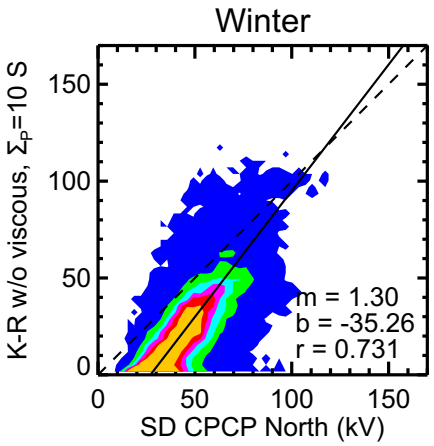

Figure 5.17: Scatterplot of expected CPCP from Eq. 2.16 without the v_x^2 term and SuperDARN CPCP for the winter dataset.

It is possible then that the greatest difference between the models is the coefficients used. The correlation coefficients calculated in Figures 5.16b and 5.17 are nearly identical, 0.730 and 0.731. The density of points looks similar in both, except that the H-S model is stretched vertically, implying that the main difference is in the coefficients. As mentioned above, the coefficient in the Φ_m term in the Hill-Siscoe model appears to be too large. Perhaps a modification to this term or its derivation would result in better agreement.

Our tests showed that the SuperDARN data are not far from predictions of all four theories for small CPCPs. The best agreement is with the Kivelson-Ridley model. However, the agreement is very poor for large CPCPs with SuperDARN giving much smaller values than those expected from the literature. It is noted that the SuperDARN data do not show very strong values of the CPCP.

5.12 Summary of the Findings

In this Chapter, possible connections between the SuperDARN CPCPs and various parameters of the near-Earth space were investigated. SuperDARN CPCP data were also compared with predictions of some recent physics-based and simulation-based models of CPCP formation. The analysis performed led to several conclusions, both regarding SuperDARN CPCP itself and the potential factors in the solar wind affecting it. These conclusions are listed here without ranking their importance.

1. First is a comment on the database which was used in this study. One full year of SuperDARN radar operation was selected. It was shown that the SuperDARN radars, in the configuration of 2000-2001, collected data for all typical values of the solar wind and IMF. However, if the threshold for the number of map points used to derive the CPCP is set at a value of $\sim$300, there are very few measurements with IEF > 3-4 mV/m, the values starting from which the CPCP begin to saturate, as concluded from previous SuperDARN publications and observations made with other instruments/methods. The southern hemisphere coverage is worse due to there being fewer radars present. With selected data coverage, the SuperDARN radars are only suitable for studies of the factors affecting the increasing part of the CPCP dependence upon IEF, and not the saturation part. Additionally, the radars seldom report CPCPs above $\sim$100 kV, no matter what conditions are imposed (*Koustov et al.*, 2009a). This is well below reports where other instruments were used. The apparent saturation seen in SuperDARN CPCP plots versus various parameters are at $\sim$80 kV on average.

2. A number of SuperDARN results reported here are very similar to the ones reported in other SuperDARN studies where the data selection was more elaborate and more justifiable (*Shepherd et al.*, 2003; *Koustov et al.*, 2009a; *Fiori et al.*, 2009). This implies that obtained CPCP are not very sensitive to the specific configuration/distribution of the vectors on a map; one just needs a significant amount of vectors. However, if the threshold is not high enough, the "quantization" effect of the CPCP is clearly seen and the data are strongly affected by the assumed startup convection model. The CPCP values for the models are predetermined at relatively low levels (< 80 kV). The data showed that having more than 300 vectors is a highly desirable goal for every convection map.

3. SuperDARN data for the Northern hemisphere give statistically similar CPCP values for the northern and southern hemispheres. Although a lower threshold was considered for the number of required points for the southern hemisphere, 200 instead of 300, these results hold if N_{map} = 300 is chosen for both hemispheres, although very

few points would be available from the southern hemisphere.

4. For relatively narrow bins of the SW parameters or IMF, the SuperDARN CPCP showed significant variability, ranging at least +/- 20 kV. This variability makes it difficult to reliably establish a relationship between SuperDARN CPCP and various parameters of the near-Earth space.

5. It was shown that the SuperDARN CPCP increases almost linearly with an increase of the negative IMF B_z component, consistent with previous studies. The range of the data is -10 +10 nT. The rate of increase is in agreement with the one inferred from AMIE modelling/magnetometer data, but slower than reported in DMSP measurements. Winter data showed a faster increase, while summer data showed a slower increase. For B_z < -8 nT, a tendency for CPCP saturation is seen but the amount of data tapers off very quickly in this regime. For positive B_z > 8 nT, the CPCP stays at $\sim$20-30 kV, which is consistent with other reported potentials for $B_z > 0$.

6. For negative IMF B_z, the SuperDARN CPCP also increases with the magnitude of the IMF B_y, although weakly. The rate of increase is $\sim$5 times slower than the one for the dependence on the IMF B_z. The B_y dependence is stronger for $B_y > 0$ during winter.

7. Since the SuperDARN CPCP depends strongly upon the IMF B_z and B_y, it strongly changes with the IMF clock angle. The data are best described by the function $\sin^2(\theta_c/2)$.

8. The SuperDARN CPCP showed very little dependence on the velocity of the solar wind. The spread of the CPCP in the bins can be as great as +/- 40 kV.

9. The SuperDARN CPCP varies weakly with the solar wind pressure. There is virtually no trend for typical IEF values of 1-3 mV/m. At smaller and larger IEFs, a subtle tendency for increase is present. The former (latter) is consistent (inconsistent) with the Hill-Siscoe model predictions. Unfortunately, the available data cover mostly small values of P_{sw} so that the effects of strong P_{sw} were not possible to investigate.

10. The SuperDARN CPCP increases almost linearly with the IEF in the range -3 to +3 mV/m. The rate of increase is larger in winter and smaller in summer, consistent with previous SuperDARN studies. The rate of increase depends strongly on the size of the magnetopause; the dependence of the CPCP on the IEF is stronger for larger magnetosphere radii and weaker for smaller radii. Perhaps the decrease in the CPCP variation with IEF at large values of the IEF is evidence for the CPCP saturation effect at IEF > 3-5 mV/m. Another indication of the saturation effect is stabilization in the fall of the rate increase at large IEFs. Unfortunately, the amount of data is insignificant at large IEF values.

11. The Alfvén-Mach number correlates, although weakly, with the SuperDARN CPCP. Data show a general decrease of the CPCP with increasing M_A. The trends of M_A appear to be dominated by B_T.

12. The Alfvén velocity also correlates somewhat with SuperDARN CPCP. Data show that the CPCP increases with v_A for small IEFs but at large IEFs, there is almost no CPCP dependence on v_A. This could be an indication of the saturation effect depicted by *Kivelson and Ridley* (2008), who show a decrease in CPCP dependence on E_r with increasing v_A. We should note that the number of points for large IEFs is not significant to confidently conclude, but the effect of the decrease in the slope between CPCP and v_A is clearly there.

13. The difference in the CPCP between the northern and southern hemispheres is influenced by the IMF B_y and B_x values for all seasons. For $B_y < 0$ and $B_x > 0$, there was a minor trend for southern hemisphere CPCPs to be larger, while for $B_y > 0$ and $B_x < 0$ the trend favoured the northern hemisphere. A potential physical explanation is that B_y and B_x alter the location where reconnection occurs at the frontside magnetopause, creating an imbalance in the energy transferred to each hemisphere. Alternatively, we hypothesize that the effect is that of the startup convection model that assigns more voltage in the northern hemisphere for $B_y > 0$, although this effect is supposedly minimised by the data selection process.

14. There is little difference between CPCPs observed in the "sunlit" and "dark" ionosphere if data in one hemisphere are considered, although rates of increase with various parameters, such as IEF and B_z, were stronger in the dark ionosphere, i.e. winter.

CHAPTER 6

CONCLUSIONS AND SUGGESTIONS FOR FUTURE RESEARCH

The research contained in this Thesis is twofold. First, a validation of SuperDARN data was performed using the CADI at Resolute Bay. This involved both 1-D and 2-D velocity comparisons between the PolarDARN radars and the RB CADI, as well as studying the relationship between CADI velocities, representing the average polar cap convection, and SuperDARN CPCP, in an attempt to identify the reasons for SuperDARN CPCP underestimation in comparison with other techniques. Second, the relationship between the CPCP, inferred from SuperDARN l-o-s velocities, and solar wind/IMF parameters was investigated. This involved comparing SuperDARN CPCP to various individual solar wind/IMF parameters and to numerous coupling functions that have been proposed in the past, as well as comparing simultaneous SuperDARN data between hemispheres. Also, four chosen theories of CPCP formation were tested against SuperDARN CPCP.

6.1 Conclusions

6.1.1 SuperDARN Velocity/CPCP Validation

First, SuperDARN velocities were plotted against Resolute Bay CADI to investigate the effect of velocity underestimation on the supposed SuperDARN CPCP underestimation. Line-of-sight plasma velocity measurements from the PolarDARN radars at Rankin Inlet and Inuvik were shown to be comparable to plasma drift measurements from the Resolute Bay CADI. Both the CADI projection (1-D) analysis and the merged PolarDARN (2-

D) analysis revealed that there is good agreement between the instruments. There was, however, a trend in both analyses for the PolarDARN velocities to be slightly larger than the CADI velocities. This was unexpected, as SuperDARN in the past has been shown to underestimate the $\mathbf{E} \times \mathbf{B}$ drift when compared to other instruments such as DMSP ion drift meters and incoherent scatter radars.

The second part of the validation involved testing SuperDARN CPCP against another ionospheric parameter, i.e., CADI $\mathbf{E} \times \mathbf{B}$ drift measurements, which act as a proxy for the average ionospheric polar cap electric field. A linear trend was observed for CADI velocities up to 800 m/s, although a high variance in the data made it difficult to reach a conclusion.

Overall, with these studies, no issues could be found with the SuperDARN CPCP data. This still does not explain why SuperDARN CPCP is much smaller than CPCP derived from other instruments. It is believed that the major factors involved in this could be the statistical model that is used to fill in the gaps in radar coverage and the Heppner-Maynard boundary. While the data were selected for only maps derived using a minimum number of points, one wonders how much influence the model still has in determining the CPCP. The Heppner-Maynard boundary has been shown to cause disagreement between fitted vectors and l-o-s velocities near the boundary and likely causes CPCP underestimation during storm conditions when the polar cap expands equatorward. These issues may be dealt with by better radar coverage, which is currently in progress with the recent addition of the mid-latitude radars and the future addition of auroral radars in Russia.

6.1.2 SuperDARN CPCP Dependence on the Solar Wind/IMF

SuperDARN CPCP was tested against various solar wind and IMF parameters to determine which parameters were the most important in generating the CPCP. The parameters chosen are ones used in numerous solar wind coupling functions, theories and models describing solar wind-magnetospheric-ionospheric coupling. A number of these functions and models were chosen for comparison with SuperDARN CPCP.

Of all the parameters tested against the SuperDARN CPCP, the ones that showed the best correlation with or influence on the CPCP were IMF B_T, IMF B_z, θ_c, E_{sw}, R_{ms}, and v_A.

IMF B_z had the highest linear correlation, although saturation is present for $|B_z| > 8$; also highly correlated were B_T, E_{sw} (also showing saturation) and θ_c. Solar wind pressure did not appear to show any direct correlation, but the magnetosphere radius R_{ms}, proportional to $p_{sw}^{-1/6}$, appeared to play an important role in determining the slope between CPCP and E_{sw}. Likewise, the slope between CPCP and E_{sw} appeared to be somewhat affected by v_A. Parameters that showed low correlation to the CPCP were v_{sw} and n_{sw}, although these are believed to be involved in combination with other parameters, and are also the components of the solar wind ram pressure.

The linear correlations between SuperDARN CPCP and various solar wind coupling functions were tested. The best correlation coefficients were obtained with the function by *Lyatsky et al.* (2007) and the square root of the function by *Wygant et al.* (1983). Both functions contained the factor $\sqrt{B_T}$. One reason why fractional powers of B_T performed better is that CPCP saturation with B_T is better matched with a square root function than a linear relationship. Coupling functions with $\sin^2(\theta_c/2)$ appeared to have higher correlation coefficients than ones with higher exponents. Coupling functions including an n_{sw} term had lower correlation coefficients.

Simultaneous SuperDARN data between the northern and southern hemispheres were compared in order to test for possible differences due to ionospheric conductance, theorised to affect the CPCP. Little difference was detected when comparing the sun-lit and dark ionospheres, represented by summer and winter, respectively. However, a trend was found when the CPCP difference was plotted against the IMF B_x and B_y terms. The northern CPCP data tended to be larger than the southern CPCP when $B_y > 0$ and $B_x < 0$, and smaller for $B_y < 0$ and $B_x > 0$. Since the statistical model used for the northern hemisphere gives larger CPCPs for $B_y > 0$, one wonders if this effect is physical or if the statistical model has more effect than previously thought.

SuperDARN CPCP was compared to four theories and models predicting the CPCP using solar wind/IMF parameters. The theory providing the closest CPCP to SuperDARN was the Kivelson-Ridley theory, although the predicted CPCP was on average about 1.5 times larger than the SuperDARN CPCP. This number lowered somewhat when the quasi-viscous term in the Kivelson-Ridley formula was not considered. The Hill-Siscoe model

had a very high correlation coefficient, although was on average nearly twice as large as the SuperDARN CPCP.

6.2 Future Research

Initially, one of the objectives of this Thesis was to investigate the CPCP saturation effect with SuperDARN data, but this proved to be difficult, both due to the questions raised about the quality of CPCP data under extreme conditions, and the lack of such data. The data used in this study are from the last solar maximum, from 2000-2002, when fewer radars were present than are currently in operation (the PolarDARN and the mid-latitude radars were added). The main reason why more recent data were not used was simply a lack of extreme conditions due to the extended minimum of Solar Cycle 23. Hopefully, with another solar maximum and the newer radars, more data will be available for extreme solar wind conditions and the work undertaken here can be expanded with improved datasets. Initial work with the mid-latitude radars has already shown somewhat larger CPCP values those calculated with only the auroral radars.

Another issue, that was not addressed in this Thesis, is SuperDARN velocity underestimation compared to other instruments. In this study, the actual quality of the PolarDARN velocity measurements was not investigated. All measurements relied on ACF quality flags built into the standard SuperDARN processing software. It is important to investigate the quality of the PolarDARN data while comparing with CADI $\mathbf{E} \times \mathbf{B}$ measurements. Of special interest should be the larger velocities that disagreed with CADI measurements, which cannot be explained by the ground scatter contamination of radar echoes.

Such an investigation is also important for CADI as an instrument for convection measurements. CADI $\mathbf{E} \times \mathbf{B}$ measurements have not been scrutinized in the past like SuperDARN data, but CADIs become increasingly important as their numbers increase and they operate at the very high latitudes where the PolarDARN radars detect very few echoes. CADIs theoretically are not affected by the refractive index. The question is: why is the measured velocity even smaller that the PolarDARN velocity, which are very likely affected by the index of refraction? Of interest are cases where the polarity of the Polar-

DARN velocity is opposite to the projection of the CADI vector onto the radar beam. The currently accepted notion is that such cases correspond to instruments monitoring well-separated ionospheric regions. Since CADI data have information of echo location, this opinion can be tested with the data available. One can think that perhaps such cases are due to a low number of reflectors involved in the velocity determination (for the Resolute Bay CADI it seldom surpasses 50). A special experiment can be run with CADI operating in the so called "dynasonde" mode. In this mode, the velocity measurements are done at many transmitted frequencies and not limited to the choice of either 3 or 4 MHz (CADI provides data on 5 and 6 MHz, but these are very limited) so that velocity determination would be more reliable.

The next aspect of the current work is the quality of the CPCP determination from l-o-s data. It is clear that the CPCP can be strongly affected by the startup convection model. The recent work by *Cousins and Shepherd* (2010) is a step in the right direction. They developed a new statistical model that better reflects ionospheric responses to changes in the IMF. Of note is the statistical model in the southern hemisphere, which is quite different than that for the northern hemisphere. This poses questions about the role of the startup convection model in SuperDARN mapping. *Fiori et al.* (2010) developed a technique that works without any convection model and does not use the Heppner-Maynard boundary either. It is not clear yet if their method is better than the current work with the startup convection model. It would be interesting to perform a comparison of the methods with a significant database.

Ideally, there would be no need for a statistical model if enough data could be obtained. Installing radars to cover the entire polar cap and auroral region would be a step in the right direction, although the radars are still dependent on ionospheric conditions for receiving echoes.

BIBLIOGRAPHY

Baker, J. B. H., R. A. Greenwald, J. M. Ruohoniemi, K. Oksavik, J. W. Gjerloev, L. J. Paxton, and M. R. Hairston, Observations of ionospheric convection from the Wallops superDARN radar at middle latitudes, *J. Geophys. Res.*, *112*, A01303, doi: 10.1029/2006JA011982, 2007.

Borovsky, J. E., B. Lavraud, and M. M. Kuznetsova, Polar cap potential saturation, dayside reconnection, and changes to the magnetosphere, *J. Geophys. Res.*, *114*, A03224, doi: 10.1029/2009JA014058, 2009.

Boyle, C. B., P. H. Reiff, and M. R. Hairston, Empirical polar cap potentials, *J. Geophys. Res.*, *102*, 111, doi:10.1029/96JA01742, 1997.

Bristow, W. A., R. A. Greenwald, S. G. Shepherd, and J. M. Hughes, On the observed variability of the cross-polar cap potential, *J. Geophys. Res.*, *109*, A02203, doi: 10.1029/2003JA010206, 2004.

Coco, I., E. Amata, M. F. Marcucci, M. D. Laurentis, J. P. Villain, C. Hanuise, and M. Candidi, Effects on SuperDARN HF radar echoes of sudden impulses of solar wind dynamic pressure, *Ann. Geophys.*, *23*, 1771–1783, 2005.

Cousins, E. D. P., and S. G. Shepherd, A dynamical model of high-latitude convection derived from SuperDARN plasma drift measurements, *J. Geophys. Res.*, *115*, A12329, doi:10.1029/2010JA016017, 2010.

de la Beaujardiere, O., D. Alcayde, J. Fontanari, and C. Leger, Seasonal dependence of high-latitude electric fields, *J. Geophys. Res.*, *96*(A4), 5723–5735, 1991.

Doyle, M. A., and W. J. Burke, S3-2 measurements of the polar cap potential, *J. Geophys. Res.*, *88*(A11), 9125–9133, 1983.

Drayton, R. A., A. V. Koustov, M. R. Hairston, and J.-P. Villain, Comparison of DMSP cross-track ion drifts and SuperDARN line-of-sight velocities, *Ann. Geophys.*, *23*, 2479–2486, 2005.

Dungey, J. W., Interplanetary magnetic field and the auroral zones, *Phys. Res. Lett.*, *6*, 47–49, 1961.

Fiori, R. A. D., A. V. Koustov, D. Boteler, and R. A. Makarevich, PCN magnetic index and average convection velocity in the polar cap inferred from SuperDARN radar measurements, *J. Geophys. Res.*, *114*, A07225, doi:10.1029/2008JA013964, 2009.

Fiori, R. A. D., D. H. Boteler, A. V. Koustov, G. V. Haines, and J. M. Ruohoniemi, Spherical cap harmonic analysis of Super Dual Auroral Radar Network (SuperDARN) observations for generating maps of ionospheric convection, *J. Geophys. Res.*, *115*, A07307, doi:10.1029/2009JA015055, 2010.

Förster, M., G. Paschmann, S. E. Haaland, J. M. Quinn, R. B. Torbert, H. Vaith, and C. A. Kletzing, High-latitude plasma convection from Cluster EDI: variances and solar wind correlations, *Ann. Geophys.*, *25*, 1691–1707, 2007.

Ghezelbash, M., H. Liu, A. V. Koustov, and D. Andre, PolarDARN radar echo occurrence in the polar cap, in *Abstracts of DASP (CAP) Annual Meeting*, Saskatoon, 2011.

Gilles, R. G., G. C. Hussey, G. J. Sofko, K. A. McWilliams, R. A. D. Fiori, P. Ponomarenko, and J.-P. St.-Maurice, Improvement of SuperDARN velocity measurements by estimating the index of refraction in the scattering region using interferometry, *J. Geophys. Res.*, *114*, A07305, doi:10.1029/2008JA013967, 2009.

Greenwald, R. A., et al., DARN/SuperDARN: A global view of the dynamics of high-latitude convection, *Space Sci. Rev.*, *71*, 763–796, 1995.

Grocott, A., S. V. Badman, S. W. H. Cowley, S. E. Milan, J. D. Nichols, and T. K. Yeoman, Magnetosonic Mach number dependence of the efficiency of reconnection between planetary and interplanetary magnetic fields, *J. Geophys. Res.*, *114*, A07219, doi:10.1029/2009JA014330, 2009.

Haaland, S., G. Paschmann, and B. U. O. Sonnerup, Comment on "a new interpretation of Weimer et al.'s solar wind propagation delay technique" by Bargatze et al., *J. Geophys. Res.*, *111*, A06102, doi:10.1029/2005JA011376, 2006.

Haaland, S., G. Paschmann, M. Förster, J. M. Quinn, R. B. Torbert, C. E. McIlwain, H. Vaith, P. A. Puhl-Quinn, and C. A. Kletzing, High-latitude plasma convection from Cluster EDI measurements: method and IMF-dependence, *Ann. Geophys.*, *25*, 239–253, 2007.

Hairston, M. R., T. W. Hill, and R. A. Heelis, Observed saturation of the ionospheric polar cap potential during the 31 March 2001 storm, *Geophys. Res. Lett.*, *30*, 1325, doi:10.1029/2002GL015894, 2003.

Hairston, M. R., K. A. Drake, and R. Skoug, Saturation of the ionospheric polar cap potential during the October-November 2003 superstorms, *J. Geophys. Res.*, *110*, A09S26, doi:10.1029/2004JA010864, 2005.

Hargreaves, J. K., *The Solar-Terrestrial Envionment*, Cambridge University Press, Cambridge, UK, 1992.

Hill, T. W., A. J. Dessler, and R. A. Wolf, Mercury and Mars: The role of ionospheric conductivity in the acceleration of magnetospheric particles, *Geophys. Res. Lett.*, *3*(8), 429–432, 1976.

Jayachandran, P. T., et al., The Canadian high arctic ionospheric network (CHAIN), *Radio Sci.*, *44*, RS0A03, doi:10.1029/2008RS004046, 2009.

Kan, J. R., and L. C. Lee, Energy coupling function and solar wind magnetosphere dynamo, *Geophys. Res. Lett.*, *6*(7), 577–580, 1979.

Kan, J. R., H. Li, C. Wang, B. B. Tang, and Y. Q. Hu, Saturation of polar cap potential: Nonlinearity in quasi-steady solar wind-magnetosphere-ionosphere coupling, *J. Geophys. Res.*, *115*, A08226, doi:10.1029/2009JA014389, 2010.

Khachikjan, G. Y., A. V. Koustov, and G. J. Sofko, Dependence of SuperDARN cross polar cap potential upon the solar wind electric field and magnetopause subsolar distance, *J. Geophys. Res.*, *113*, A09214, doi:10.1029/2008JA013107, 2008.

Kihn, E. A., R. Redmon, A. J. Ridley, and M. R. Hairston, A statistical comparison of the AMIE derived and DMSP-SSIES observed high-latitude ionospheric electric field, *J. Geophys. Res.*, *111*, A08303, doi:10.1029/2005JA011310, 2006.

Kivelson, M. G., and A. J. Ridley, Saturation of the polar cap potential: Inference from Alfvén wing arguments, *J. Geophys. Res.*, *113*, A05214, doi:10.1029/2007JA012302, 2008.

Kivelson, M. G., and C. T. Russell, *Introduction to Space Physics*, Cambridge University Press, Cambridge, UK, 1995.

Koustov, A. V., G. J. Sofko, D. Andre, D. W. Danskin, and L. V. Benkevitch, Seasonal variation of HF radar F region echo occurrence in the midnight sector, *J. Geophys. Res.*, *109*, A06305, doi:10.1029/2003JA010337, 2004.

Koustov, A. V., J. W. MacDougall, and G. E. Kadochnikov, A comparison of CADI-inferred F region plasma convection and DMSP ion drift above Resolute Bay, *Radio Sci.*, *42*, RS6012, doi:10.1029/2007RS003706, 2007.

Koustov, A. V., G. Y. Khachikjan, R. A. Makarevich, and C. Bryant, On the SuperDARN cross polar cap potential saturation effect, *Ann. Geophys.*, *27*, 3755–3764, 2009a.

Koustov, A. V., J.-P. St.-Maurice, G. J. Sofko, D. Andre, J. W. MacDougall, M. R. Hairston, R. A. Fiori, and E. E. Kadochnikov, Three-way validation of the Rankin Inlet PolarDARN radar velocity measurements, *Radio Sci.*, *44*, RS4003, doi:10.1029/2008RS004045, 2009b.

Liemohn, M. W., and A. J. Ridley, Comment on "nonlinear response of the polar ionosphere to large values of the interplanetary electric field" by C. T. Russell et al., *J. Geophys. Res.*, *107*(A12), 1460, doi:10.1029/2002JA009440, 2002.

Liu, H., Study of the high-latitude ionosphere with the Rankin Inlet PolarDARN radar, Master's thesis, University of Saskatchewan, 2010.

Liu, W. W., Polar cap potential saturation: An energy conservation perspective, *J. Geophys. Res.*, *112*, A07210, doi:10.1029/2007JA012392, 2007.

Lyatsky, W., S. Lyatskaya, and A. Tan, A coupling function for solar wind effect on geomagnetic activity, *Geophys. Res. Lett.*, *34*, L02107, doi:10.1029/2006GL027666, 2007.

Lyatsky, W., G. V. Khazanov, and J. A. Slavin, Saturation of the electric field transmitted to the magnetosphere, *J. Geophys. Res.*, *115*, A08221, doi:10.1029/2009JA015091, 2010.

Lyons, L. R., and D. J. Williams, *Quantitative Aspects of Magnetospheric Physics*, D. Reidel Publishing Company, Dordrecht, Holland, 1984.

MacDougall, J. W., and P. T. Jayachandran, Polar cap convection relationships with solar wind, *Radio Sci.*, *36*(6), 1869–1880, 2001.

MacDougall, J. W., and P. T. Jayachandran, Polar cap voltage saturation, *J. Geophys. Res.*, *111*, A12306, doi:10.1029/2006JA011741, 2006.

Merkin, V. G., A. S. Sharma, K. Papadopoulos, G. Milikh, J. Lyon, and C. Goodrich, Global MHD simulations of the strongly driven magnetosphere: Modeling of the transpolar potential saturation, *J. Geophys. Res.*, *110*, A09203, doi:10.1029/2004JA010993, 2005a.

Merkin, V. G., A. S. Sharma, K. Papadopoulos, G. Milikh, J. Lyon, and C. Goodrich, Relationship between the ionospheric conductance, field aligned current, and magnetopause geometry: Global MHD simulations, *Planet. Space Sci.*, *53*, 873–879, doi:10.1016/j.pss.2005.04.001, 2005b.

Milan, S. E., Dayside and nightside contributions to the cross polar cap potential: placing an upper limit on a viscous-like interaction, *Ann. Geophys.*, *22*, 3771–3777, 2004.

Mitchell, E. J., R. E. Lopez, R. J. Bruntz, M. Wiltberger, J. G. Lyon, R. C. Allen, S. J. Cockrell, and P. L. Whittlesey, Saturation of transpolar potential for large

Y component interplanetary magnetic field, *J. Geophys. Res.*, *115*, A06201, doi: 10.1029/2009JA015119, 2010.

Mori, D., S. Toderian, A. V. Koustov, and P. T. Jayachandran, PolarDARN velocities: Are they consistent with SuperDARN and CADI measurements?, in *Abstracts of DASP (CAP) Annual Meeting*, p. 9, Saskatoon, 2011.

Newell, P. T., T. Sotirelis, K. Liou, C.-I. Meng, and F. J. Rich, A nearly universal solar wind-magnetosphere coupling function inferred from 10 magnetospheric state variables, *J. Geophys. Res.*, *112*, A01206, doi:10.1029/2006JA012015, 2007.

Ober, D. M., N. C. Maynard, and W. J. Burke, Testing Hill model of transpolar potential saturation with observations, *J. Geophys. Res.*, *108*, 1467, doi:10.1029/2003JA010154, 2003.

Papitashvili, V., and F. J. Rich, High-latitude ionospheric convection models derived from Defense Meteorological Satellite Program ion drift observations and parameterized by the interplanetary magnetic field strength and direction, *J. Geophys. Res.*, *107*, 1198, doi:10.1029/2001JA000264, 2002.

Papitashvili, V., F. Rich, M. Heinemann, and M. Hairston, Parameterization of the Defense Meteorological Satellite Program ionospheric electrostatic potentials by the interplanetary magnetic field strength and direction, *J. Geophys. Res.*, *104*, doi: 10.1029/1998JA900053, 1999.

Perrault, W. K., and S.-I. Akasofu, A study of geomagnetic storms, *Geophys. J. R. Astron. Soc.*, *54*, 547, 1978.

Pettigrew, E. D., S. G. Shepherd, and J. M. Ruohoniemi, Climatological patterns of high-latitude convection in the northern and southern hemispheres: Dipole tilt dependencies and interhemispheric comparisons, *J. Geophys. Res.*, *115*, A07305, doi: 10.1029/2009JA014956, 2010.

Ponomarenko, P. V., C. L. Waters, and F. W. Menk, Effects of mixed scatter on Super-DARN convection maps, *Ann. Geophys.*, *26*, 1517–1523, doi:10.5194/angeo-26-1517-2008, 2008.

Pudovkin, M. I., S. A. Zaitseva, T. A. Bazhenova, and V. G. Andrezen, Electric fields and currents in the earth's polar caps, *Planet. Space Sci.*, *33*(4), 407–414, 1985.

Raeder, J., and G. Lu, Polar cap saturation during large geomagnetic storms, *Adv. Space Res.*, *36*, 1804–1808, 2005.

Reiff, P. H., and J. G. Luhmann, Solar wind control of the polar-cap voltage, in *Solar wind-magnetosphere coupling*, edited by Y. Kamide and J. Slavin, pp. 453–476, Terra Sci., Tokyo, 1986.

Reiff, P. H., R. R. Spiro, , and T. Hill, Dependence of polar cap potential on interplanetary parameters, *J. Geophys. Res.*, *86*, 7639–7648, 1981.

Richmond, A. D., Assimilative mapping of ionospheric electrodynamics, *Adv. Space Res.*, *12*(6), 59–68, 1992.

Richmond, A. D., and Y. Kamide, Mapping electrodynamic features of the high-latitude ionosphere from localized observations: technique, *J. Geophys. Res.*, *93*(A6), 5741–5759, 1988.

Ridley, A., Alfvén wings at the Earth's magnetosphere under strong interplanetary magnetic field, *Ann. Geophys.*, *23*, 533–542, 2007.

Ridley, A. J., A new formulation for the ionospheric cross polar cap potential including saturation effects, *Ann. Geophys.*, *23*, 3533–3548, 2005.

Ridley, A. J., and E. A. Kihn, Polar cap index comparisons with AMIE cross polar cap potential, electric field, and polar cap area, *Geophys. Res. Lett.*, *31*, L07801, doi: 10.1029/2003GL019113, 2004.

Ridley, A. J., G. Lu, C. R. Clauer, and V. O. Papitashvili, A statistical study of the ionospheric convection response to changing interplanetary magnetic field conditions using

the assimilative mapping of ionospheric electrodynamics technique, *J. Geophys. Res.*, *103*, 4023–4039, 1998.

Ruohoniemi, J. M., and K. B. Baker, Large-scale imaging of high-latitude convection with Super Dual Auroral Radar Network HF radar observations, *J. Geophys. Res.*, *103*(A9), 20,797–20,811, 1998.

Ruohoniemi, J. M., and R. A. Greenwald, Dependencies of high-latitude plasma convection: Consideration of interplanetary magnetic field, seasonal, and universal time factors in statistical patterns, *J. Geophys. Res.*, *110*, doi:10.1029/2004JA010815, 2005.

Russell, C. T., J. G. Luhmann, and G. Lu, Nonlinear response of the polar ionosphere to large values of the interplanetary electric field, *J. Geophys. Res.*, *106*, 18,495–18,504, doi:10.1029/2001JA900053, 2001.

Scali, J. L., B. W. Reinisch, C. J. Heinselman, and T. W. Bullett, Coordinated digisonde and incoherent scatter radar F region drift measurements at Sondre Stromfjord, *Radio Sci.*, *30*(5), 1481–1498, doi:10.1029/95RS01730, 1995.

Sedgemore, K. J. F., P. J. S. Williams, G. O. L. Jones, and J. W. Wright, A comparison of EISCAT and Dynasonde measurements of the auroral ionosphere, *Ann. Geophys.*, *14*, 1403–1412, 1996.

Sedgemore, K. J. F., J. W. Wright, P. J. S. Williams, G. O. L. Jones, and M. T. Rietveld, Plasma drift estimates from the Dynasonde: comparison with EISCAT measurements, *Ann. Geophys.*, *16*, 1138–1143, 1998.

Shepherd, S. G., Polar cap potential saturation: Observations, theory, and modeling, *J. Atmos. Sol.-Terr. Phys.*, *69*, 234–248, doi:10.1016/j.jastp.2006.07.022, 2007.

Shepherd, S. G., and J. M. Ruohoniemi, Electrostatic potential patterns in the high-latitude ionosphere constrained by superdarn measurements, *J. Geophys. Res.*, *105*(A10), 23,005–23,014, 2000.

Shepherd, S. G., R. A. Greenwald, and J. M. Ruohoniemi, Cross polar cap potentials measured with Super Dual Auroral Radar Network during quasi-steady solar wind and interplanetary magnetic field conditions, *J. Geophys. Res.*, *107*(A7), 1–9, doi: 10.1029/2001JA000152, 2002.

Shepherd, S. G., J. M. Ruohoniemi, and R. A. Greenwald, Testing the Hill model of transpolar potential with Super Dual Auroral Radar Network observations, *Geophys. Res. Lett.*, *30*(1), 1002, doi:10.1029/2002GL015426, 2003.

Siscoe, G. L., and K. D. Siebert, Comment on "Polar cap voltage saturation" by J. W. MacDougall and P. T. Jayachandran, *J. Geophys. Res.*, *112*, A06227, doi: 10.1029/2006JA012242, 2007.

Siscoe, G. L., N. U. Crooker, and K. D. Siebert, Transpolar potential saturation: Roles of region 1 current system and solar wind ram pressure, *J. Geophys. Res.*, *107*(A10), 1321, doi:10.1029/2001JA009176, 2002a.

Siscoe, G. L., G. M. Erickson, B. U. Ö. Sonnerup, N. C. Maynard, J. A. Schoendorf, K. D. Siebert, D. R. Weimer, W. W. White, and G. R. Wilson, Hill model of transpolar potential saturation: Comparisons with MHD simulations, *J. Geophys. Res.*, *107*(A6), doi:10.1029/2001JA000109, 2002b.

Siscoe, G. L., J. Raeder, and A. J. Ridley, Transpolar potential saturation models compared, *J. Geophys. Res.*, *109*, A09203, doi:10.1029/2003JA010318, 2004.

Spreiter, J. R., A. L. Summers, and A. Y. Alksne, Hydromagnetic flow around the magnetosphere, *Planet. Space Sci.*, *14*, 223–253, 1966.

Temerin, M., and X. Li, Dst model for 1995–2002, *J. Geophys. Res.*, *111*, A04221, doi: 10.1029/2005JA011257, 2006.

Troshichev, O., H. Hayakawa, A. Matsuoka, T. Mukai, and K. Tsuruda, Cross polar cap diameter and voltage as a function of PC index and interplanetary quantities, *J. Geophys. Res.*, *101*(A6), 13,429–13,435, 1996.

Troshichev, O., A. Janzhura, and P. Stauning, Unified PCN and PCS indices: Method of calculation, physical sense, and dependence on the IMF azimuthal and northward components, *J. Geophys. Res.*, *111*, A05208, doi:10.1029/2005JA011402, 2006.

Troshichev, O. A., R. Y. Lukianova, V. O. Papitashvili, F. J. Rich, and O. Rasmussen, Polar cap index (PC) as a proxy for ionospheric electric field in the near-pole region, *Geophys. Res. Lett.*, *27*(23), 3809–3812, 2000.

Villain, J.-P., R. A. Greenwald, K. B. Baker, and J. M. Ruohoniemi, HF radar observations of E region plasma irregularities produced by oblique electron streaming, *J. Geophys. Res.*, *92*, 12,327–12,342, 1987.

Weimer, D. R., Models of high-latitude electric potentials derived with a least error fit of spherical harmonic coefficients, *J. Geophys. Res.*, *100*(A10), 19,595–19,607, 1995.

Weimer, D. R., D. M. Ober, N. C. Maynard, M. R. Collier, D. J. McComas, N. F. Ness, C. W. Smith, and J. Watermann, Predicting interplanetary magnetic field (IMF) propagation delay times using the minimum variance technique, *J. Geophys. Res.*, *108*(A1), 1026, doi:10.1029/2002JA009405, 2003.

Wygant, J. R., R. B. Torbert, and F. S. Mozer, Comparison of S3-3 polar cap potential drops with the interplanetary magnetic field and models of magnetopause reconnection, *J. Geophys. Res.*, *88*, 5727, 1983.

Xu, L., A. V. Koustov, J. Thayer, and M. McCready, SuperDARN convection and Sondrestrom plasma drift, *Ann. Geophys.*, *19*, 749–759, 2001.

Xu, L., A. V. Koustov, J.-S. Xu, L. Huo, and R. A. Drayton, A 2-D comparison of ionospheric convection derived from SuperDARN and DMSP measurements, *Adv. Space Res.*, *42*, 1459–1266, doi:10.1016/j.asr.2007.06.044, 2008.